ATTENUATION OF LOW FREQUENCY STRUCTURALLY RADIATED NOISE WITH AN ARRAY OF WEAK RADIATING CELLS

Bradley W. Ross

Thesis to be submitted to the Faculty of the
Virginia Polytechnic Institute and State University
in partial fulfillment of the requirements for the degree of

Master of Science
in
Mechanical Engineering

Dr. Ricardo A. Burdisso, Chair
Dr. Harley H. Cudney
Dr. William R. Saunders

February, 1998
Blacksburg, Virginia

Keywords: Structural Acoustics, Passive Sound Reduction, Acoustic Dipole, Weak Radiating Cell

ATTENUATION OF LOW FREQUENCY STRUCTURALLY RADIATED NOISE WITH AN ARRAY OF WEAK RADIATING CELLS

Bradley W. Ross

(ABSTRACT)

The concept of a weak sound radiating cell is proposed to reduce the low frequency radiated noise from structures. The cell consists of two coupled surfaces such that, when placed on a vibrating structure, the responses of the two surfaces are nearly out-of-phase and of equal strength over a wide frequency range. This structure response leads the cell to behave as an acoustic dipole and thus as a poor sound radiating source. The control of low frequency structurally radiated noise is then achieved by covering the structure with an array of these weak radiating cells, i.e. surface treatment. Thus, the surface treatment essentially transforms the response of the structure to that of a distributed array of dipoles yielding a low sound radiating structure. Theoretical models are developed to predict the performance of the cell. Experimental verification is performed for a single cell applied to a piston-like structure to demonstrate the concept on a simple radiating structure. The results demonstrated an overall sound power level reduction of 5.2 dB between 400-1600 Hz with maximum reductions over 30 dB at discrete frequencies. Finally, an array of weak radiating cells is experimentally applied to a more complex structure, a rectangular plate. The results of the plate experiments reveal an overall sound power level reduction of 10.2 dB between 100-1600 Hz with maximum reductions of 25 dB at discrete frequencies. These results demonstrate the potential of the weak radiating cell concept to reduce low frequency structurally radiated noise.

Acknowledgements

I would first like to thank Ricardo Burdisso for strengthening my interest in the field of acoustics and for giving me the opportunity to further explore this interest through graduate studies at Virginia Tech.

Special thanks must be given to Brody Johnson and Jerome Smith for being friends and sources of knowledge when a different point of view was most needed. I would also like to thank Cathy Guigou for her assistance on many levels, including always keeping things in perspective. To Dawn Williams and Nancy Thomas, I am grateful for all the financial and political wrinkles you ironed out along the way. Also, thanks to the rest of the VAL members, especially to Steve Booth for his extensive help in the machine shop.

I am indebted to my father, William Ross, mother, Sharyl Ross, brother, Brian, and sister, Kristin, for their monetary and emotional support throughout my academic career.

Finally, to everyone who supported me in my decision to begin my occupational career prior to fulfilling my degree requirements, we knew I would do it!

Table of Contents

List of Figures

List of Tables

Chapter 1

Introduction

The cancellation of unwanted sound has become a major subject of interest as federal regulations have stiffened, as consumer's desires for quieter products have increased, and as the Department of Defense has entered an era of acoustic stealth to further advance its military force. This has led to extensive research to gain a better understanding of the acoustic behavior of structures such as helicopters, airplanes, power transformers, and so forth. The attenuation of structurally radiated noise, in particular at low frequencies, from these systems and others alike has been intensively pursued.

Helicopter cabin noise has been investigated by Murray and Wilby [1] to define the structureborne and airborne noise source paths that contribute to interior sound pressure levels exceeding 90 dB at frequencies below 500 Hz. In addition to identifying dominating sound transmission paths, the authors address the concern of space limitations and additional weight imposed by potential treatments designed to reduce the excessive helicopter cabin noise levels.

Later, a thorough overview of aircraft interior noise was presented by Wilby [2]. Turboprop aircraft possess a low frequency cabin noise problem that is primarily generated by the blade passing frequency of the propeller and its harmonics at frequencies below 400 Hz and by boundary layer noise at frequencies above 400 Hz. Again, interior sound pressure levels can approach 90 dB at low frequencies.

Another structure that deserves attention to low frequency sound radiation is the power transformer. Though geared toward divulging an active control solution, Brungardt, Vierengel, and Wiessman [3] present a short summary of the power transformer noise problem. Traditional methods used for attenuation of sound radiated to areas surrounding the power substation are discussed. For transformers in North America where the line frequency is 60 Hz, the noise consists of 120 Hz tones and its harmonics. In most cases, the noise problems are dominant below 480 Hz.

Helicopters, airplanes, and power transformers are a small sample of a diverse variety of structures that require attenuation of low frequency noise. In light of this, it is the intent of this thesis to investigate the control of low frequency structurally radiated sound.

1.1 Noise Control Approaches

Noise control approaches are typically classified as passive, active, or a combination of the two control techniques, referred to as hybrid. Though each category presents viable solutions to today's noise control problems, serious limitations are encountered, in particular, in the control of low frequency structurally radiated noise.

Traditional passive methods of noise control include applying treatments to the radiating structure surface such as absorptive and damping materials. However, absorptive materials are not practical means of attenuation at low frequencies because of the thickness requirement to absorb the large acoustic wavelengths. On the other hand, damping materials typically are not effective in attenuating low frequency vibrations. Thick and massive viscous materials are required, which again presents a practicality problem with implementing this traditional control technique to realistic applications. In light of this, researchers have investigated alternate passive control techniques designed to reduce the low frequency sound radiation from structures. Attempts have been made by embedding arrays of acoustic resonators into transmission loss panels mounted to structures [4,5]. In the efforts by Prydz, Wirt, and Kuntz, an array of embedded

Helmholtz resonators was tuned to a specific frequency. Both numerical predictions and experimental results revealed a transmission loss of over 60 dB at discrete frequencies just above the resonator's natural frequency. Lee and Swenson used a similar concept to achieve significant sound absorption of a vibrating panel through the use of acoustic resonators, and without the use of porous materials. Another passive control technique that has been investigated to reduce low frequency structurally radiated noise is modal restructuring. The intent of modal restructuring is to induce mode shapes that inherently radiate minimal acoustic power. This has been achieved by placing optimally sized masses on a rectangular plate structure [6]. Substantial reductions in radiated power were realized over narrow, low frequency bands. Another effective low frequency control device is a passive tuned vibration absorber (TVA), which has been investigated to impede tonal and broadband motion of vibrating structures for almost a century now [7,8]. Many guidelines have been developed to design the mass, stiffness, and damping of the absorber to achieve optimal reduction in vibration levels, and therefore optimal sound reduction. In addition, the tuning and placement of the TVA(s) is critical for effective cancellation of vibration. The conventional approach proposes the placement of the TVA(s) on regions of high structural response often associated with the anti-nodes of a dominantly excited structural mode. Though proper tuning a TVA can reduce vibration levels by orders of magnitudes in a narrow frequency band, it is also well known that if improperly tuned the vibration levels and associated noise may consequently be increased.

Over the past decades, active control has emerged as a viable technology to solve the problem of low frequency noise radiated from structures. Active control has facilitated the use of loud speakers to destructively interfere with sound waves radiated from structures. This technique is known as active noise control (ANC) [9]. Similarly, active vibration control (AVC) utilizes a variety of actuators applied directly to the structure for reduction of vibration [10]. When these structural control inputs are used to minimize radiated sound from the structure, the technique is known as active structural acoustic control (ASAC). The two previous publications provide a thorough

understanding of control theory, potential actuators and sensors, and possible complications encountered with active sound or vibration control.

Another heavily researched control approach is the application of active skins to a radiating structure. In the work performed by Johnson [11], the surface of a structure is covered with control devices that radiate out-of-phase with the structure, effectively creating an array of active dipoles. In the 250-750 Hz frequency range, the devices achieved an overall sound power level reduction of 10 dB when applied to an aluminum plate. The advancement of active control has also allowed for the development of hybrid control techniques. Gentry developed a hybrid skin with PVDF actuators embedded in porous acoustic foam [12]. Through the addition of an active counterpart, this technique extends the high frequency control performance of the acoustic foam to a lower frequency range, yielding a global sound attenuation of about 10 dB up to 1200 Hz. The development of active control has also allowed the traditional tuned vibration absorber technology to be extended to adaptive and purely active absorbers. Adaptive absorbers have the capability of altering the absorber characteristics to adapt to variations in the system. Franchek, Ryan, and Bernhard present a robust tuning strategy for adaptive vibration control that revealed reductions up to 24 dBA [13]. Some complications encountered when implementing adaptive control into a realistic system are discussed by Aldrin and Conrad [14]. It was determined that the increased performance of an adaptive vibration absorber, over the traditional passive approach, was not cost effective in the case investigated. Active absorbers solely rely on a control algorithm to regulate an input force being applied to the reaction mass. Sun et. al. [15] gives an excellent overview of the various techniques for low frequency noise and vibration control using TVAs.

Additional work on active control has revealed that partitioning a structure or panel into acoustic dipole elements possesses the potential for volume velocity control at low frequencies and, thus, sound reduction. Volume velocity control has become a popular philosophy for the attenuation of low frequency structurally radiated noise. The intent of the concept is to convert a structure from an efficient radiator to a weak radiator through an acoustical point of view using of an acoustic dipole. The presence of a dipole

eliminates the need to reduce the vibrations of the structure. In work performed by St. Pierre, et. al. [16], a loudspeaker is embedded into a vibrating panel and used for active volume velocity control. The panel and loudspeaker make up the components of the created dipole source. In the low frequency range, a 10 dB reduction in sound power level was obtained. Other successful approaches similar to St. Pierre's, et. al. have been taken to effectively achieve active volume velocity control of structurally radiated noise [17-19]. Major differences primarily include the choice of sensors and actuators, while adhering to the underlying concept of active volume velocity control. Unfortunately, the complexity, power requirement, additional weight, unreliability, and high cost of active control systems have in general significantly limited their practical application to realistic systems.

1.2 Overview of Thesis

The intent of this thesis is to introduce and verify the new concept of a weak radiating cell as a low frequency passive noise control device as means of controlling unwanted structurally radiated sound. The uniqueness of the concept lies in the fact that the cell converts the motion of the vibrating structure into an inefficient radiating acoustic dipole source. The weak radiating cell concept presented in this thesis relies on an underlying volume velocity control approach executed through a purely passive method. This leads to the passive reduction of low frequency sound without the adverse effects introduced by active control.

Chapter 1 reviews various control approaches customary to the attenuation low frequency structurally radiated noise. In particular, and most relevant to this research, volume velocity control is discussed with several citations to previous work performed on active volume velocity control.

In Chapter 2, an overview of the well known monopole and dipole radiation theory is given for the sake of completeness. Then, the fundamental concept and overall goal of the weak radiating cell concept is introduced. Since the pioneering of the general concept provided two independent implementations of the idea, theoretical models are

derived in detail for each of the implementations. General acoustic responses and performances are also given for each implementation.

Numerical results from the cell models developed in Chapter 2 are presented in Chapter 3. For each implementation, realistic parameter dimensions and engineering material properties are used to give a practical performance prediction of a baseline cell. Variations on the baseline cell parameter values provide for a parametric study in which the system effects of each parameter are isolated. Also unique to this chapter, complex modeling issues are addressed for each implementation that were disregarded in the more general model development of Chapter 2.

Extensive experimental verification of the weak radiating cell concept is presented in Chapter 4. The verification begins with a single cell applied to a simple piston-like structure. Modal and source strength analyses are performed to evaluate the system and its performance. The experimental results are then compared to analytical predictions through system response characteristics and achieved performance levels. Though non-critical to the global scheme of the weak radiating concept in this work, the potential of enhancing the passive performance of the weak radiating cell concept by active means was also explored. The latter half of Chapter 4 presents the results of experiments in which an array of weak radiating cells is applied to a rectangular plate. These tests probe the effectiveness of the concept when applied to a complex radiating structure. Thorough analysis of the data reveals the successful creation of a dipole array, and sound power level reductions achieved from the application of the array of weak radiating cells.

Finally, Chapter 5 summarizes the efforts contained in this thesis and draws conclusions about the performance of the weak radiating cell concept. In addition, the practicality of application to realistic radiating structures is discussed.

Chapter 2

Theoretical Development

2.1 Introduction

In this chapter, relevant monopole and dipole radiation theory will first be reviewed. This will serve as a basis for the introduction to the fundamental concept of a weak radiating cell. Analytical models will be developed for each of the two weak radiating cell implementations. From the models, generalized response trends and system performance spectra will be analyzed. Also, general guidelines will be discussed for the achievement of optimal reduction.

2.2 Monopole and Dipole Radiation Theory

For the sake of completeness, a review of the well known monopole and dipole radiation theory will be included in this section. Though most any fundamental acoustics book contains a similar overview of the following radiation theory, Kinsler and Frey [20] was the primary reference source.

In the case where a radiating source has a closed surface, vibrates radially with an arbitrary velocity distribution, and has dimensions much smaller than the wavelength of the emitted sound, the source is termed to be a simple or monopole source. The surface of the monopole source displaces a volume of fluid at a rate termed complex volume velocity or source strength and is defined as

$$Qe^{i\omega t} = \int_S \vec{v} \cdot \vec{n} dS \qquad (2.1)$$

where $\vec{v}$ is the instantaneous velocity at a point on the surface, $\vec{n}$ is the unit outward normal to the surface element *dS*, and the integral is taken over the entire surface of the

source. The importance of source strength lies in the fact that if the dimensions of the source are much smaller than the wavelength of the radiated sound, then the details of the surface motion are not important. The source will radiate exactly the same sound as any other monopole source with the same source strength.

The radiated pressure and intensity at a point of distance r from a monopole source is respectively defined as

$$p(r,t) = i\rho c_a \frac{Qk}{4\pi r} e^{i(\omega t - kr)} \tag{2.2}$$

and

$$I(r) = \frac{p}{\rho c_a} = \frac{1}{8}\rho c \left(\frac{|Q|}{\lambda} \right)^2 \tag{2.3}$$

where ρ is the density of the surrounding fluid, c_a is the speed of sound, and k is the acoustic wavelength. Integration of the intensity over a sphere centered at the source gives the radiated power of a monopole

$$W = \frac{\pi}{2}\rho c_a \left(\frac{|Q|}{\lambda} \right)^2 \tag{2.4}$$

The monopole source can be used as a foundation to describing more complex radiators. Monopoles of different complex strengths may be combined to form multipole radiators. Here, the characteristics of a dipole source are discussed. A dipole consists of two closely spaced monopole sources of equal strength but 180° out-of-phase and separated by a distance much smaller than the acoustic wavelength, i.e. $kd << 1$ where , d is the distance between the sources. The pressure at a far-field point is the sum of the pressures produced by the individual sources and is given as

$$p(r,\theta,t) = -k^2 Qd \frac{\rho c_a}{4\pi r} \cos\theta \left(1 + \frac{i}{kr} \right) e^{i(kr - \omega t)} \tag{2.5}$$

where Q is the complex source strength of one of the monopoles and θ is the angle between the field observation point and the midpoint between the two sources, as shown in Figure 2.1. Though the sources are 180° out-of-phase and of equal magnitude, the

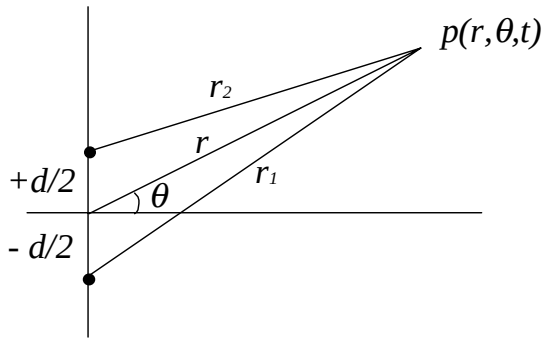

Figure 2.1 Geometry used in deriving the radiation characteristics of an acoustic dipole

the distance between the sources creates a phase difference and the pressure sum at the observation point is not necessarily zero.

The beneficial effects, in terms of sound reduction, of placing two monopoles of equal strength and opposite phase close to one another can be quantified by comparing its acoustic power W_d to the power of the monopoles W_m that form the dipole. This is given as

$$W_d = \frac{(kd)^2}{3} W_m \qquad kd << 1 \tag{2.6}$$

which shows the net radiated power of one of the monopoles is dramatically reduced by the second monopole that forms the dipole source. Thus, the creation of a dipole from two monopole sources is a very efficient method for the reduction of source strength and acoustic power.

2.3 Theory of a Generalized Weak Radiating Cell

The radiation theory presented in the previous section can be employed to suggest that if the volume velocity of a source is nearly zero and the wavelength is much larger than the source dimension, such as in a dipole, the radiated power is consequently minimized. Thus, an efficient method to reduce the sound radiation from a structure would be to partition the surface of the structure into small sectors each of which would independently respond as a dipole with zero volume velocity. To this end, the concept of a weak sound radiating cell is introduced to reduce, in particular the low frequency, radiated noise from structures.

A weak radiating cell is a device that consists of two coupled surfaces such that, when placed on a vibrating structure, the responses of the two surfaces are nearly out-of-phase and of equal strength over a wide frequency range. This leads the motion of the surfaces to behave as an acoustic dipole and thus as a poor sound radiating source. Recall that the dimensions of the surfaces must be much smaller than the wavelength of the radiated sound to qualify as monopoles. Furthermore, the monopoles must comply with the restriction placed on the distance between the two sources, i.e. $kd << 1$.

The concept of a weak radiating cell is illustrated in Figure 2.2. The problem is initiated by a structure radiating sound into the surrounding fluid as shown in Figure 2.2a. The sound power radiated by a small area, S_s, with dimensions smaller than the acoustic wavelength, is determined by its source strength, $Q_s = v_s S_s$ where v_s is the average normal velocity component over the small area. For simplicity, at low frequencies the velocity response of the structure can be considered as nearly uniform over this area S_s which in turn radiates sound as a monopole source. Note that the total radiated power from the plate is due to the contribution of all the areas of the structure including their far-field coupling. Figure 2.2b illustrates a weak radiating cell covering the surface S_s. The concept of the weak radiating cell is to convert the motion of the small area from that of a monopole into a dipole source. To this end, the motion of the nearly uniform velocity v_s of the surface S_s is transformed into the motion of the two surfaces S_{c1} and S_{c2} with velocities v_{c1} and v_{c2}, respectively. The cell is then designed such that the motion of these two surfaces are out-of-phase and of relative magnitude that leads to $v_{c1}S_{c1} + v_{c2}S_{c2} \cong 0$. Conceptually, by covering the structural surface with an array of cells as shown in Figure 2.2c, the response of the structure is converted to that of an array of dipoles. Thus, leading to an essentially zero volume velocity structural source with minimum sound radiation. The weak radiating cell will behave as a dipole source for frequencies that the wavelength is much larger than the cell dimensions. Thus, the size of the cell will determine the expected frequency range of sound reduction, i.e. the smaller the source the wider the range.

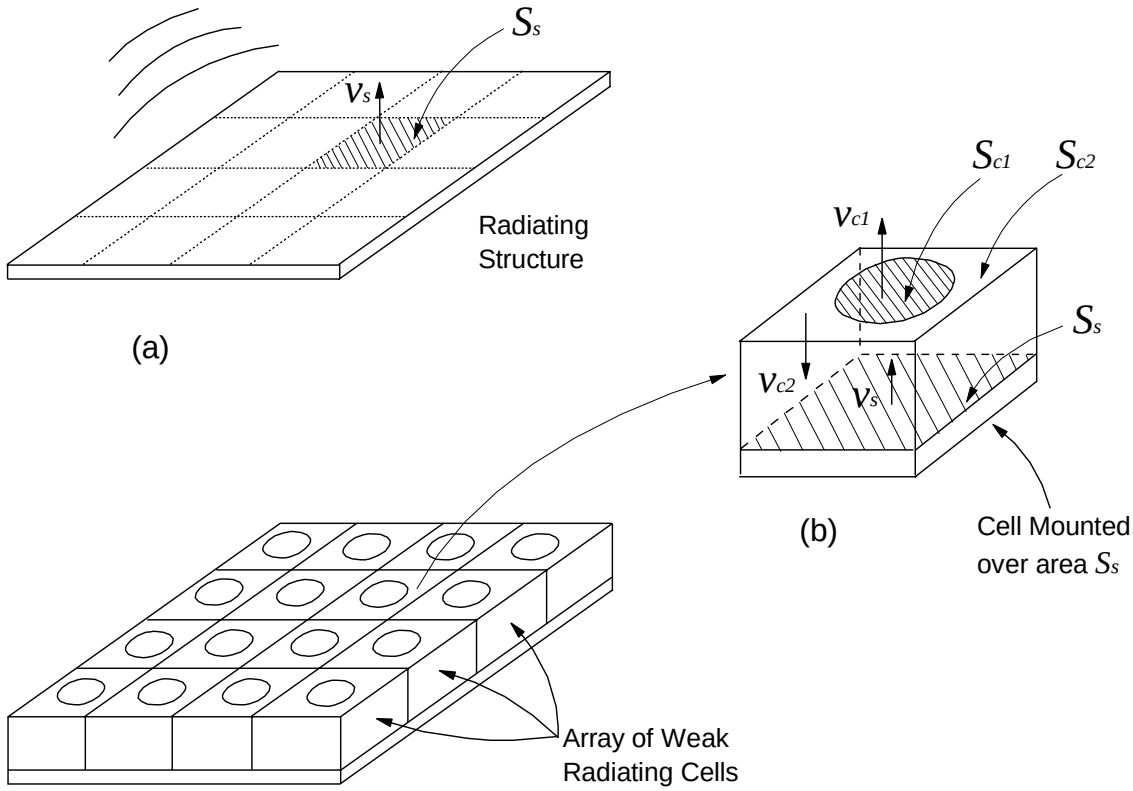

Figure 2.2 Attenuation of low frequency structurally radiated sound using the weak radiating cell concept: (a) untreated plate, (b) single cell, (c) plate with array of cells

It is important to remark that researchers have proposed active control methods to minimize the volume velocity of small panels [16-19]. This purely active approach can have significant drawbacks that could limit its applicability in real systems. For example, the extra weight of the control element, the complexity, reliability and cost of the controller, and so forth. A more efficient method would be to first obtain volume velocity cancellation passively, as proposed in this work, and then implement active control to further enhance the performance of the system if so desired. The hybrid approach has been experimentally investigated and the results will be examined in the later experimental results chapter.

2.4 Implementations of the Concept

The pioneering of the weak radiating cell concept has evolved into various independent implementations of the concept. While other implementations have been investigated, two of the best performing cell implementations will be theoretically derived and analyzed in detail. The first implementation possesses mechanically coupled surfaces whereas the second has mechanically and acoustically coupled surfaces in order to generate the desired dipole effect.

Without loss of generality and for the sake of clarity, the small area S_s of the offensive structure is assumed to be a circular piston with uniform velocity, v_s. This assumption will be effective for the analysis of each implementation of a single weak radiating cell. Hence for geometric consistency and without loss of generality, the cell will also adhere to a circular configuration.

2.4.1 Mechanically Coupled Cell

The first implementation of the weak radiating cell concept is illustrated in Figure 2.3a. Termed mechanically coupled, the cell has two surfaces that are both coupled to the structure through mechanical components. The cell contains a hallow rigid element with a surface area, S_{c2}, which is mounted to the radiating structure surface. Because this element is assumed to be very stiff, the velocity of the surface S_{c2} is assumed to be same as the velocity of the structure, $v_{c2} \cong v_s$. The second radiating surface of the cell, S_{c1}, is

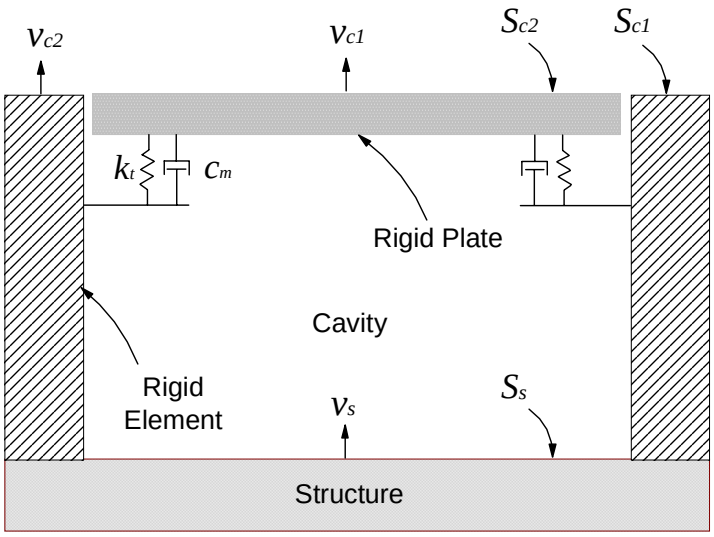

(a)

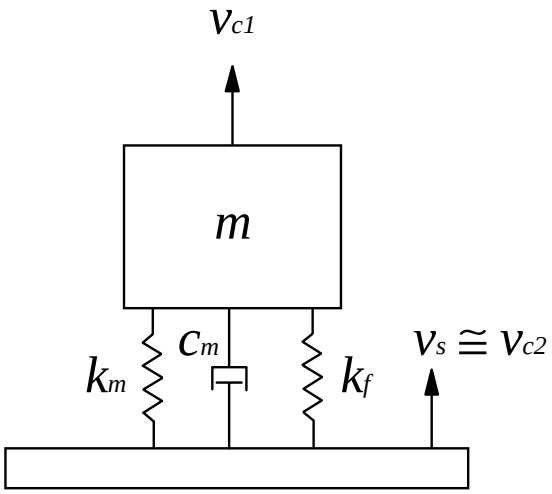

(b)

Figure 2.3 Mechanically coupled cell, (a) Implementation and (b) Simplified model

obtained by attaching a rigid plate to the rigid element through a flexible mounting system which creates a sealed cavity. The mounting system should allow for stiffness in the radial direction with compliance in the axial direction.

As a first attempt, the mechanical behavior of the cell can be depicted as a single degree-of-freedom (dof) lumped parameter system with a base input. The simplified model is shown in Figure 2.3b. With a detailed derivation contained in Appendix A, the equation of motion for the simplified model is

$$m_p \ddot{x}_{c1} + c_m \dot{x}_{c1} + k_t x_{c1} = c_m \dot{x}_s + k_t x_s \tag{2.7}$$

where m_p is the system mass, c_m is the damping in the mounting system, k_t is the total stiffness of the system $k_m + k_f = k_t$ with k_m being the mechanical stiffness of the mounting system and k_f the stiffness due to the compressibility of the fluid in the cavity, and x_{c1} and x_s are the displacements of surfaces S_{c1} and S_s, respectively. A dot over a variable indicates differentiation with respect to time.

Assuming harmonic input, Eq. (2.7) can be transformed to the frequency domain and then written in terms of velocity as follows

$$\left(i\omega m_p + c_m + \frac{k_t}{i\omega} \right) v_{c1} = \left(c_m + \frac{k_t}{i\omega} \right) v_s \tag{2.8}$$

The complex source strengths for the two radiating surfaces of the cell can then be computed in terms of the system parameters and input velocity. They are given by

$$Q_{c2} = v_s S_{c2} \tag{2.9}$$

for the rigid element surface and

$$Q_{c1} = v_{c1} S_{c1} \tag{2.10}$$

for the plate surface. The net source strength radiated from the cell is $Q_c = Q_{c2} + Q_{c1}$. To be used as a basis, the complex source strength at low frequencies of the original structure, the piston, is given as

$$Q_s = S_s v_s \tag{2.11}$$

For low frequency, the acoustic power can be computed for each radiating surface from the source strength as [20]

$$W = \frac{\alpha}{2}\pi\rho c\left(\frac{|Q|}{\lambda}\right)^2 \qquad \lambda >> a \tag{2.12}$$

where α = 1 for a free-field source and 2 for a baffled source, a is the piston radius, ρ is the fluid density, c is the speed of sound, and λ is the acoustic wavelength.

The performance of the cell is determined from the reduction in sound power between the piston and cell systems, which is defined as

$$\Gamma = W_s - W_c \tag{2.13}$$

where W_s and W_c are the acoustic power radiated from the structure and cell, respectively.

For the sake of describing the acoustic behavior of the cell, the source strengths in Eqs. (2.9) and (2.10) are plotted in Figure 2.4 as a function of frequency normalized by the natural frequency of the plate-cavity system, $\omega_n = \sqrt{k_t / m_p}$. From Eq. (2.12), the acoustic power of the piston and cell are plotted in Figure 2.5. Computed from Eqs. (2.11) and (2.12), Figure 2.6 reveals the sound power level reduction achieved by applying the weak radiating cell to the piston.

The general response of the cell can be described for the following frequency regions: below, around, and above the resonance of the plate-cavity system. It can be seen in Figure 2.4 that below the natural frequency of the system, the motion of the two surfaces are in phase and the sound radiated by the two surfaces add to obtain the net radiation of the cell. At frequencies well below resonance, $f/f_n \leq 0.4$, the velocities of the two surfaces are nearly the same, and thus the cell radiates the same acoustic power as the original structure as seen in Figure 2.5. When the frequency is around resonance, the plate response greatly exceeds that of the piston due to dynamic amplification, and the relative phase goes through a 180° variation. The plate motion completely dominates the system response resulting in an overall increase in the sound radiation from the structure. After resonance, the motion of the two surfaces is out-of-phase and the radiation from the

surfaces subtract producing sound reduction. Selecting proper areas will minimize the source strength of the resulting cell over a wide frequency range leading to the consequent sound reduction. To achieve optimal reduction, the resonance of the system should be placed below the frequency range of desired reduction. In addition, the surface area ratio S_{c2}/S_{c1} should be determined so the source strengths are precisely equal, effectively creating a perfect dipole, at a frequency above the resonance where maximum sound reduction is desired. In Figure 2.6, the increase in the sound power level is visualized at the resonant frequency, but more importantly, notice the region of maximum reduction around the frequency ratio of 2.18 where a perfect dipole is created.

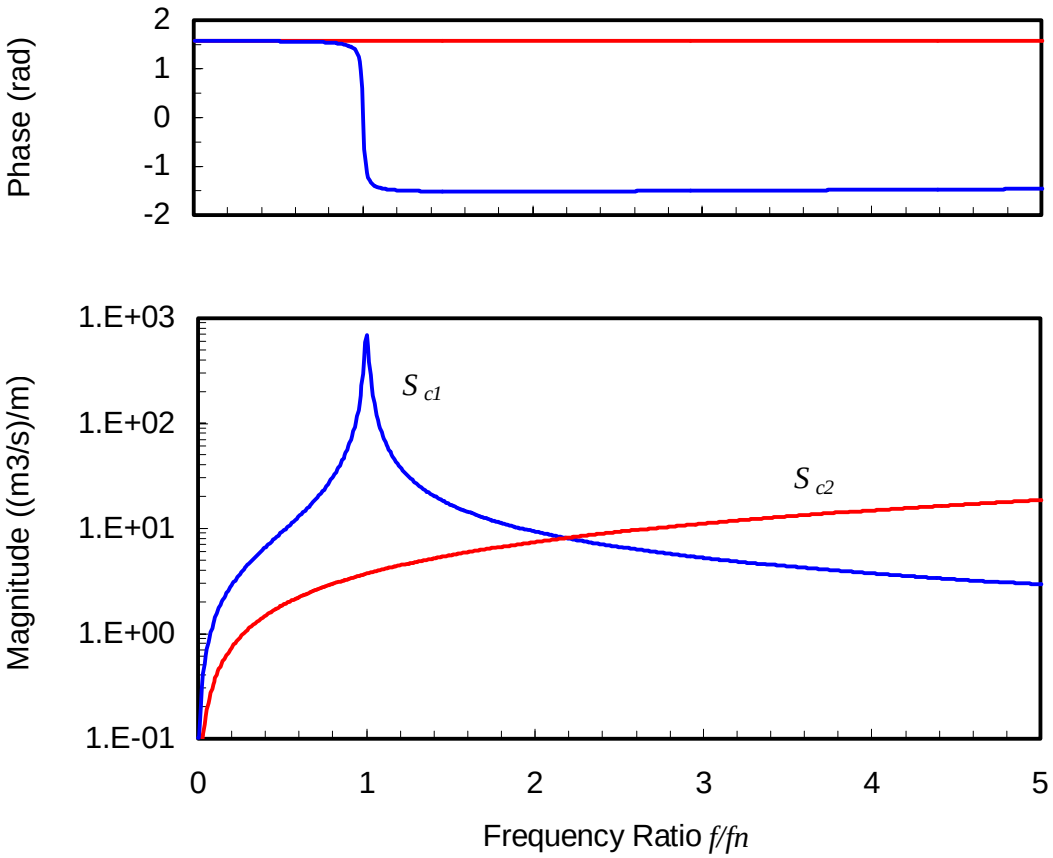

Figure 2.4 Source strength of surfaces S_{c1} and S_{c2}

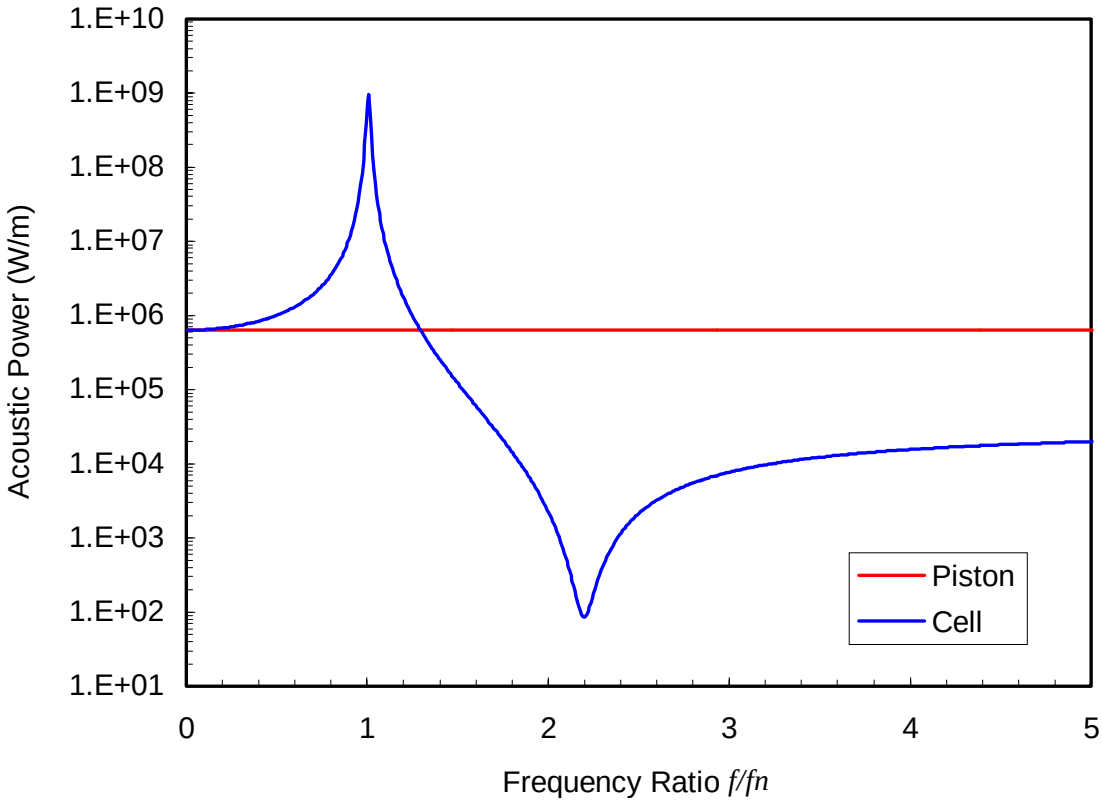

Figure 2.5 Acoustic power of piston and cell

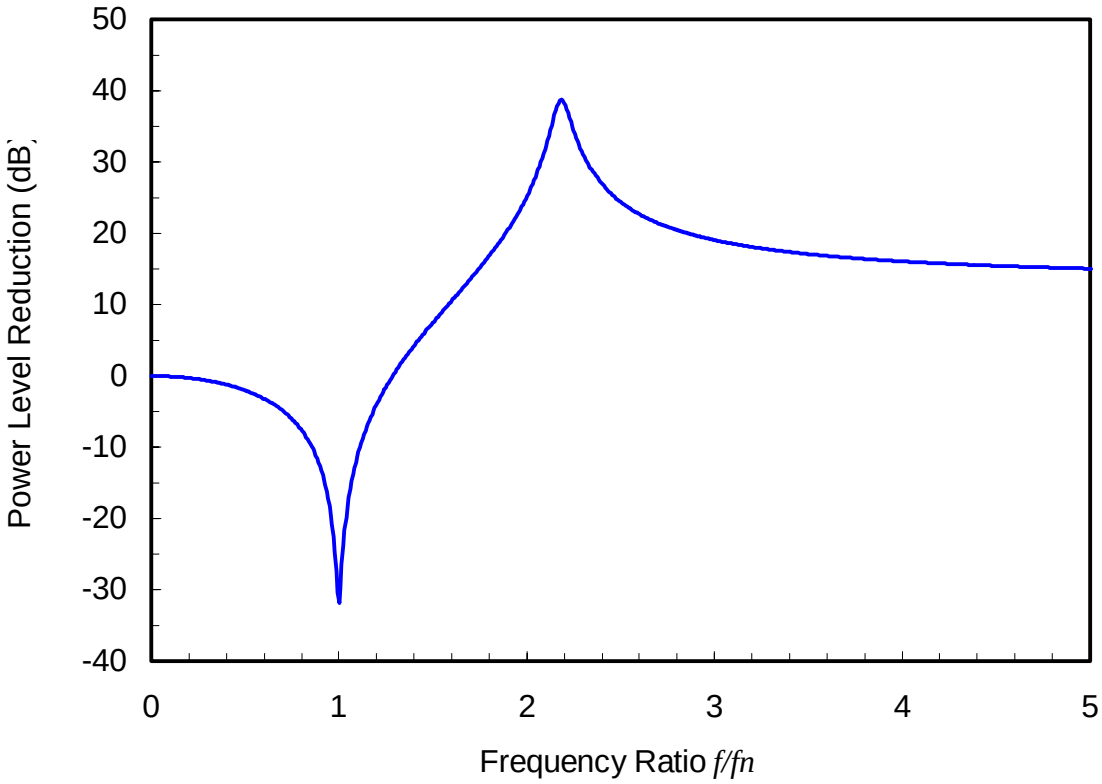

Figure 2.6 Sound power level reduction for mechanically coupled cell

2.4.2 Mechanically and Acoustically Coupled Cell

The second implementation of the weak radiating cell concept is illustrated in Figure 2.7a. This implementation is termed mechanically and acoustically coupled because one surface is mechanically linked to the structure while the other is coupled to the structure through the cavity. The cell consists of a rigid plate with an orifice and an elastic hallow element that connects the plate to the vibrating piston creating a cavity. The plate is one of the radiating surfaces of the cell with an area S_{c2}, which is bounded by radii b and c. Sound is generated by the oscillatory motion of the fluid through the orifice, which has a radius of c and forms the second radiating surface, S_{c1}. The motion of the fluid in the orifice, or neck, behaves as an inertial element. The combination of the radiation from the plate and orifice creates the dipole effect for this implementation of a weak radiating cell. The dynamic behavior of this implementation is more involved than that of the previous mechanically coupled implementation. The cavity and orifice behave as an acoustic or Helmholtz resonator [21]. This resonator is excited by the change in the cavity volume due to the relative displacement between the plate and the piston. On the other hand, the plate and the elastic element form a mechanical oscillator excited by the motion of the structure. The acoustic and mechanical radiator components are coupled through the cavity internal acoustic pressure. The behavior of this system can be investigated by developing a simplified two degree-of-freedom lumped parameter model of the system, illustrated in Figure 2.7b. The motion of the plate and orifice fluid are the two dof's. Appendix B contains a detailed derivation of the equations of motion for the system.

From the free-body diagram, the equilibrium equation for the plate is given as

$$m_p \ddot{x}_{c2} + c_m \dot{x}_{c2} + k_m x_{c2} + p\left(S_c - S_{c1}\right) = c_m \dot{x}_s + k_m x_s \qquad (2.14)$$

where m_p is the mass of the plate, k_m and c_m correspond to the mechanical stiffness and damping of the elastic medium, p is the acoustic pressure developed inside the cavity, S_c is the surface area of the cavity formed by radius b, and x_{c2} and x_s are the displacements of the plate and structure, respectively. Assuming the fluid loading on the plate is negligible, p is the net pressure acting on the area of the plate facing the cavity, i.e (S_c-S_{c1}).

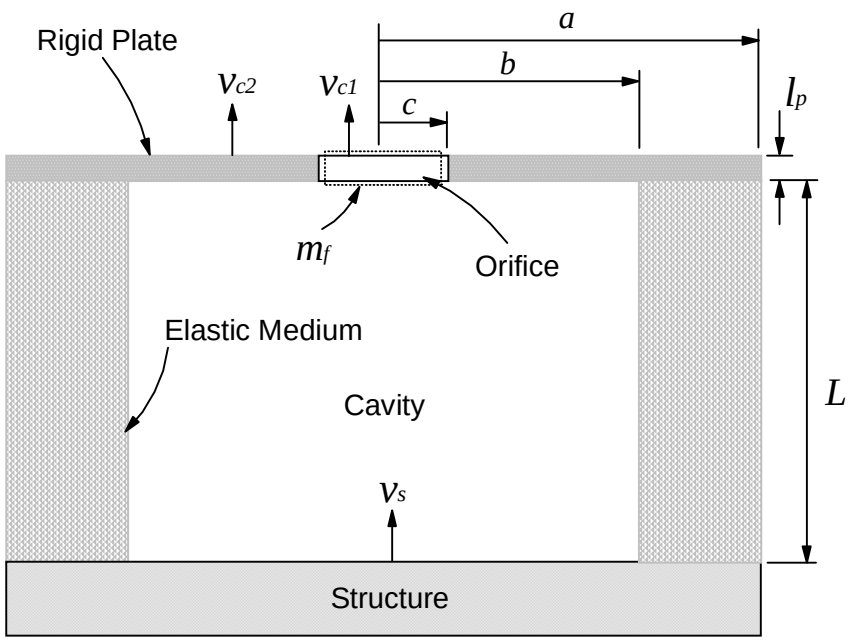

(a)

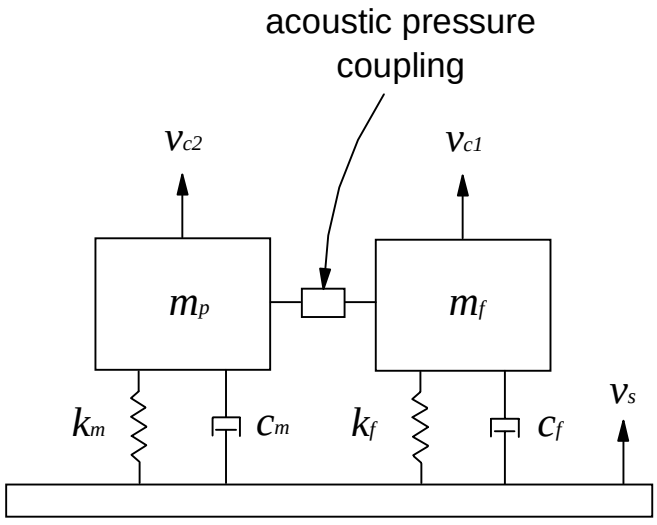

(b)

Figure 2.7 Acoustically and mechanically coupled cell, (a) Implementation and (b) Simplified model

On the other hand, the force balance on the fluid in the orifice is given as

$$m_f \ddot{x}_{c1} + pS_{c1} = 0 \tag{2.15}$$

where m_f is the mass of the fluid in the orifice, or resonator neck, with displacement x_{c1}. The second term is due to the acoustic pressure acting on the fluid mass of area S_{c1}.

It is clear from Eqs. (2.14) and (2.15) that the mechanical and acoustic systems are coupled through the internal acoustic pressure. The acoustic pressure is defined as the difference between the instantaneous pressure and the static equilibrium pressure. Assuming the fluid in the cavity is inviscid and the acoustic processes in the fluid are adiabatic, the acoustic pressure derivation is contained in Appendix A and given as

$$p = -\frac{c_a{}^2 \rho \Delta V}{V_o} \tag{2.16}$$

where ρ is the fluid density, c_a is the speed of sound, V_o is the initial volume of the cavity and ΔV is the change in volume.

The change in volume is due to the relative motion between the piston, plate, and fluid in the orifice. The volume change is given as

$$\Delta V = x_{c2}\left(S_c - S_{c1}\right) - x_s S_c + x_{c1} S_{c1} \tag{2.17}$$

which is useful to describe the interaction between the mechanical and acoustic components. The combination of the first and second terms defines the change in volume due to the relative motion between the structure and the plate. The volume increases when $x_{c2} > x_s$ and therefore decreases the acoustic pressure. The pressure developed in the cavity due to this change in volume excites the dynamics of the Helmholtz resonator, which introduces the last term in Eq. (2.17). It reflects the volume change due to the displacement of the fluid in the neck.

Replacing Eqs. (2.17) into (2.16) and this into (2.14) and (2.15) and then assuming harmonic input, the equilibrium equations can be written in matrix form as

$$\begin{bmatrix} i\omega m_p + c_m + \dfrac{k_m}{i\omega} + \dfrac{c_a{}^2 \rho (S_c - S_{c1})^2}{i\omega V_o} & \dfrac{c_a{}^2 \rho S_{c1}(S_c - S_{c1})}{i\omega V_o} \\ \dfrac{c_a{}^2 \rho S_{c1}(S_c - S_{c1})}{i\omega V_o} & i\omega m_f + c_f + \dfrac{k_f}{i\omega} \end{bmatrix} \cdot \begin{Bmatrix} v_{c2} \\ v_{c1} \end{Bmatrix}$$

$$= \begin{bmatrix} c_m + \dfrac{k_m}{i\omega} + \dfrac{c_a{}^2 \rho S_c (S_c - S_{c1})}{i\omega V_o} \\ \dfrac{c_a{}^2 \rho S_{c1} S_c}{i\omega V_o} \end{bmatrix} \cdot v_s \qquad (2.18)$$

where k_f is the stiffness due to the fluid in the cavity assuming no relative motion between the plate and piston and c_f is acoustic damping term of the orifice. Note that this system has two resonant frequencies.

Referring to Eq. (2.18), the equations of motion of the two dof system are symmetric. The coupling between the mechanical and acoustical systems is stiffness-like. The positive off-diagonal term in the matrix indicates that when the plate is displaced in its positive direction, the pressure in the cavity decreases and the fluid mass is thus moved in the negative direction.

Using Eq. (2.18), the complex source strengths of the two radiating surfaces can be computed in terms of the system parameters and input velocity. The complex source strength for the plate is given by Eq. (2.9) from the previous section while the orifice source strength is given by Eq. (2.10). The net source strength from the cell is $Q_c = Q_{c1} + Q_{c2}$. The source strengths phase and magnitudes for the cell components are plotted in Figure 2.8 as a function of frequency normalized by the first resonance of the system. At low frequencies, the radiated acoustic power is given by Eq. (2.12) and the sound power reduction by Eq. (2.13). Figure 2.9 illustrates the radiated sound power for the cell and piston while Figure 2.10 plots the achieved sound power level reduction.

In Figure 2.8, the two resonances of the two dof system are clearly identified. For convenience, the resonances are referred to as the mechanical and acoustic resonances, respectively. The first resonance is dominated by the plate oscillations while the large fluid motion at the orifice characterizes the second. From Figure 2.8, five frequency

regions are identified in the response of this cell: below the mechanical resonance, between the two resonances, above the acoustical resonance, and finally around each of the resonances. It is clear that this cell implementation behaves as a dipole in the frequency region between the resonances since the sources are nearly out-of-phase. As seen at resonance of the mechanically coupled cell implementation, Figures 2.9 and 2.10 show an increase in radiated sound at the resonances of this system. However, sound reduction is achieved throughout the frequency bandwidth between the resonances with maximum reduction at the frequency ratio of 2.76 where a perfect dipole is created. To achieve optimal reduction, the first resonance should be placed below the frequency range of interest while placing the second resonance above. Also, the surface areas of the plate, orifice, and cavity should be optimized as to place the maximum reduction at a desirable frequency between the two resonances of the system.

Through the simple models developed, the performance of the two cell implementations can be compared. The mechanically coupled cell is most likely simpler to implement and has less adverse dynamic behavior compared to the second cell, i.e. one resonance as opposed to two resonances of the mechanically and acoustically coupled cell. On the other hand, the performance of the second cell implementation is better than the first, achieving higher power reduction over a wider frequency range.

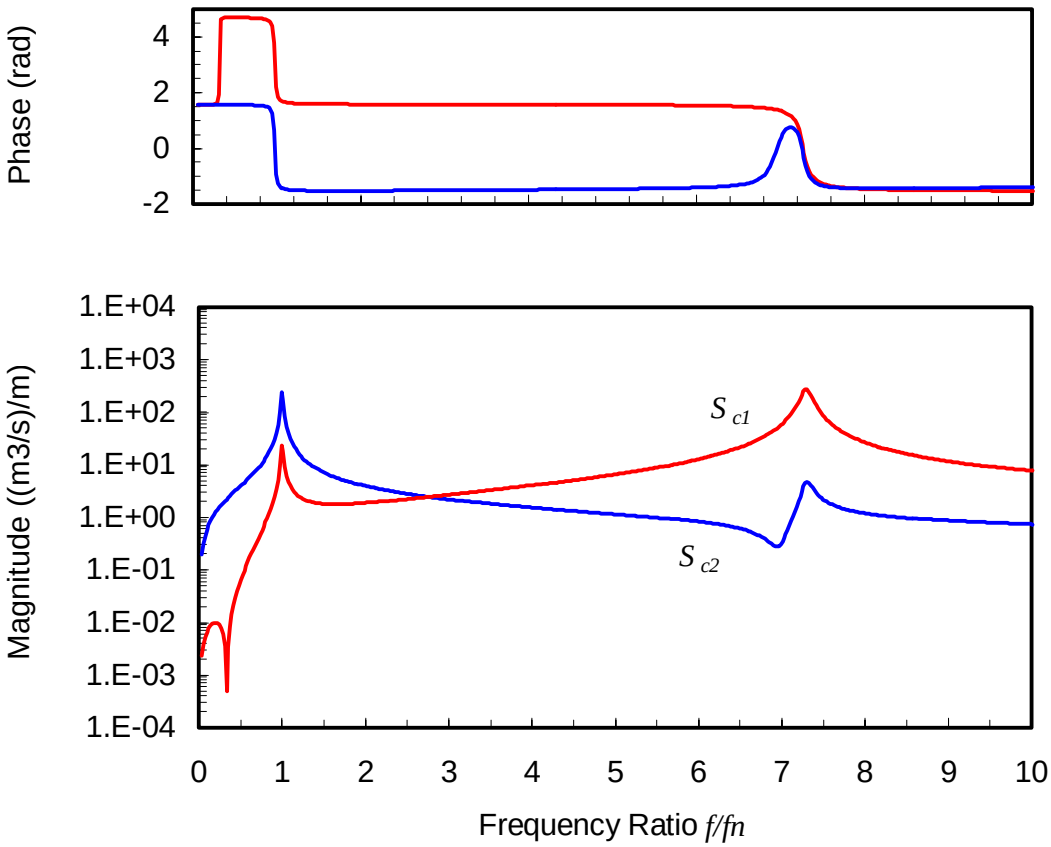

Figure 2.8 Source strength of surfaces S_{c1} and S_{c2}

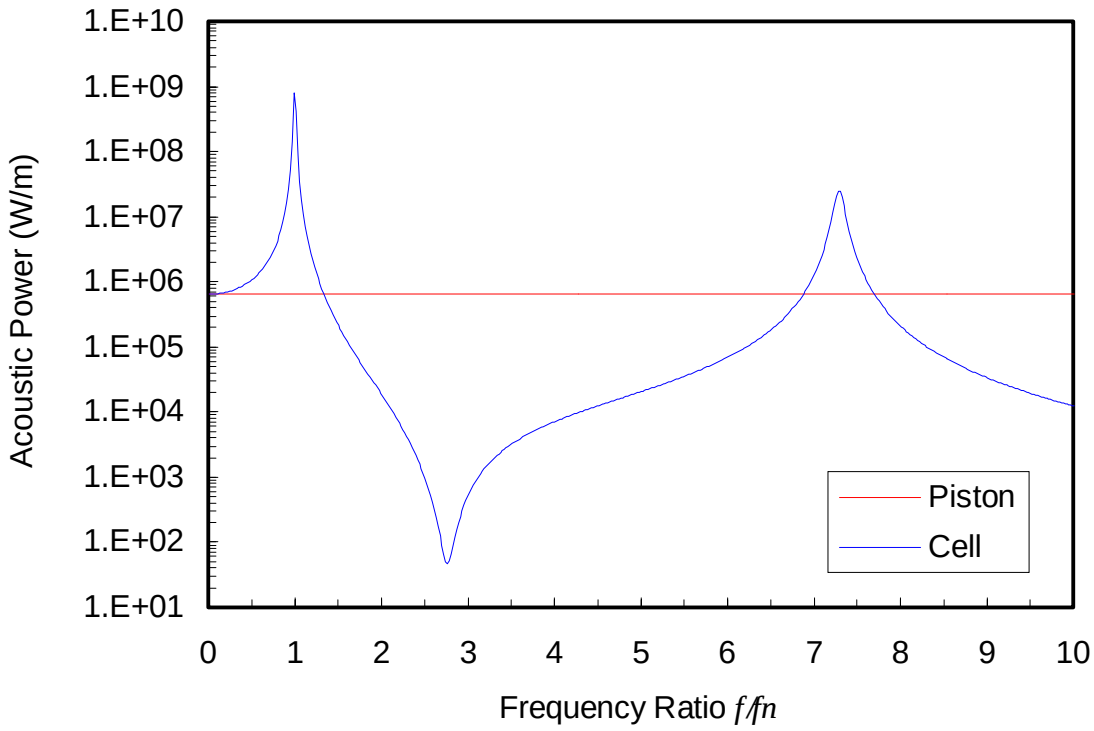

Figure 2.9 Acoustic power of piston and cell

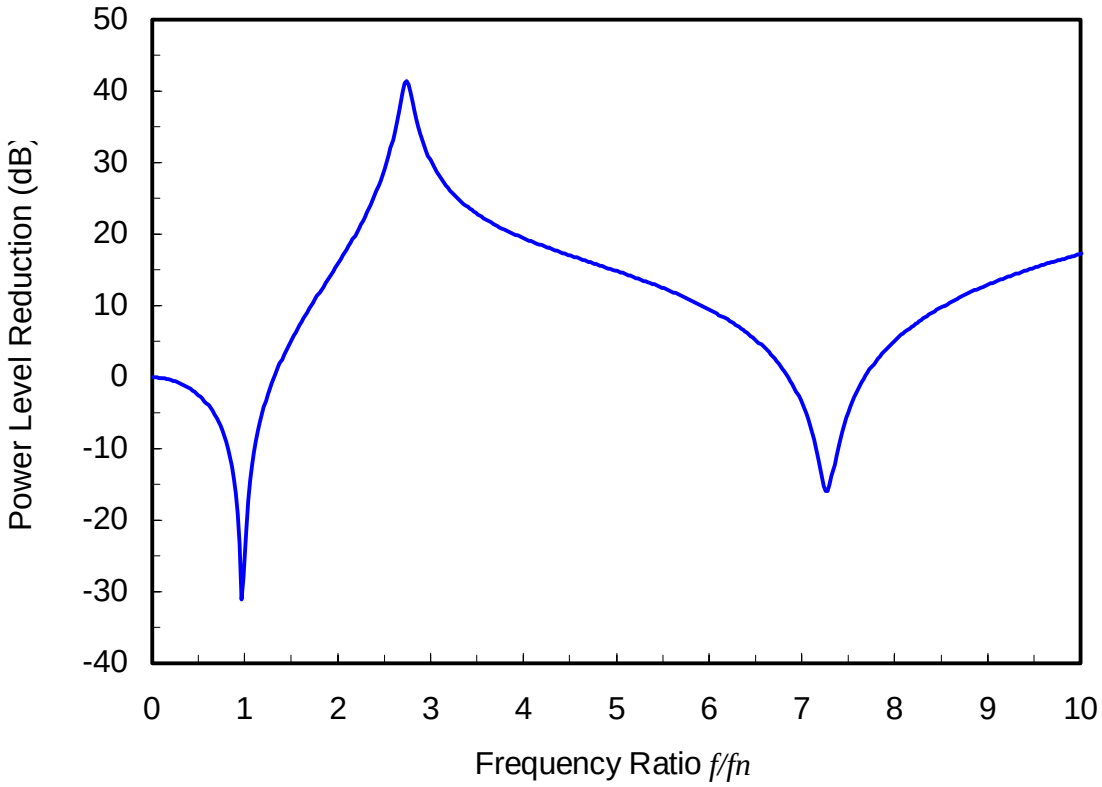

Figure 2.10 Sound power level reduction for mechanically and acoustically coupled cell

Chapter 3

Numerical Results

3.1 Introduction

The simplified models developed and properties used in the Chapter 2 served the purpose of introducing the concept of the weak radiating cell as well as to gain some insight into the behavior of two independent cell implementations. In this chapter, parameters from realistic engineering materials will be used to study the system response and performance of each cell, which will be used to assess the practicality of the concept and its implementations. Since the goal of the weak radiating cell is principally, but not exclusively, to reduce the sound radiation at frequencies below 1000 Hz, the design of the baseline cells is defined to achieve this goal. Due to the generality of the previous chapter, the investigation of several modeling techniques was neglected and will be resolved in this chapter. In addition, the influence on the cell performance to parameter variations will also be investigated for each implementation. For simplicity and conciseness, the sound power level reduction is used as means of characterizing the effects of the parameter variations. Though the goal is to achieve reduction below 1000 Hz, the analysis will investigate frequencies up to 1600 Hz to help establish an upper limit of performance.

3.2 Mechanically Coupled Cell

3.2.1 Physical Implementation

In the previous chapter, the physical implementation details of the mechanically coupled weak radiating cell were omitted for the sake of generality. In addition to providing realistic materials and material properties, a practical implementation is given for the flexible mounting system required to attach the rigid plate to the hallow rigid element.

Figure 3.1 illustrates the mechanically coupled cell with a realistic physical implementation of the mounting system. A thin flexible shim serves as means of attaching the plate to the rigid element while achieving the desired plate motion in order to create a dipole effect. The shim should be designed to be flexible in the vertical direction while providing some degree of stiffness in the plane normal to the intended motion. The intent is to limit the excitation of undesirable modes in the radial direction for the frequency range of concern. A snapshot of the predicted dynamic motion for the plate and shim is given in Figure 3.1, designated by dashed lines. Notice the motion is solely in the vertical, or axial direction. One option for the attachment of the plate to the rigid element would be to use a speaker suspension ring. However, it is assumed here that the shim is constructed of brass (Modulus of Elasticity E = 104GPa, density ρ = 8500 kg/m^3, and loss factor η = 0.01) with a uniform thickness of l_s and radius of a. The dimensions of the system parameters selected as baseline values are tabulated in Table 3.1.

The rigid element is assumed here to be built from epoxy foam, commercially known as structural foam used in the automotive industry [22]. The advantage of this material is its high Modulus of Elasticity (E = 642 MPa) and low density (ρ = 480 kg/m^3) which is advantageous to minimize the overall weight of the cell. Minimizing the weight is a critical goal in some applications such as in aircraft interior noise. Other materials such as composite and honeycomb structures are also possible. The fundamental resonance of the rigid element without the center plate and shim is 3623 Hz, which is outside the frequency range of interest [23].

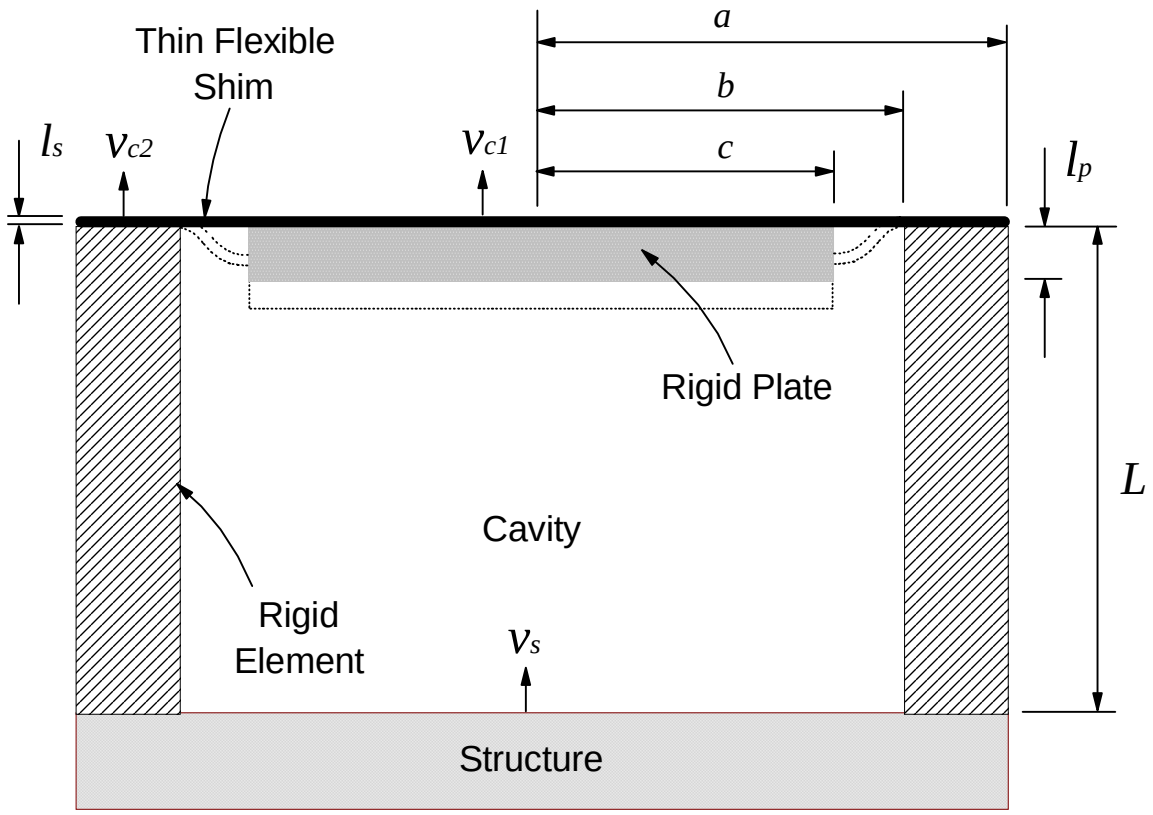

Figure 3.1 Mechanically coupled cell implementation illustrating the use of a thin flexible shim to serve as the mounting system for the rigid plate

Table 3.1 System parameters for mechanically coupled baseline cell

Description	Variable	Value
Piston radius	a	57.2 mm
Cavity radius	b	50.8 mm
Plate radius	c	38.1 mm
Plate thickness	l_p	6.4 mm
Shim thickness	l_s	0.2 mm
Cavity height	L	50.8 mm
Shim damping ratio	ζ	0.01

The circular central plate, which partially forms the second surface, should have the necessary mass for the desired dynamics and sufficient bending stiffness to essentially behave as a rigid plate in the frequency region of interest. Though a number of materials can be used, this plate is assumed here to be made of Plexiglas (Modulus of Elasticity E = 2758 Mpa, Poisson's ratio σ = 0.4, and density ρ = 1300 kg/m^3) with a thickness of l_p = 6.4 mm and a radius of c = 38 mm. With these parameters, the fundamental bending plate resonance is 8811 Hz, which is again outside the frequency range of interest [24].

As mentioned above, the size and weight of sound attenuating devices is typically critical to the engineering problem at hand. Therefore, the goal is to minimize the dimensions of the system components and to utilize materials with minimal density properties. On the other hand, achieving optimal reduction and retaining structural integrity is also a chief concern. For the realistic dimensions and material properties assumed for this numerical analysis, the overall height and mass of the cell are 51 mm and 108 g, respectively. Based on typical passive or active control approaches, the size and weight of the weak radiating cell is favorable to the goals of noise reduction techniques.

3.2.2 Modeling Techniques

In the theoretical section of Chapter 2 it was assumed that the two surfaces of the mechanically coupled cell were clearly identified. However, with the implementation of the flexible shim as the spring-damper mounting system, the surface cannot be discretely defined. This is because the shim has a velocity distribution that varies from v_p at $r = c$ to v_s at $r = b$ where r is the radius from the center of the cell. Thus, the volume velocity of the cell is computed by integrating [20]

$$Q_c = \int_0^r v(r) 2\pi r dr \tag{3.1}$$

where the velocity distribution is defined as

$$v(r) = \begin{cases} v_p = \dfrac{c_m + \dfrac{k_t}{i\omega}}{i\omega m_p + c_m + \dfrac{k_t}{i\omega}} & 0 \le r \le c \\ v_h = \dfrac{v_p + v_s}{2} + \cos\left(\dfrac{\pi r}{b-c}\right) \cdot \dfrac{v_p - v_s}{2} & c < r < b \\ v_s & b \le r \le a \end{cases} \tag{3.2}$$

where the velocity profile across the surface of the shim, $c < r < b$, is assumed to simulate a half-period cosine function. The system mass, m_p, includes both the mass of the rigid plate and the equivalent mass of the shim.

The system stiffness, k_t, in Eq. (3.2) is defined as the combination of the shim mechanical stiffness and the stiffness due to the fluid in the cavity. Assuming clamped boundary conditions, the stiffness of the annular shim can be computed from the work by Leissa [24]. The stiffness due to the fluid in the cavity is computed from the internal acoustic pressure, p, given by Eq. (2.17). In this case, the change in volume within the cavity is $\Delta V = (x_{c1}\text{-}x_s)S_{c1}$. Performing a force balance on the surface S_{c1} reveals the additional stiffness to the system due to the fluid in the cavity is given as

$$k_f = \frac{c_a^2 \rho S_{c1}^2}{V_o} \tag{3.3}$$

The internal damping of the shim, c_m, is modeled as viscous damping and is given as [23]

$$c_m = 2\zeta\omega_n m_p \tag{3.4}$$

where ζ is the damping ratio, ω_n is the system resonant frequency, and m_p is the system mass.

Using Eq. (3.1), the source strength of the baseline cell was computed and is plotted in Figure 3.2. The source strength of the piston, computed from Eq. (2.12), is also included. This figure shows that the resonance of the cell is at 276 Hz while the

frequency at which a perfect dipole is created is 426 Hz. After the resonance of the cell, reduction is achieved starting at 338 Hz and then throughout the frequency band.

3.2.3 Parametric Study

The parameter values given in Table 3.1 will be used as a baseline for each parametric case study on the mechanically coupled cell implementation of the weak radiating cell concept, with the exception of the parameter(s) affected by that specific case study.

The first parameter investigated is the ratio of the two radiating surfaces. This can be achieved by changing the ratio of the inner, *c*, to outer, *b*, radii of the shim. It is assumed that the mass of the center plate does not change while the thickness of the shim is adjusted to keep the same natural frequency of the system. Figure 3.3 reveals that the frequency of maximum sound reduction is sensitive to the area ratio as well as the overall reduction, which improves as the ratio *c*/*b* increases. Note that the heavy line represents the reduction using the baseline cell design parameters. This representation is also included in Figures 3.4 and 3.5.

The next parameter to be investigated is the system resonant frequency. This can be altered by changing either the thickness or density of the plate to affect the mass and/or by changing the shim thickness to modify the stiffness. In this study, the shim thickness was held constant while the mass was changed. The resulting sound power reductions are shown in Figure 3.4. As expected, the frequency of maximum reduction occurs at lower frequencies as the mass is increased. However, the maximum level of power reduction is insensitive to the mass. Another interesting factor is the ratio of the frequency of maximum reduction to the natural frequency. This ratio decreases with the natural frequency of the system. It is important to minimize the overall weight of the cell for some applications; so, the mass should be minimized which implies a minimization of the stiffness to yield a predetermined resonance frequency. The lowest stiffness is bounded by the size of the air cavity assuming negligible contribution from the shim. For further reduction in the weight, the height of the cavity can be decreased, which however

increases the cavity stiffness. Note that as the size of the cell is proportionally reduced, the stiffness due to the fluid decreases in the same proportion as the cell size.

One approach to alleviate the increase in the radiated power at frequencies near the resonance is by introducing damping. Thus, the effect of the shim damping ratio on the system response is examined and shown in Figure 3.5. As expected, increasing the energy dissipation leads to a reduction at resonance. However, it also decreases the maximum sound reduction because it affects the relative phase between the motion of the two surfaces, i.e. the two surfaces are not out of phase as the damping increases. Consequently, there is a sound reduction trade off to introducing damping into the system.

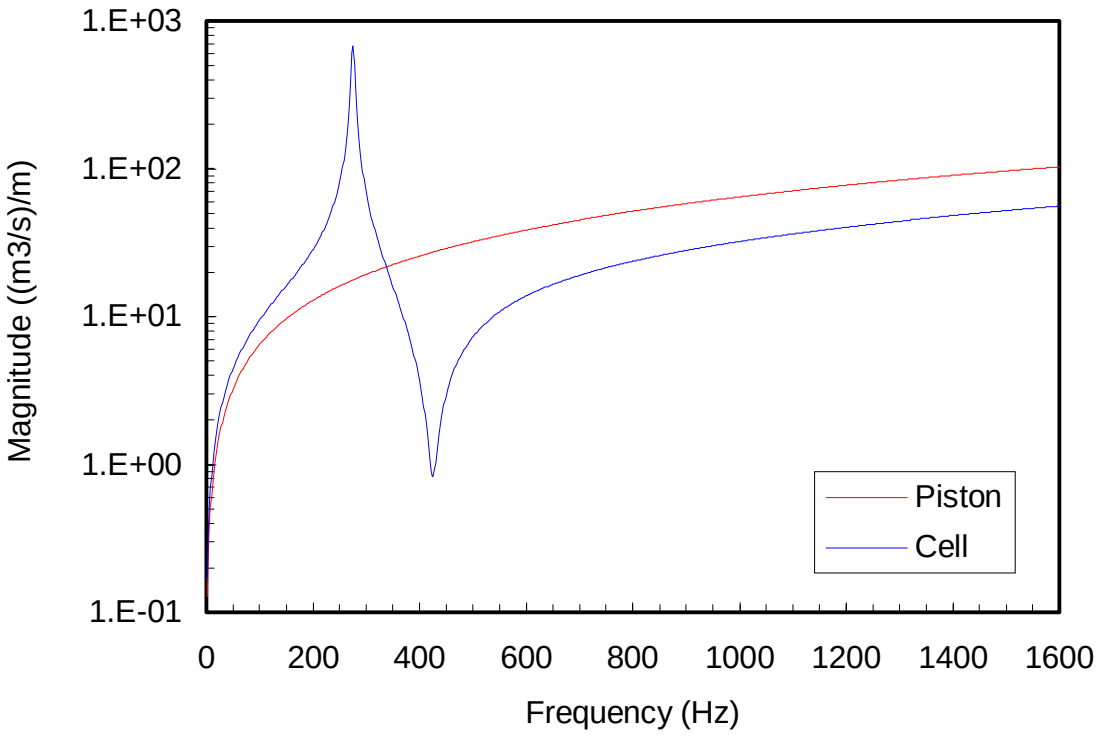

Figure 3.2 Source strength of piston and baseline cell for mechanically coupled implementation

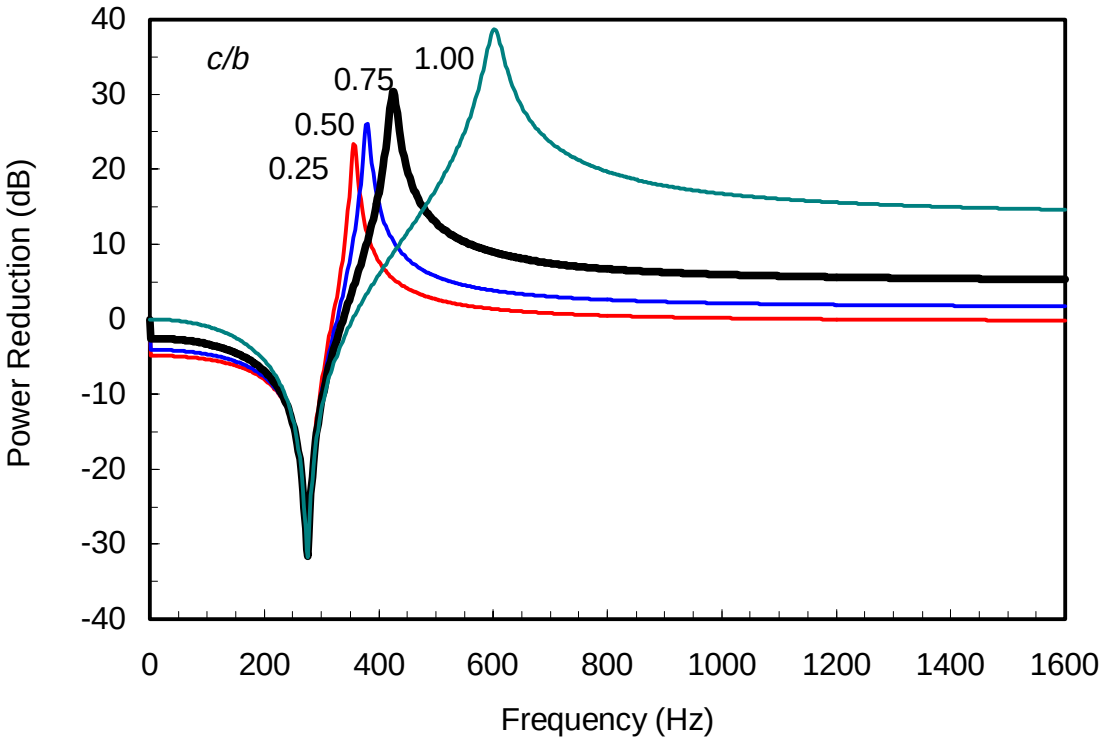

Figure 3.3 Parametric study on area ratio by varying the radii ratio, *c*/*b*

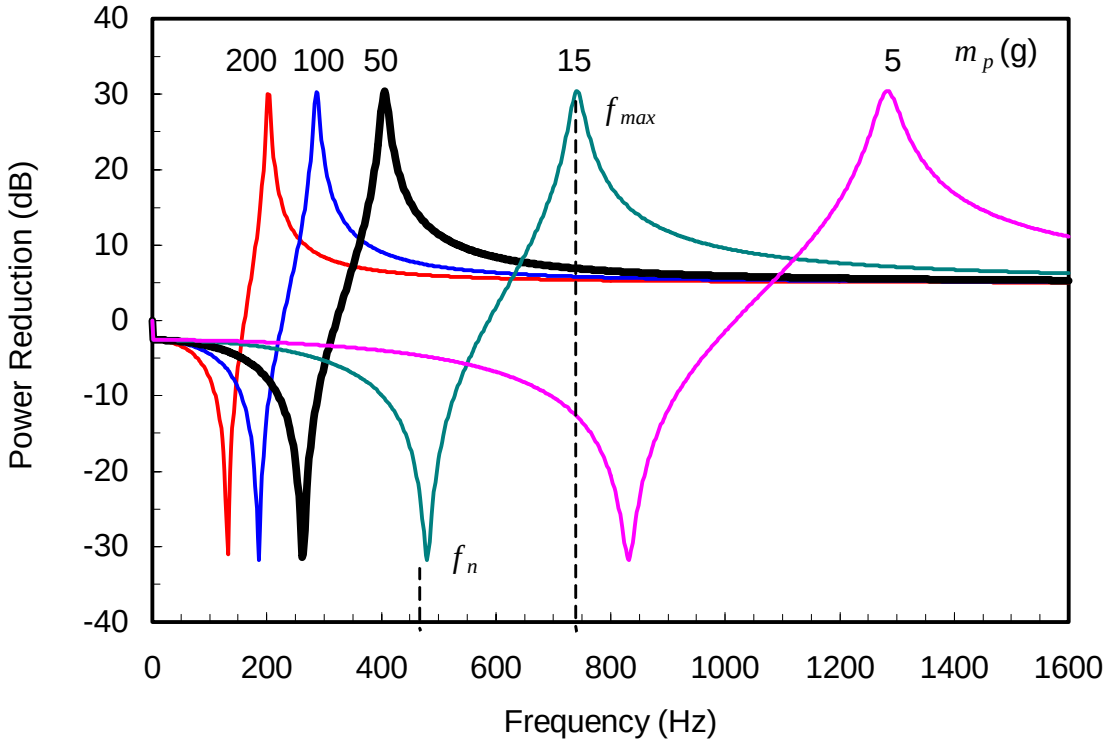

Figure 3.4 Parametric study on system resonance by varying the system mass, m_p

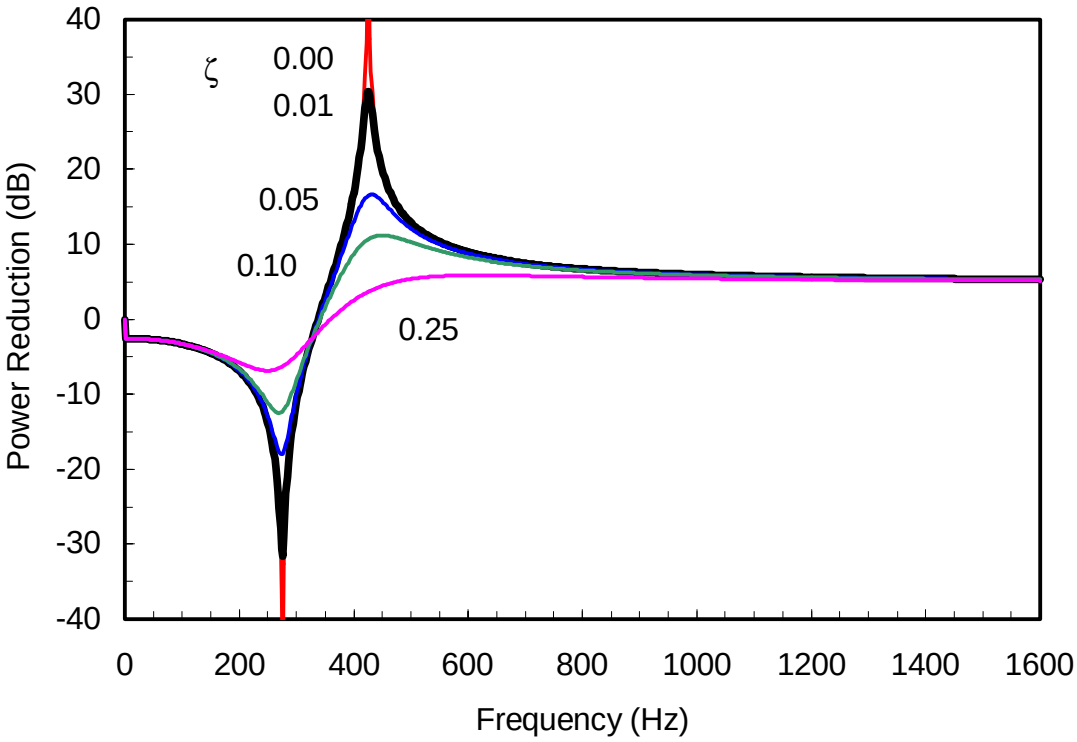

Figure 3.5 Parametric study on shim damping by varying the damping ratio, ζ

3.3 Mechanically and Acoustically Coupled Cell

3.3.1 Physical Implementation

The implementation of the mechanically and acoustically coupled weak radiating cell uses an elastic element in conjunction with a rigid plate containing an orifice to create the dipole affect. Recall Figure 2.7a for an illustration of the implementation. The elastic element is assumed to be closed cell foam with a low Modulus of Elasticity (E = 300 kPa) and a low density (ρ = 36 kg/m^3) with a height of L and an inner and outer radius of b and a, respectively. The dimensions for the baseline cell are tabulated in Table 3.2. Another possibility for the elastic medium would be to use a rubber bevel boot that allows for compliance in the axial or normal direction with respect to the cell surfaces.

The annular rigid plate with a thickness of l_p and an inner and outer radius of c and a, respectively, forms one of the radiating surfaces. Though a number of materials can be used, the plate is assumed here to be made of aluminum (Modulus of Elasticity E = 71GPa, Poisson's ratio σ = 0.33, and density ρ = 2700 kg/m^3) to place the fundamental bending resonance outside the 1000 Hz frequency range of interest while also considering the contribution to the total cell mass. From the plate properties, the fundamental resonance is 2571 Hz [24]. By attaching the rigid plate to the elastic element, a sealed cavity with radius b is formed. Then through the relative motion between the plate and piston, Helmholtz resonator dynamics are induced at the orifice, which forms the second radiating surface.

With the given realistic parameter dimensions, the overall height and mass of the cell is 28 mm and 190 g, respectively. As determined with the mechanically coupled cell, this implementation of the weak radiating cell is again determined to be a compact and lightweight noise control device by either active or passive control approach standards.

Table 3.2 System parameters for mechanically and acoustically coupled baseline cell

Description	**Variable**	**Value**
Piston radius	a	57.2 mm
Cavity radius	b	12.7 mm
Orifice radius	c	6.4 mm
Plate thickness	l_p	3.2 mm
Cavity height	L	25.4 mm
Elastic medium damping ratio	ζ	0.01

3.3.2 Modeling Techniques

In the theoretical section for the mechanically and acoustically coupled cell of Chapter 2, several variables were introduced but no modeling techniques were divulged. Though various approaches may be taken to model these variables, the chosen techniques used for the mechanical and acoustic stiffness, the mechanical and acoustic damping, and the effective fluid mass in the orifice will be given in this section. Also, the response of the elastic element will be modeled as a continuous system and compared to the simplified single degree-of-freedom model to validate the sdof assumption.

Assuming the elastic medium behaves as depicted in the simplified single degree-of-freedom model in Figure 2.7b, the mechanical axial stiffness of the elastic element, k_m, can be computed as

$$k_m = \frac{SE}{L} \tag{3.5}$$

where S is the surface area of the elastic element, E is the Modulus of Elasticity, and L is the height of the element. On the other hand, the stiffness of the fluid in the orifice, k_f, is modeled using a mechanical analogy and is given by Eq. (3.3). This equation is the traditional equivalent stiffness of a rigid walled Helmholtz resonator [21].

The mechanical damping of the elastic element, c_m, is modeled as viscous damping and is given by Eq. (3.4). To model the more complex acoustic damping of the orifice, the impedance at the cell orifice opening is investigated. For low frequencies, the mechanical radiation impedance at the orifice is [25]

$$Z_m = \left(i\omega m_f + R_f\right) \cdot S_{c1}^2 \tag{3.6}$$

where

$$R_f = \frac{K_d \rho c_a k^2}{4\pi} \tag{3.7}$$

is the radiation resistance, K_d is the damping constant with $K_d = 1$ for thin-walled duct opening and $K_d = 2$ for a flanged opening, and k is the acoustic wavenumber. With impedance equal to force, pS_{c1}, divided by velocity, v_{c1}, a force balance at the orifice reveals the acoustic damping term to be

$$c_f = R_f S_{c1}^2 = \frac{K_d \rho c_a k^2}{4\pi} S_{c1}^2 \tag{3.8}$$

Next, the technique to model the mass of the fluid in the orifice of the resonator is developed. Due to end corrections at the inner and outer openings of the resonator, an effective orifice length exists that consequently affects the mass of the fluid in the orifice. The model assumes a short circular orifice with flanges at both openings and incompressible uniform fluid flow within the cavity. From the acoustic inertance at low frequencies, the mass of the fluid inside the orifice is given as [25]

$$m_f = \left(\frac{\rho l_p}{\pi c^2} + 2\frac{8\rho}{3\pi^2 c} \right) \cdot S_{c1}^2 \qquad k_w l_p << 1,\ l_p \cong c \tag{3.9}$$

recalling that c is the radius of the orifice. The first term in Eq. (3.9) is the physical mass of the fluid in the orifice while the second term is due to the orifice end corrections. Since both ends of the opening are flanged for a thin flat plate, the end correction is simply doubled to obtain the combined correction, thus the factor of 2 in Eq. (3.9).

Finally, verification will be performed on the assumption that the elastic medium behaves as a single degree-of-freedom system in the frequency range of concern. This will be achieved by developing a continuous model for the elastic medium and comparing the response to the single dof model response for frequencies below 1600 Hz. The details of the continuous model derivation are contained in Appendix C. Using the parameters given in Table 3.2, the uncoupled displacement response of the annulus elastic element is given in Figure 3.6 using the single degree-of-freedom model and the continuous model. The models are nearly identical up to approximately 500 Hz, where the presence of the second mode becomes apparent. Since the frequency range of concern is below 1000 Hz, the single dof model is determined to sufficiently represent the system at low frequencies.

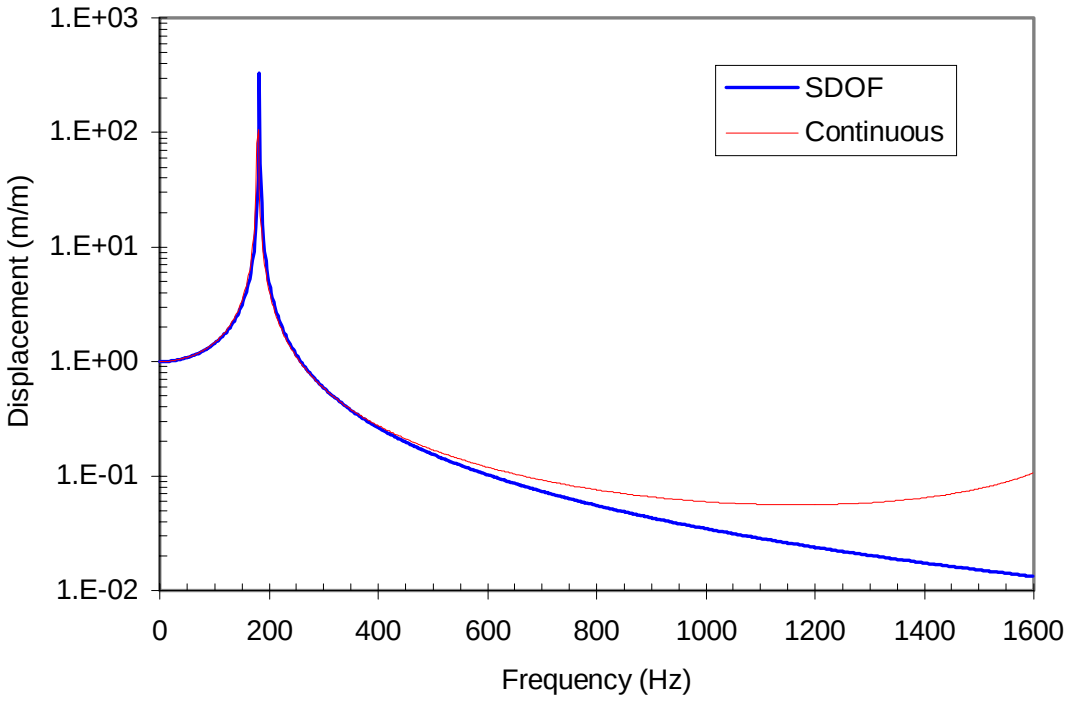

Figure 3.6 Comparison of displacement response of annular elastic element from single dof and continuous models

3.3.3 Parametric Study

The parameter values given in Table 3.2 will be used for each parametric case study on the mechanically and acoustically coupled cell implementation of the weak radiating cell concept, with the exception of the parameter(s) affected by that specific case study. The source strength of the baseline cell and piston is plotted in Figure 3.7.

Due to the heavily coupled dynamics of this weak radiating cell implementation, performing an effective parametric study involves rigorous assumptions to clearly isolate the effects of various important parameters. Complimenting this, a parametric study on the ratio of radiating surfaces offers little useful information applicable to the design of the maximum reduction region where a perfect dipole is created. However, the area ratio greatly effects the acoustic resonance of the system.

The next parameter to be investigated is the system resonant frequency due to the mechanical properties of the plate and elastic medium. This can be altered by changing either the thickness or density of the plate to affect the mass and/or by changing the elastic medium surface area, height or Modulus of Elasticity to modify the stiffness. In this study, the elastic medium Modulus of Elasticity varied while the surface area and height were held constant. The resulting sound power reductions are shown in Figure 3.8. As desired, the effects of altering the mechanical resonance were decoupled from the dynamics of the acoustic system. The frequency of maximum reduction occurs at higher frequencies as the stiffness is increased, as expected. However, the maximum level of power reduction decreases as the stiffness increases. Another interesting factor is the ratio of the frequency of maximum reduction to the natural frequency. This ratio decreases with the natural frequency of the system. Similar effects were revealed for the mechanically coupled cell. In attempts to reduce the overall weight of the control device, the plate mass should be minimized which implies a minimization of the stiffness to yield a predetermined resonance frequency. The lowest stiffness is bound by the restraint placed on the elastic medium stating it must not allow non-planer motion, which may be induced with a very low stiffness.

The effects of the acoustic resonance on the system performance will be investigated next. This was achieved by varying the orifice radius, while assuming the plate density is changed as to not effect the plate mass, which in turn would change the mechanical resonance. The sound power level reductions are given in Figure 3.9. As desired, the effects are decoupled from the mechanical resonance. The ratio of the frequency of maximum reduction to the acoustic resonance frequency decreases with the resonance frequency, similar to the mechanical resonance effects. However, the maximum level of reduction is inversely related, with the maximum level increasing as the acoustic resonance is increased. An important factor here is to note the significant increase in system performance when placing the resonance out of the frequency range of interest. To this point, the acoustic resonance has remained within the range of concern to simply verify its effects on the system.

One approach to alleviate the increase in the radiated power at frequencies near the resonances is by introducing damping into the mechanical and acoustic systems. Thus, the effect of the elastic medium damping ratio on the system response is examined first and shown in Figure 3.10. As expected, increasing the energy dissipation of the elastic medium leads to a reduction at the mechanical resonance. However, it also decreases the maximum sound reduction because it affects the relative phase between the motion of the two surfaces, i.e. the two surfaces are not out of phase as the damping increases. Consequently, there is a sound reduction trade off to introducing damping into the mechanical system.

As detailed in the previous section, the acoustic system also possesses damping characteristics. The damping constant, K_d, for the orifice mechanical radiation impedance is a function of whether the opening is a thin-walled duct, $K_d = 1$, or flanged, $K_d = 2$. The effects of adding damping to the acoustic system are investigated in Figure 3.11. Note that damping constant values other than 1 and 2 were used to characterize the effects of acoustic damping on the reduction of radiated power. Theoretically, the orifice damping model does not support these values, however, additional damping may be introduced by placing a screen over the orifice to increase the mechanical radiation

resistance. In contrast to the mechanical damping, the acoustic damping has little effect on the system performance away from the resonant frequency, except for extremely high damping constants. This proves to be very beneficial in analyzing the sound power level reduction. Also note that as the acoustic damping is increased, the cell behaves the same as the mechanically coupled cell.

To compare the two implementations of the weak radiating cell concept, the mechanically coupled implementation is an inherently simpler system to model and to achieve realistic sound reductions. On the other hand, the acoustically and mechanically coupled implementation has the potential to ultimately achieve a greater level of performance. However, this work has demonstrated the difficulty to physically apply this implementation and obtain successful results. This difficulty is spawned from the need for sufficient compliance of the elastic medium in the normal direction while having enough stiffness in the radial direction to minimize dynamics in this direction. Such an elestic medium was not utilized in the experimental verification performed in the work. Therefore the results presented in Chapter 4 will only address those corresponding to the mechanically coupled cell implementation.

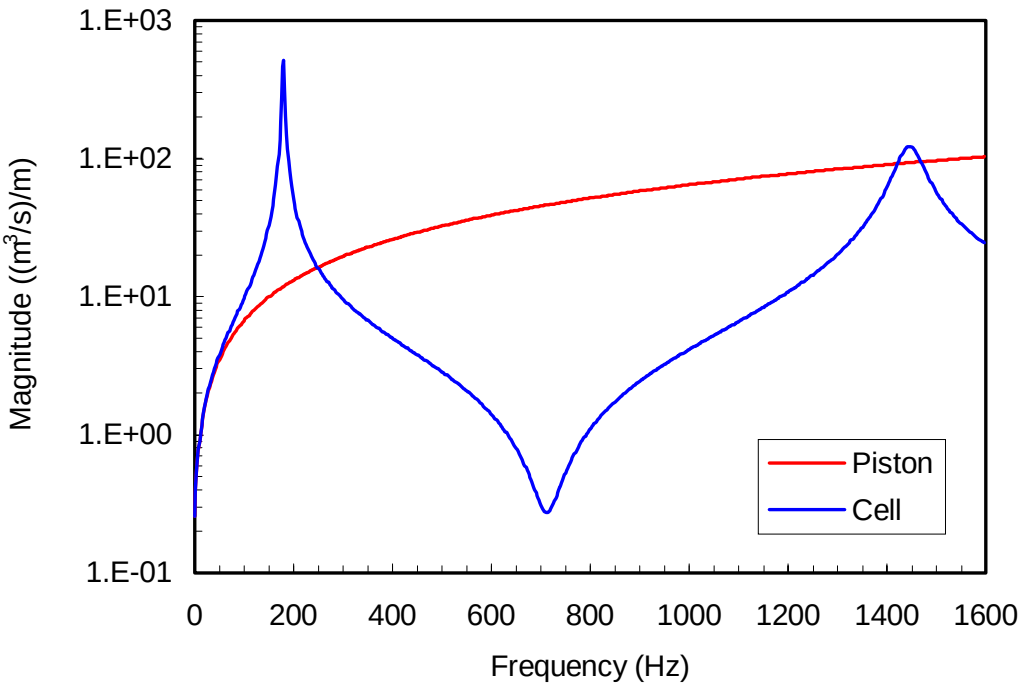

Figure 3.7 Source strength of piston and baseline cell for mechanically and acoustically coupled implementation

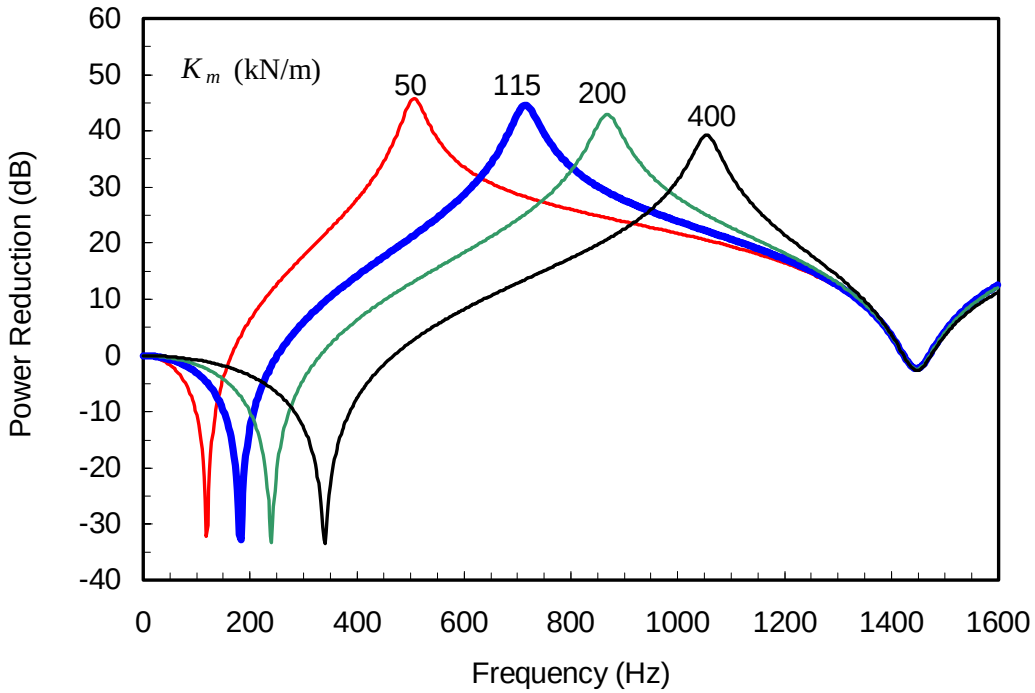

Figure 3.8 Parametric study on mechanical resonance by varying the stiffness of the elastic medium, k_m

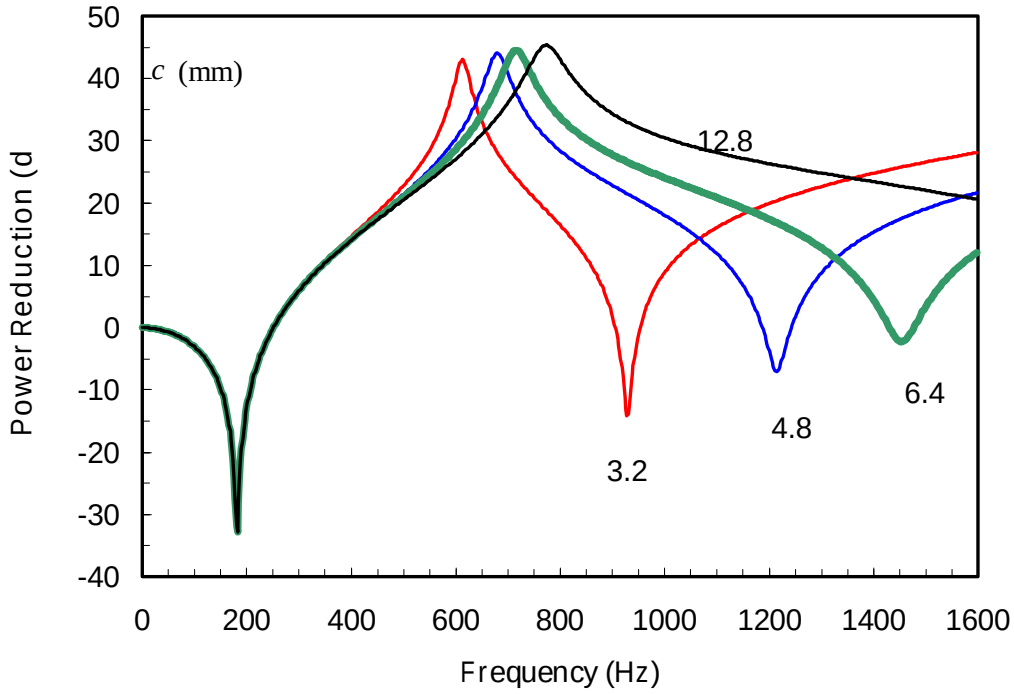

Figure 3.9 Parametric study on the acoustic resonance by varying the orifice radius, *c*

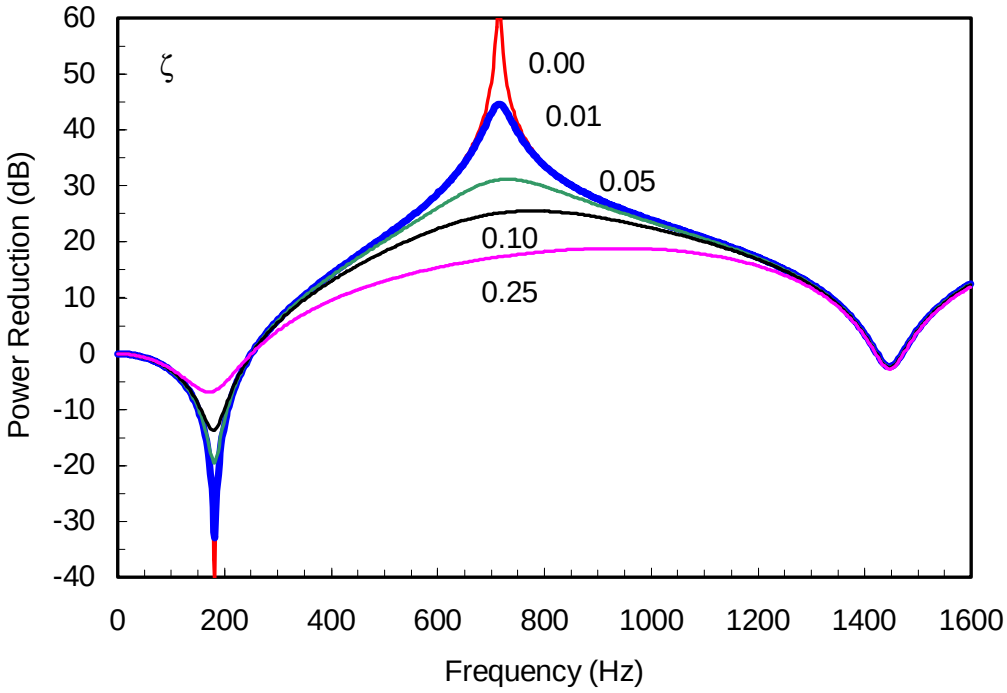

Figure 3.10 Parametric study on mechanical damping by varying the damping ratio of the elastic medium, ζ

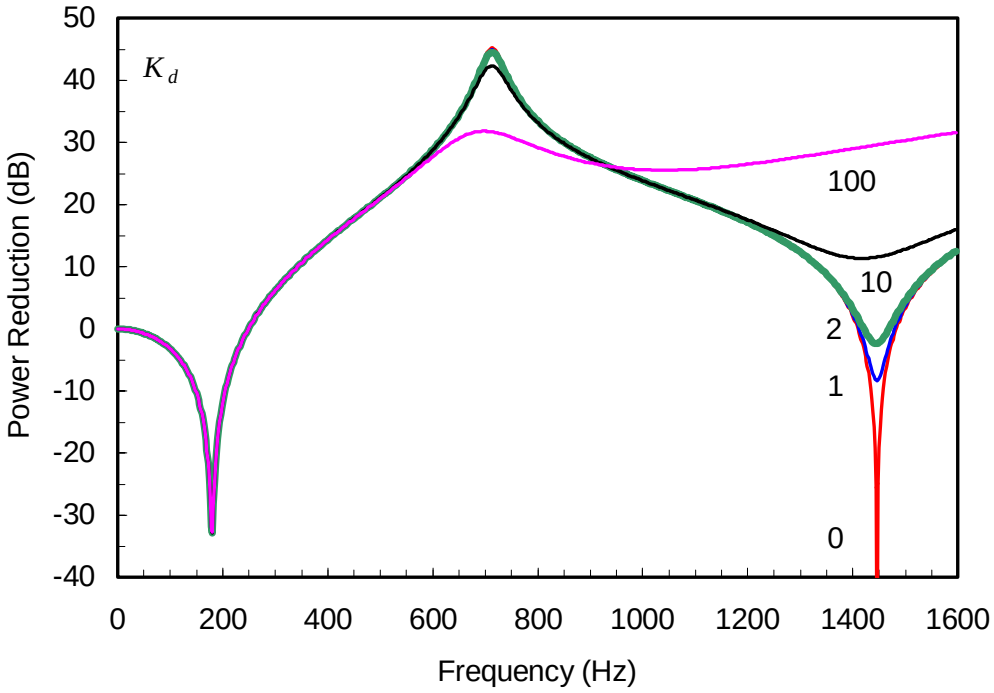

Figure 3.11 Parametric study on orifice damping by varying the acoustic damping constant, K_d

Chapter 4

Experiments

4.1 Introduction

The analytical results in Chapter 3 indicated the theoretical potential for the weak radiating cell concept to reduce low frequency structurally radiated noise. In this chapter, the theoretical concept will be experimentally verified. In a first attempt to achieve this, the results of tests performed on a single weak radiating cell using the mechanically coupled implementation applied to a simple piston-like structure will be examined. Analysis of the results will evaluate its ability to create a dipole, its performance, and its consistency to theoretical predictions. Though not a crucial addition to the work presented in the thesis, active control will be integrated into the system to investigate the potential of a hybrid cell. Then the results of experiments where an array of mechanically coupled cells was applied to a more complex structure will be analyzed. This is to verify the notion that the array of cells would attenuate the total radiated sound from the structure, i.e. its effectiveness in creating an array of distributed dipoles. Experiments were also performed on a single acoustically and mechanically coupled cell using acoustic foam as the elastic medium. However, the elastic medium did not possess the required stiffness in the direction normal to the cell surface while allowing for sufficient compliance in the direction parallel to the motion of the cell surface. This does not invalidate the concept of the acoustically and mechanically coupled implementation, but does however imply that further investigation into more appropriate materials for the elastic medium is required to prove that it is a realistic implementation for the weak radiating cell concept.

4.2 Single Cell on a Piston-Like Structure

The experimental verification of a single mechanically coupled weak radiating cell serves the purpose of investigating the response and performance of the weak radiating cell concept in a simple setup, i.e. applied to a simple piston-like structure. This will filter the input of complexities into the system so that the dynamics of the cell can be clearly defined.

4.2.1 Experimental Setup

To achieve a simple setup for the testing of a single weak radiating cell, a cell is applied to a rigid circular plate that emulates a piston-like structure. The structure is assumed to possess no dynamics beyond the uni-directional motion imposed upon it by an excitation input, i.e. radiate as a uniform piston. The radiating piston will be used as a baseline case for the performance of the weak radiating cell. Figure 4.1 is a photograph of the cell applied to the piston, which is driven by an excitation shaker with white noise from 0-1600 Hz. To assess the dynamics and performance of the cell, this system was tested in two environments.

In the first, a laser vibrometer was mounted to an automated traversing system and utilized to scan the surface of the untreated piston and cell, which facilitated modal and source strength analysis. A photograph of the cell and the laser traversing system is pictured in Figure 4.2. A twenty-one point scan across the surface of the piston and cell was performed along the diameters, with a scan point at the center and ten points on either side.

The second test environment included a baffled weak radiating cell and a microphone in an anechoic chamber to acquire sound pressure data. This setup is pictured in Figure 4.3. The microphone was positioned 75 cm above the center of the cell. Also, the shaker and piston assembly had the versatility to be raised and lowered so both the cell and piston surfaces were flush to the baffle during their respective test cases. The pressure data results were converted to acoustic power for the piston and cell cases

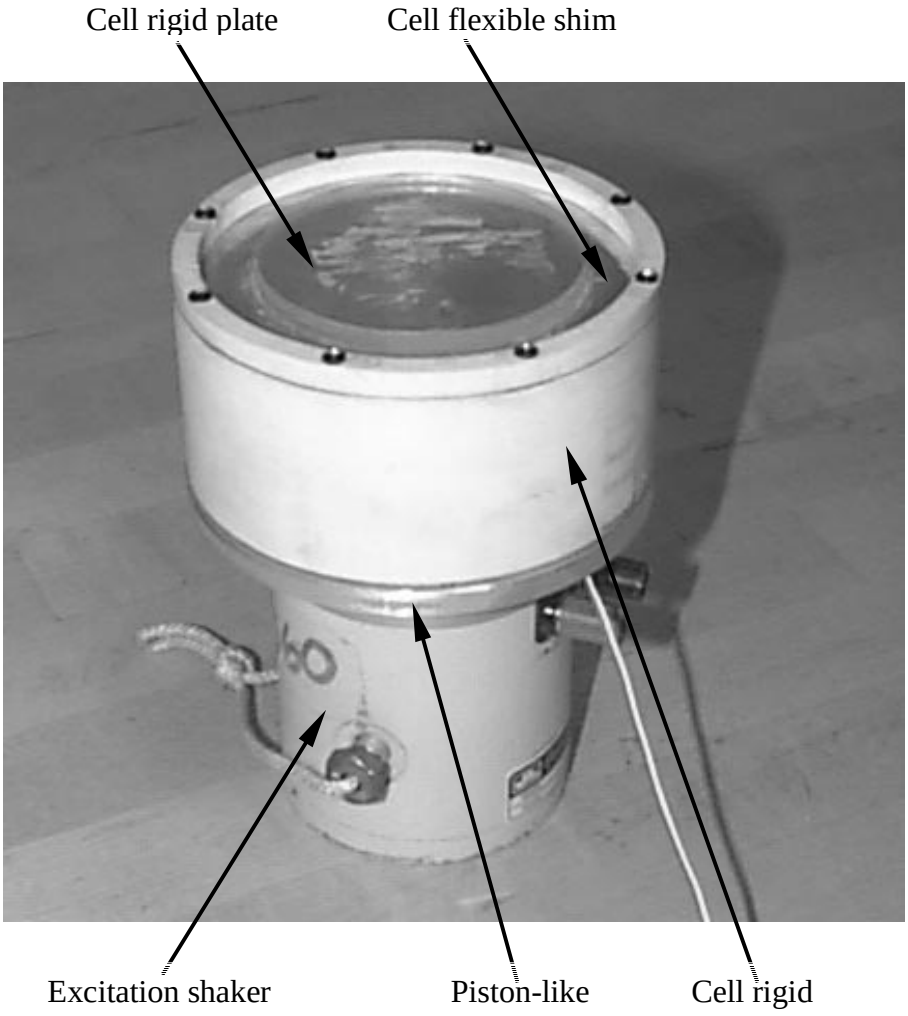

Figure 4.1 Experimentally tested mechanically coupled weak radiating cell

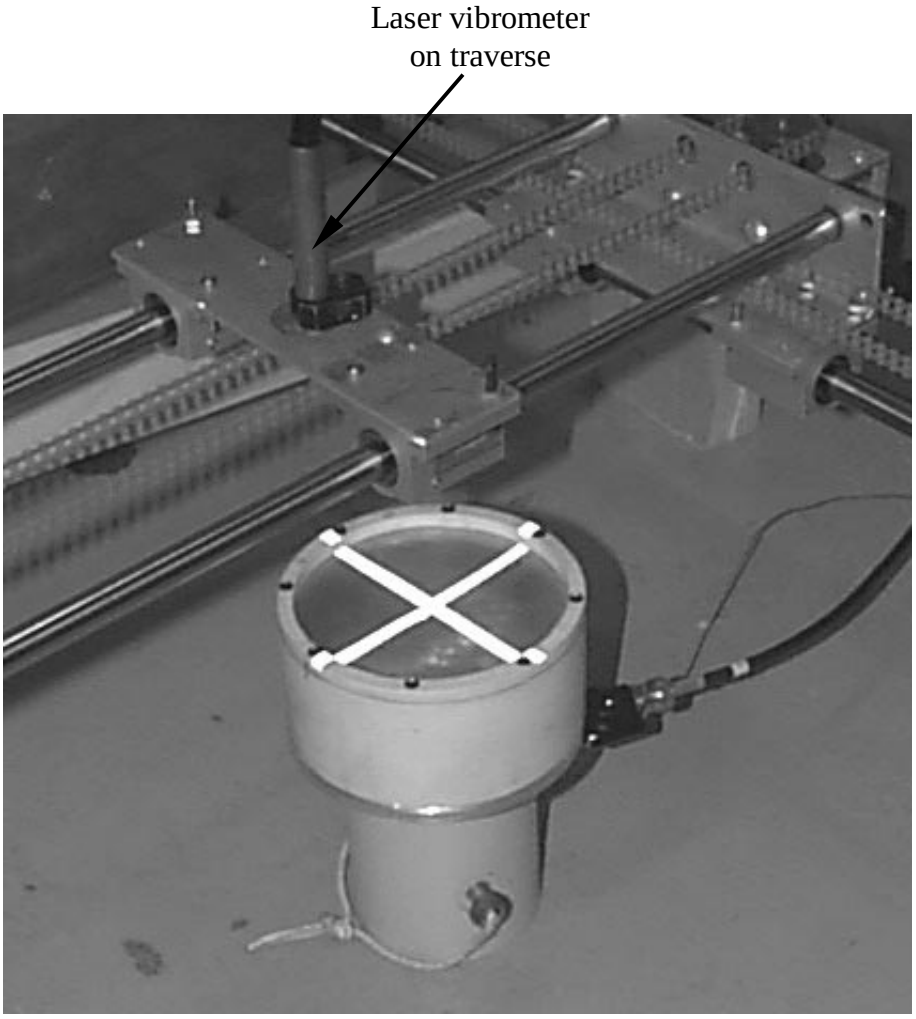

Figure 4.2 Experimental setup using laser vibrometer

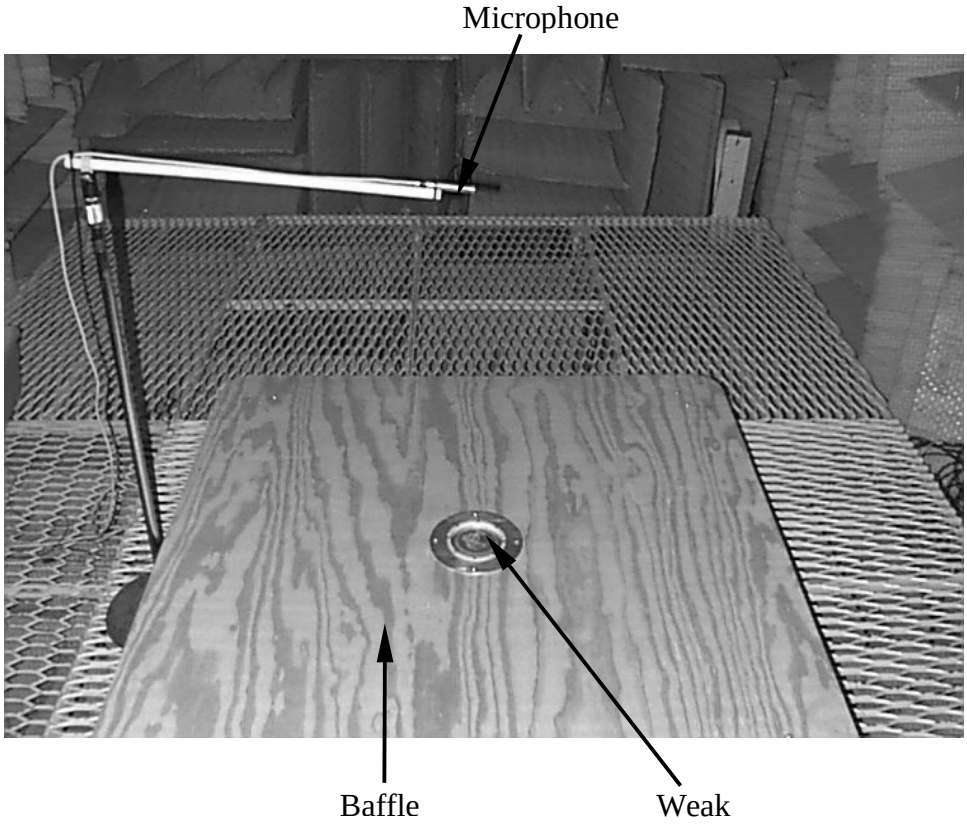

Figure 4.3 Experimental setup for pressure tests in anechoic chamber

and used to determine to sound power level reduction achieved by applying the cell to the offensive piston structure.

A schematic of the experimental setups is given in Figure 4.4. The schematic allows for either sensor, the laser vibrometer or the microphone, to be used for the respective setup. In both setups, a reference accelerometer was positioned on the bottom side of the piston so the output could be normalized to the input.

4.2.2 Weak Radiating Cell Design

The cell used for experimental verification of a single cell possessed the dimensions and physical properties of the baseline cell analyzed in Chapter 3. The dimensions of the system parameters are contained in Table 3.1. The use of identical system parameter values allows for direct comparison to theoretical predictions.

However in contrast to the physical implementation given in Chapter 3, polyvinyl chloride (PVC) tubing, (Modulus of Elasticity E = 800 MPa, density ρ = 1577 kg/m^3) served as the material for the rigid element of the cell. Though the recommended material for the rigid element in Chapter 3, structural foam, is commercially available, it was not practical to use the material to fabricate a single prototype for the sole purpose of concept verification. However, in realistic applications it would be prudent to facilitate the technology as to minimize the overall weight of cell surface treatment. It is important to remark that the fundamental resonance of the PVC element, computed from a wave analysis, is 2231 Hz. This is well above the frequency range of interest, so the element can therefore be assumed rigid in this range.

The rigid PVC element, the center plate that is made of Plexiglas, and the flexible bass shim are shown in Figure 4.1. The center mass was epoxied to a brass shim that in turn was clamped to the rigid element using a thin ring of PVC and machine screws. To ensure a tightly sealed cavity, the cell was then screwed to the rigid circular aluminum plate that served as the piston-like structure.

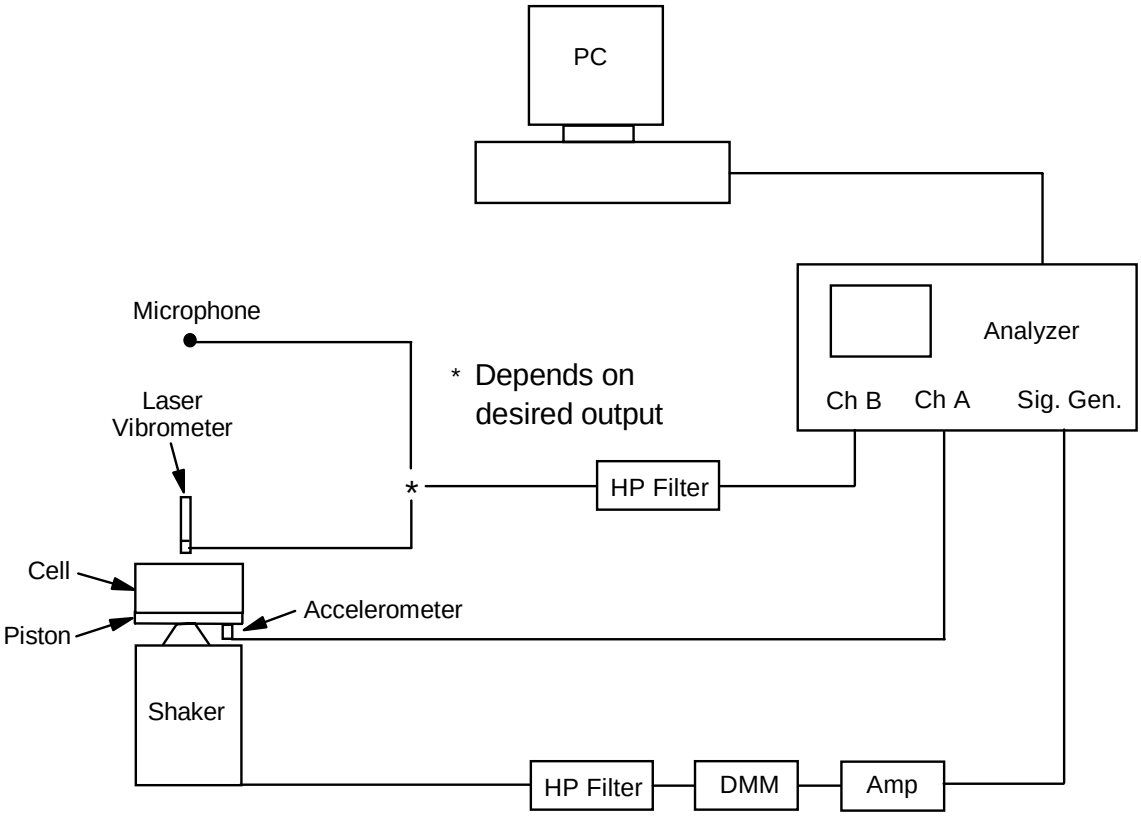

Figure 4.4 Schematic of experimental setup

4.2.3 Experimental Results

Through analysis of the velocity data obtained from the laser scan of the cell surface, the mode shapes and resonant frequencies can be identified. The velocity response at the center of the cell is shown in Figure 4.5. In the frequency range contained in this figure, there are two modes present. The resonant frequency of the dominant first mode occurs at 264 Hz, while the second and less evident mode has a resonance at 422 Hz. By plotting the real components of the velocity transfer function for the scan points across the diameter of the cell, the mode shapes at these resonant frequencies can be identified. As shown in Figure 4.6a, it is determined from the surface velocity response at 264 Hz that the first mode of the cell is the uniform vertical motion of the center plate. Notice the higher amplitudes on the right half of the cell, which suggests a rocking motion component is also present. The unmodeled rocking motion may be due to imprecision in the construction of the cell, i.e. the mass was not placed precisely in the center of the shim. The second mode occurs at 422 Hz and, as shown in Figure 4.6b, is a rocking mode. However, the presence of the rocking mode does not significantly effect the acoustics of the system since it is by definition a non-volumetric or dipole mode. In addition, the amplitude of the rocking mode resonance is nearly 20 dB below that of the fundamental resonance.

The laser velocity data also allowed for computation of source strength for the piston with and without a weak radiating cell applied. Using the data obtained from the laser scans across the radii, the complex source strength of the plate and cell can be computed using the following approximate equation

$$Q \cong \sum_{i}^{11} v(\omega)_i \cdot S_i \qquad (4.1)$$

where i is the index for the number of scanning points across one radius, v is the complex velocity as a function of frequency at the locations of the laser scan, and S_i is the corresponding annular area associated to the velocity. Figure 4.7 shows the source strength for the piston and weak radiating cell and reveals that a significant decrease in source strength is realized throughout a wide frequency range. As expected, there is an

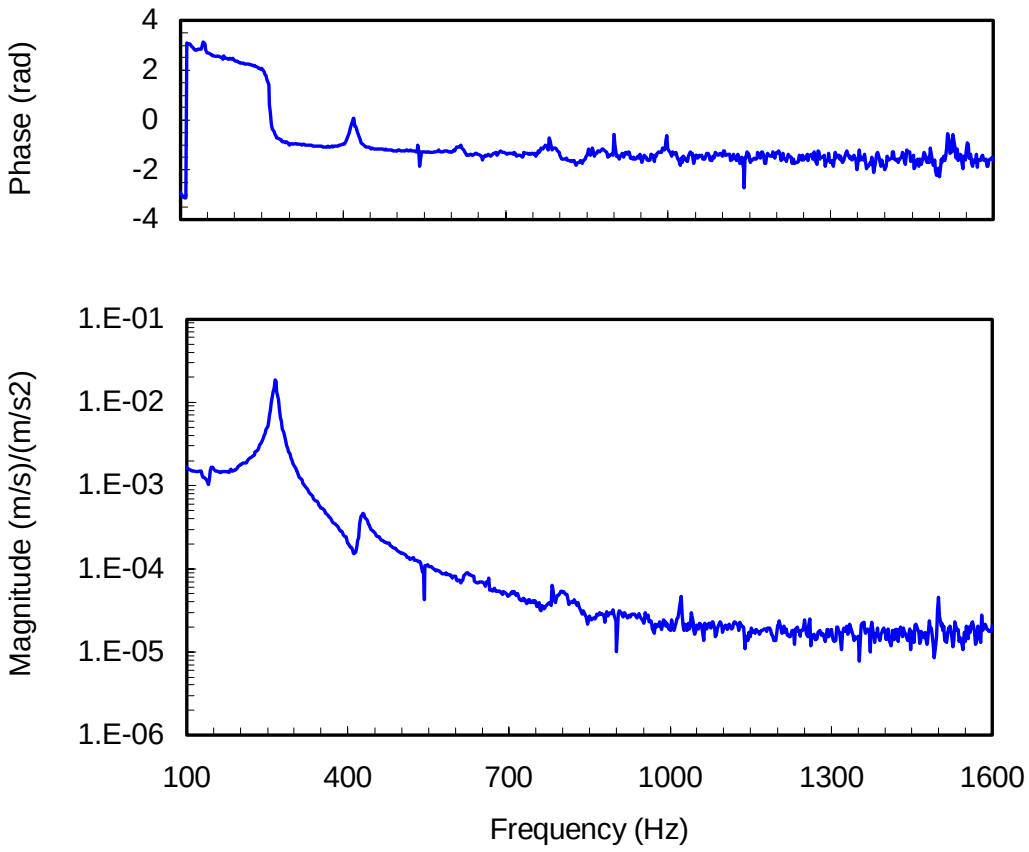

Figure 4.5 Complex surface velocity response at center of cell

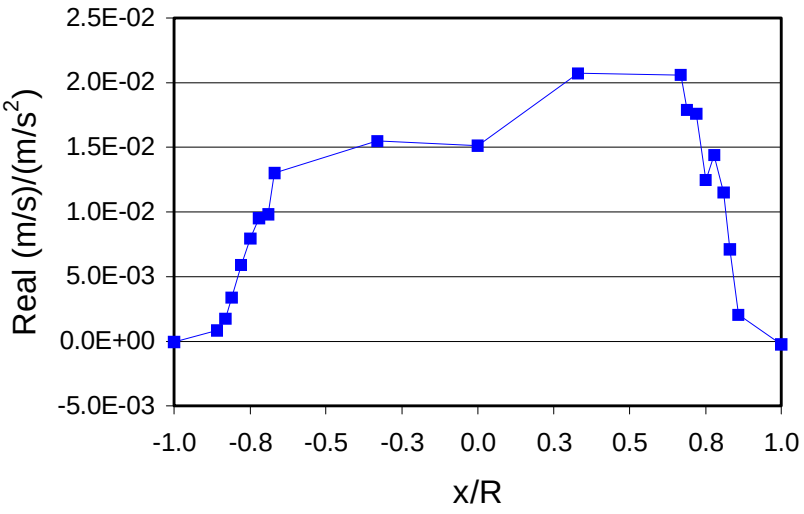

(a)

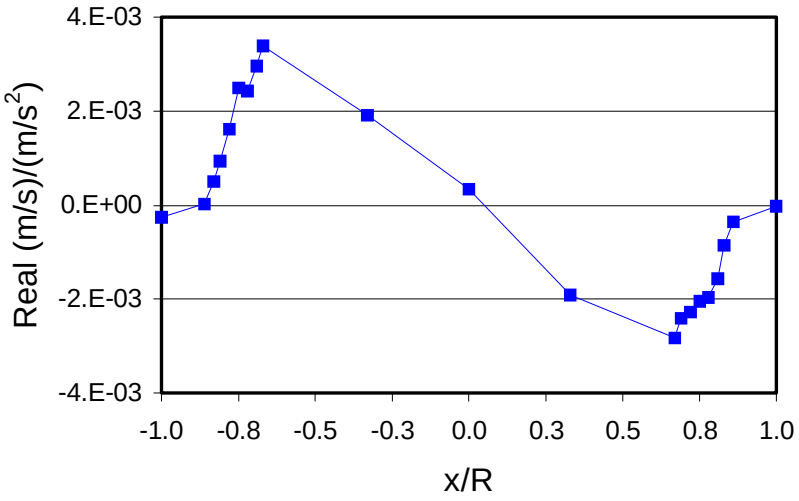

(b)

Figure 4.6 Profile of velocity response across cell radius (a) 264 Hz, (b) 422 Hz

increase in the radiated sound around resonance and a significant decrease in radiated sound where a perfect dipole source is created, which is at 474 Hz.

The sound pressure levels for the untreated piston and for the piston with a weak radiating cell applied are given in Figure 4.8. Similar to the source strength results presented in Figure 4.7, the dipole effect of the cell produces a significant decrease in the sound pressure level above the resonance of the cell with a maximum reduction around 500 Hz.

Since the frequency range of concern, under 1000 Hz, can be considered to be low frequency, the piston and cell sources are assumed to radiate as baffled simple sources. Acoustic power can be computed from Eq. (2.13) using the source strength data and from the following equation from the pressure data [20]

$$W = \frac{2\alpha\pi R^2 |P|^2}{\rho c_a} \qquad \lambda >> a \tag{4.2}$$

where α = 1 for a free-field source and 2 for a baffled source, a is the radius of the piston, R is the distance to the microphone, and P is the pressure amplitude. The power reduction from both the source strength and pressure data is then defined as the difference between the power radiated from the piston and the power radiated from piston with the weak radiating cell applied. Figure 4.9 reveals the sound power level reduction achieved by applying the cell to the piston. It can be seen that similar reduction levels are realized by the two approaches. There is an increase in the radiated power below the resonance of the cell; however, significant reduction levels are achieved throughout the frequency range above resonance with maximum levels over 30 dB. As previously mentioned, this region of maximum reduction is where a nearly perfect dipole acoustic source is created.

A comparison between the experimental and analytical results for the single weak radiating cell is tabulated in Table 4.1. The experimental values in this table were obtained from the experimental pressure data. This is because pressure is considered a more accurate measurement than source strength, which is computed by multiplying discrete velocity data by estimated surface areas. Included in the table are the system

resonant frequency, f_n, the frequency of maximum reduction, f_{max}, and the overall sound power level reduction, Γ_{Lw}, between 100-1600 Hz and 400-1600 Hz. The 400-1600 Hz bandwidth is an important frequency range because in both the theoretical model and experimental verification, positive power reduction is produced throughout this range. The resonant frequencies and overall power reductions tend to match closely, however, the frequency at which maximum reduction is achieved varies more so. This discrepancy is most likely due to the assumed velocity profile function of the shim for the analytical model that significantly alters the area ratio of the two radiating surfaces. As revealed in the parametric study of Chapter 3, the frequency of maximum reduction is very sensitive to this ratio.

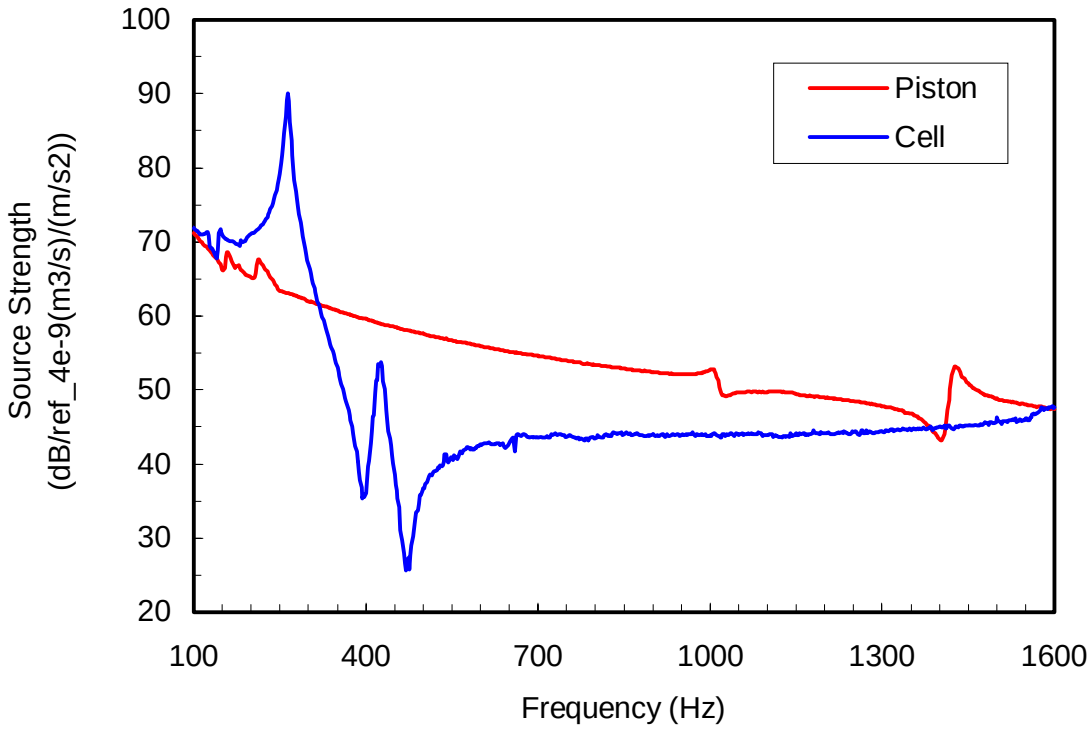

Figure 4.7 Source strength of piston and cell

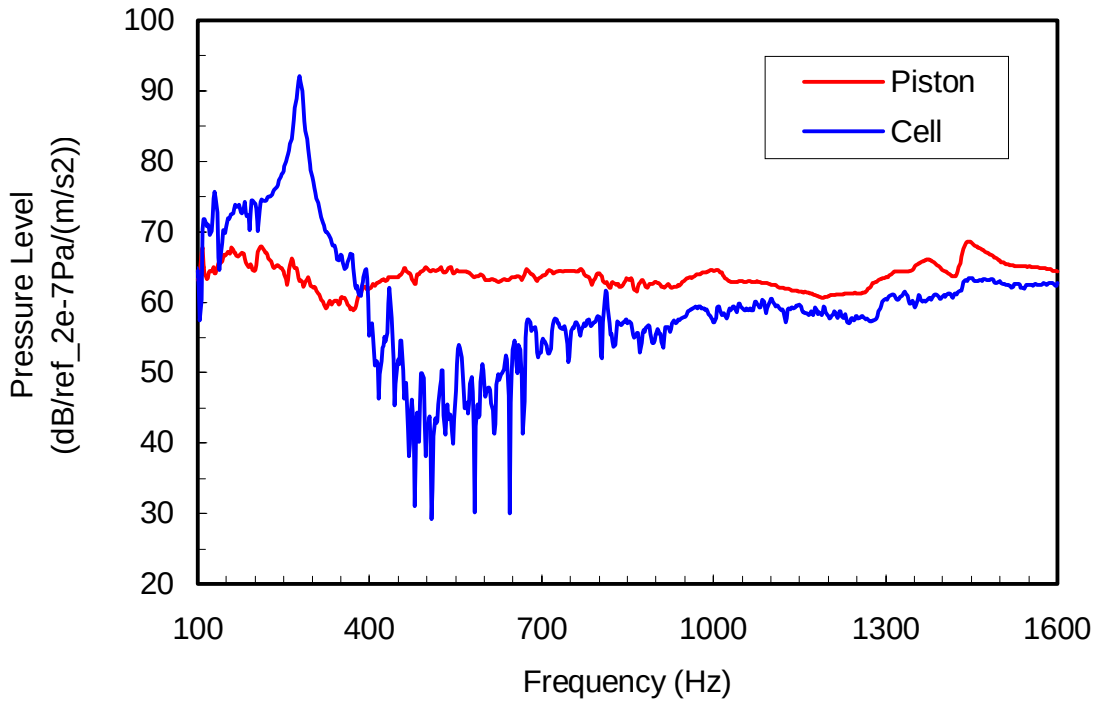

Figure 4.8 Sound pressure levels of piston and cell

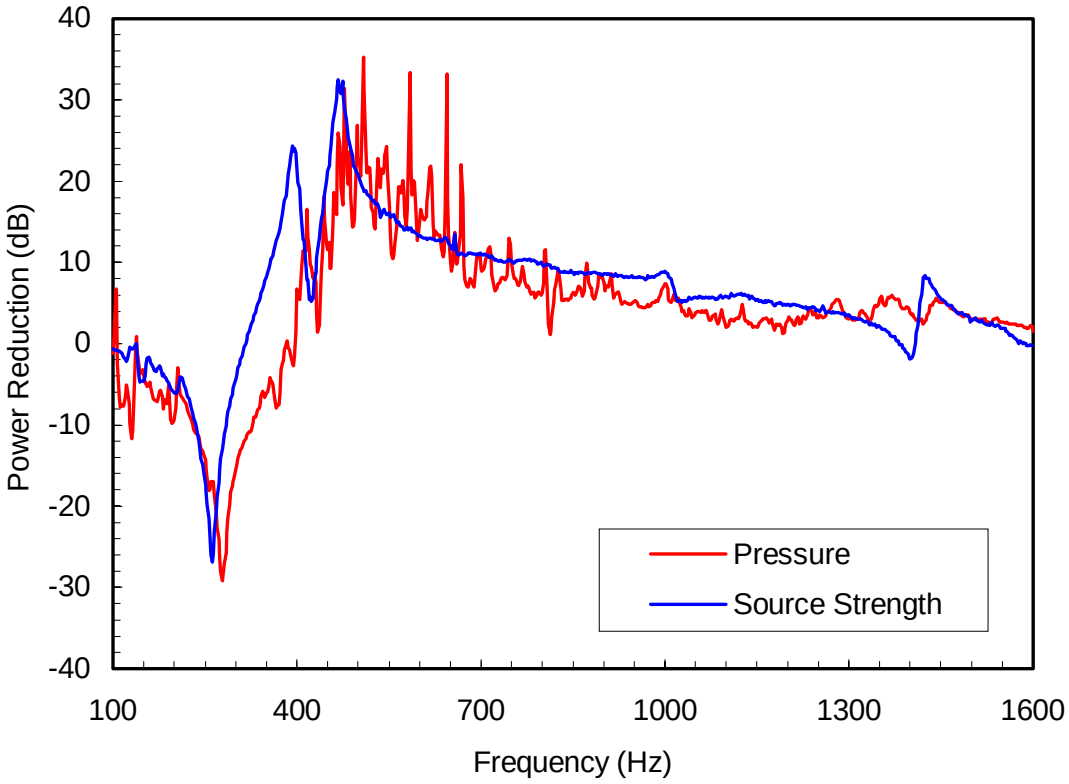

Figure 4.9 Sound power level reduction achieved by applying weak radiating cell to vibrating piston

Table 4.1 Comparison of system characteristics for single mechanically coupled cell

Characteristic	**Experimental**	**Analytical**
Natural Frequency f_n	278 Hz	276 Hz
Frequency of Maximum Attenuation f_{max}	508 Hz	426 Hz
Power Reduction Γ_{Lw} (100-1600 Hz)	-8.6 dB	-9.5 dB
Power Reduction Γ_{Lw} (400-1600 Hz)	5.2 dB	6.7 dB

4.2.4 Hybrid Cell

Though the scope of this thesis is to primarily present the analytical and experimental verification of the weak radiating cell as a purely passive noise control device for structurally radiated noise, a hybrid approach was also experimentally investigated. The goal was to combine the passive effects of the cell with active control to help alleviate the adverse effects induced at resonance. As shown in the analytical model and experimental results of the cell, the radiated sound is unfortunately increased at very low frequencies where the cell resonance is placed through the design of the system parameters. The design intent of the passive cell is to place the system resonance out of the frequency range of concern. However, if this is not feasible or if further reduction is desired in a realistic application, active control may be used to develop a hybrid cell. The advantage of a hybrid cell, as opposed to utilizing a purely active control approach, is that the passive effects of the cell limits the control bandwidth to a relatively narrow frequency range. Thus, it is not necessary to attenuate the entire frequency range of concern through active control. This reduces the requirements and limitation placed on the system control algorithm.

The control algorithm implemented in this study is a single-input, single-output (SISO) feedforward Filtered-X LMS control approach [10]. It is not the intent to present the theory of the algorithm, but merely to use it as a tool to perform active control. So, the system will be described on a relatively simplistic level. The major system components include a disturbance signal, a control signal, an error signal, and a signal to monitor the system performance. The control signal is obtained by filtering a reference signal, which is coherent to the disturbance signal, through an adaptive finite impulse response (FIR) filter. A monitor signal, which may or may not coincide with the system response signal, is used to evaluate the performance of the control system.

To give some physical insight into the experimental setup, a similar setup was used to that of the single cell experiments performed in the previous section, with the exception that there now exists a control source and path. Figure 4.10 pictures the control source, a small loud speaker, mounted to the surface of the piston structure. The

cell was then mounted to the piston, covering the speaker. Figure 4.11 reveals a schematic of the experimental setup. A significant component of the system is the computer that generated the disturbance and control signals. The disturbance signal to the shaker was white noise from 0-1600 Hz, high-pass filtered at 100 Hz. Both the error and control signals were band filtered below 100 Hz and above 400 Hz, the region in which active control is needed to attenuate the cell resonance. The asterisk in Figure 4.11 at the input to the mixer board signifies the option to use either a pair of accelerometers or a microphone as the error sensor. This option will be further discussed in the following paragraph.

For the experiments, two distinct approaches were taken to minimize the pressure radiated from the cell. One approach used a microphone 75 cm on axis above the cell as both the error sensor and the monitor sensor. Another approach used the difference between the acceleration at the center of the cell and of the piston as the error sensor signal. The minimized radiated pressure was again monitored with the microphone. For this error sensing approach, the volume velocity was obtained by summing the disturbance and system response, or acceleration, signals through the mixer board, each of which were gain weighted to account for their respective surface areas. The differing error sensing approaches are distinguished in Figure 4.11 by the use of separate channels on the mixer board. Either channel 2 or 3 was used depending on the type of sensing desired. For active control in realistic applications, it would more favorable to place the error sensor on the control device and therefore implying that the use of the accelerometers is preferred. However, since this technique does not directly minimize the radiated pressure, which is the true and final goal, less performance is typically obtained. This will be quantified and discussed in further detail after the results of the experiments are presented.

The results of the experiments will be presented in a very concise form, being the achieved sound power level reduction computed from the acquired pressure data. Only the frequency range around the cell resonance in which active control was performed will be analyzed for the three test cases: passive, hybrid with a microphone as the error

sensor, and hybrid with accelerometers as the error sensor. Figure 4.12 reveals the power level reduction gained for each test case. Though active control was initiated at 100 Hz, a noticeable increase in the performance is not revealed until approximately 250 Hz. This is most likely due to the control speaker lacking control authority at lower frequencies. Its small size was desirable to not only to meet the space requirements of the cell cavity but also to minimally effect the cavity volume that directly alters the cell resonance. Consequently, the speaker lacked the response to effectively control the system at frequencies below 250 Hz. However, the active control component of the cell did alleviate a significant portion of the increased radiated power at resonance and furthermore produced positive attenuation just above resonance. A less significant performance increase is seen from 350 to 400 Hz, whereas active control was terminated. Though the active control cases achieved positive attenuation in a narrow bandwidth, the overall sound power level reductions from 250 to 400 Hz remain negative. In this bandwidth, the purely passive cell reveals an overall reduction of -21.2 dB while the hybrid cell reveals overall levels of -9.4 dB and -11.9 dB for the microphone and accelerometer test cases, respectively. This demonstrates that a hybrid cell may be a feasible method of achieving additional attenuation beyond the purely passive cell, if so desired. In addition, the use of a microphone as the error sensor proves to be more effective in controlling the radiated pressure. However, the performance with accelerometers used to obtain the error signal yielded comparable results.

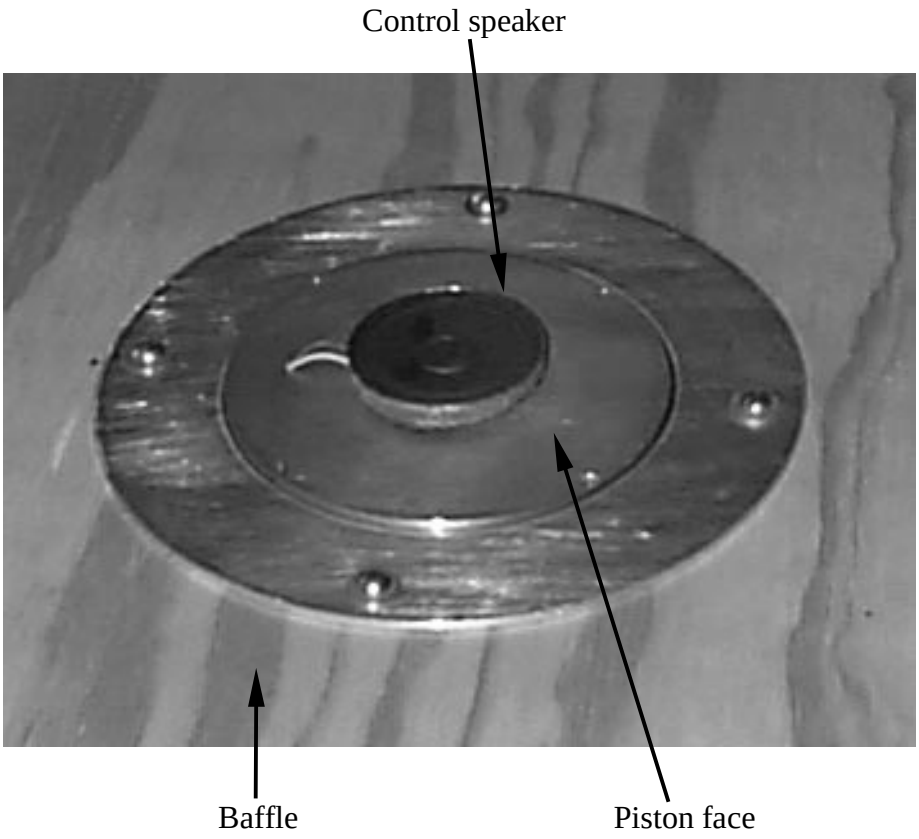

Figure 4.10 Control speaker mounted to baffled piston structure

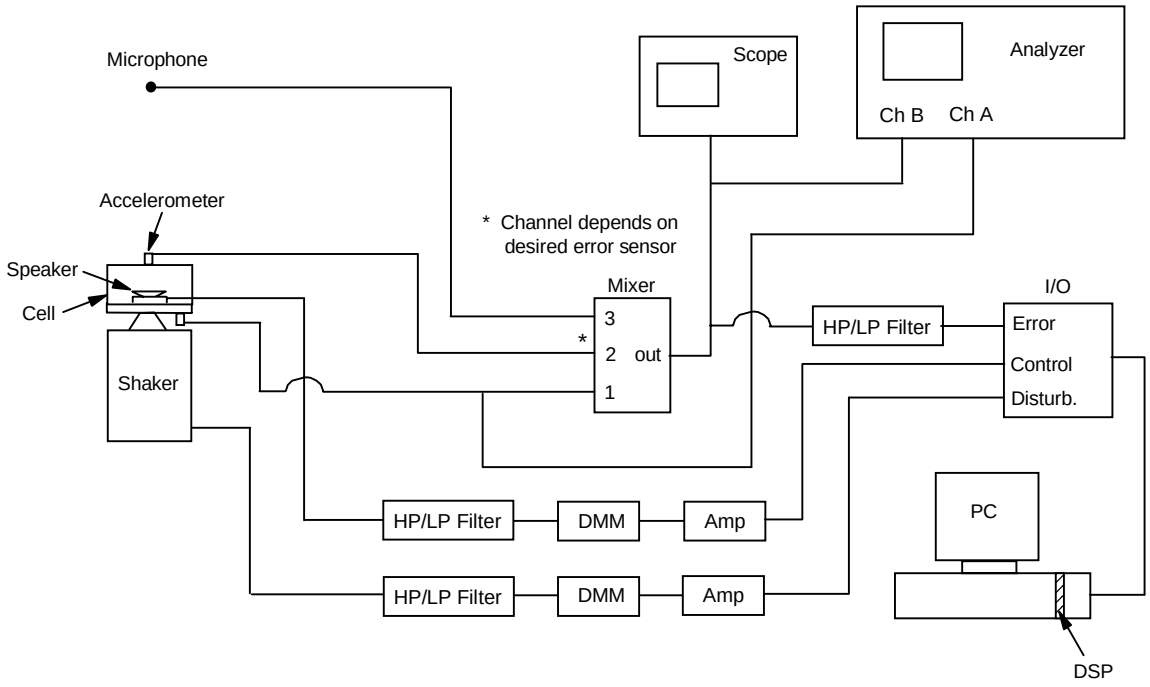

Figure 4.11 Schematic of experimental setup for tests on hybrid cell

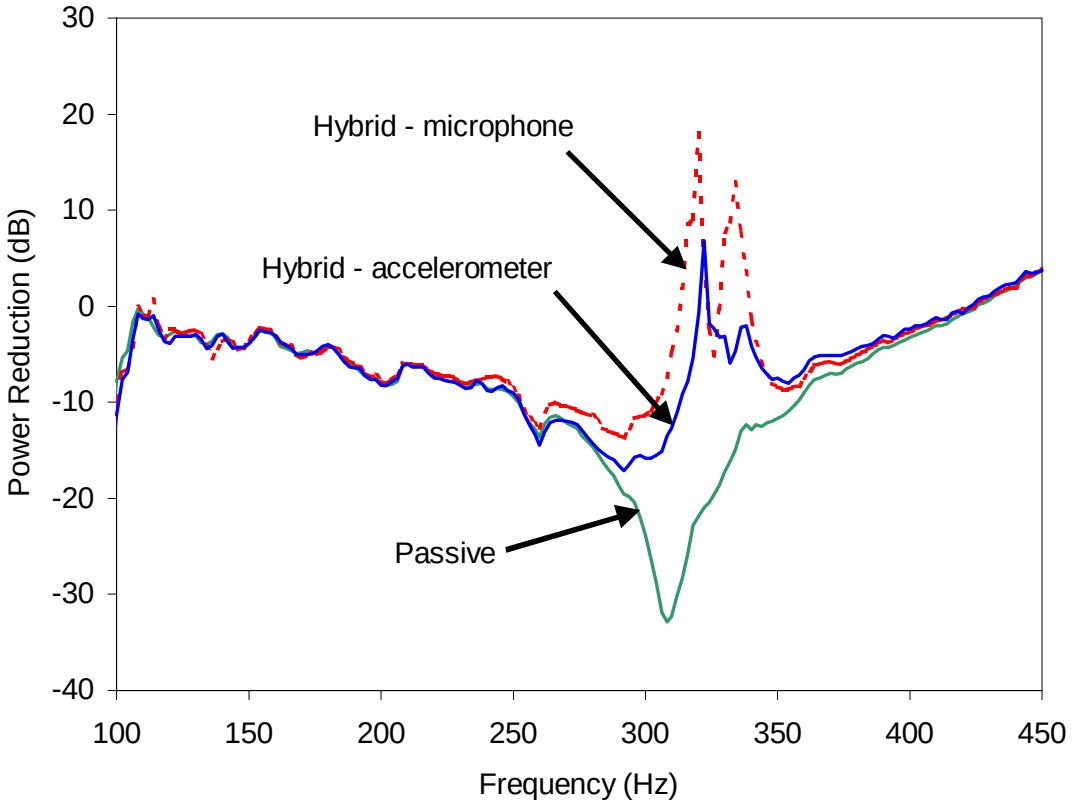

Figure 4.12 Sound power level reductions for passive and hybrid cell. Hybrid cell tests used multiple types of error sensors

4.3 Array of Cells on a Plate

In section 4.2, a single mechanically coupled weak radiating cell was applied to a simple piston-like structure. The main objective of these experiments was to validate the concept of the weak radiating cell on a simple setup. On the other hand, the aim of this section is to validate the concept on a more realistic system. To this end, a simply supported rectangular plate is selected as the offensive radiating structure. An array of weak radiating cells is then mounted on the plate surface to minimize the sound radiation. This test setup allows for the consideration of several factors not included in the piston-like structure used in the previous section. In the piston-like structure, the excitation of the cell is uniform, thus exciting only the fundamental mode of the cell, i.e. normal displacement of the plate without rotation. With the plate, the cells will be excited by the translation and rotation of the plate, which in terms will excite several modes of the cell. Since an array of cells will be implemented on the plate, the interaction effects among the cells will be present in the setup. In addition, there will be dynamic interaction between the plate and the cells.

4.3.1 Experimental Setup

The plate used in the experiments is shown in Figure 4.13. The results obtained with the untreated plate will serve as a baseline to determine the performance of the array of weak radiating cells. The plate, which is constructed of steel (i.e. Modulus of Elasticity E = 195 MPa and density ρ = 7700 kg/m^3) has dimensions of 380x300x9.5 mm and is mounted to a massive steel frame through thin aluminum shims. The shims restrain the normal motion of the plate at the boundaries while allowing rotation. This effectively provides simply-supported boundary conditions. The frame is in turn attached to an enclosure box whose interior is treated with acoustic foam. The box structure also houses an excitation shaker that was positioned at 50 mm and 60 mm from the top left corner of the plate and driven with white noise from 0-1600 Hz. To monitor the plate response for various test configurations, an accelerometer and force transducer were placed at the driving point on the plate. The plate was in turn placed in a reverberant chamber. A schematic of the chamber with an experimental layout is shown in Figure

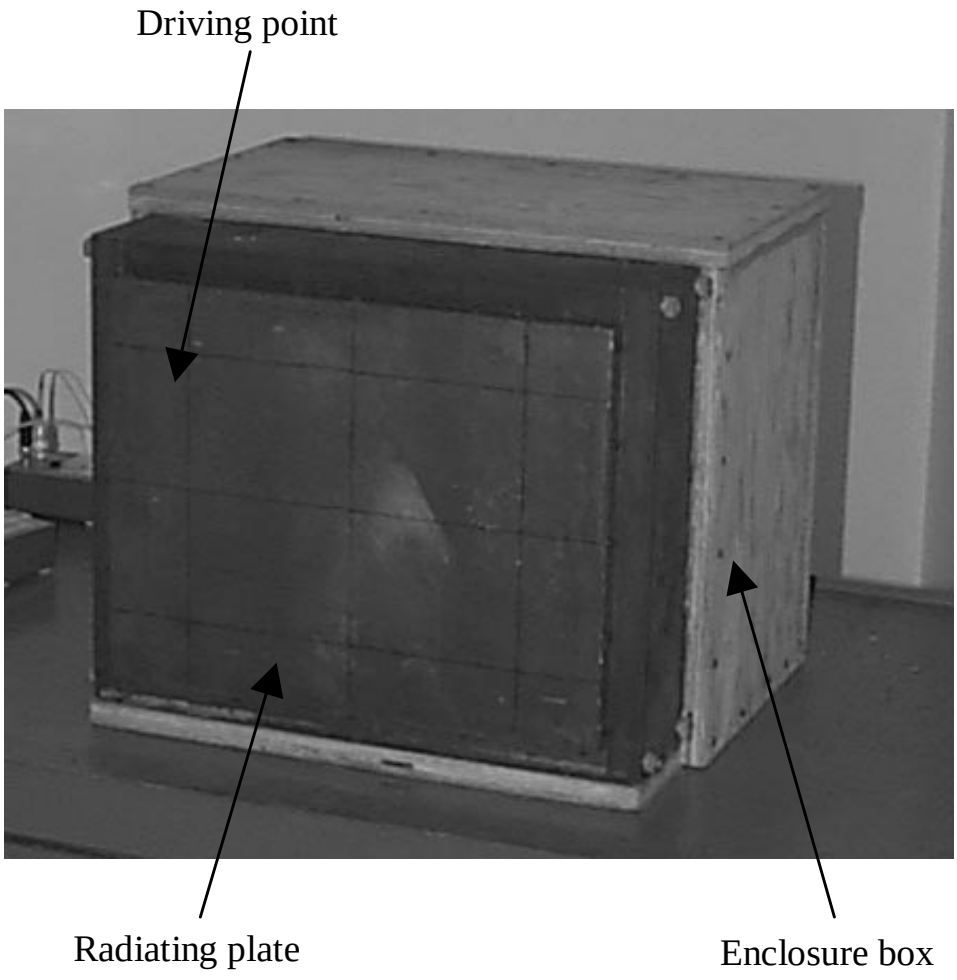

Figure 4.13 Rectangular plate with enclosure box

4.14. The plate/enclosure was positioned in a corner of the chamber with the plate facing outward. An array of ten microphones was hung on a vertical and horizontal slant to measure the sound field inside the chamber. The output from the microphones are used to compute the average sound pressure level and in turn to predict the acoustic power radiated by the structure. A laser vibrometer mounted to an automated traversing system placed in front of the structure box was utilized to perform a velocity surface scan. The laser measurements were used for modal and source strength analysis. The laser system was removed from the chamber when acoustic measurements were acquired.

The dynamic properties of the plate structure were experimentally determined by measuring the transfer function between the acceleration at the shaker location and the disturbance force, i.e. input point accelerance. This transfer function is plotted in Figure 4.22, which shows four modes present in the 0-1600 Hz frequency range. The natural frequencies of the plate are tabulated in Table 4.3. The laser vibrometer was used to scan the forced response of the plate over an 8x8 uniform grid. By plotting the magnitude and phase of the displacement response at the plate resonances, the mode shapes are easily identified. For completeness, the complex surface response for the first four modes of the plate are given in Figure 4.15a-h. Using this approach, the first four modes of the plate are identified as the (1,1), (2,1), (1,2), and (2,2) modes, respectively.

4.2.2 Weak Radiating Cell Design

To validate the proposed concept as a noise suppresion surface treatment, it was decided to cover the plate with an array nine identical weak radiating cells. Using the lumped parameter model from Chapter 2, the cell was designed so that its fundamental frequency was below the plate fundamental frequency of 414 Hz. In this way, the cells will not be strongly excited at their fundamental frequency where the sound radiation is increased by the cells. In other words, the cells fundamental resonance is placed outside the frequency range of interest. Figure 4.16 shows isometric and bottom view photographs of a weak radiating cell used in the plate experiments. A thin flexible shim was again chosen as a means of mechanically linking the rigid element, or frame, to the plate in order to create the dipole effect. The thin shim allows for stiffness in the radial

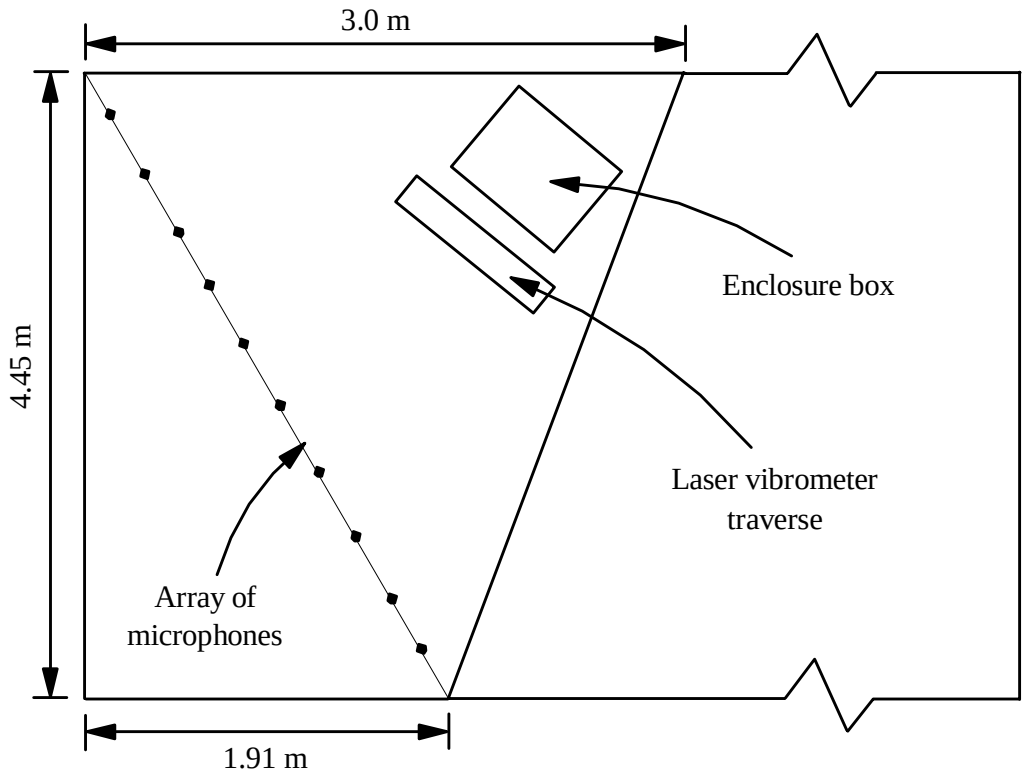

Height of chamber = 4.32 m

Figure 4.14 Experimental setup in reverberant chamber

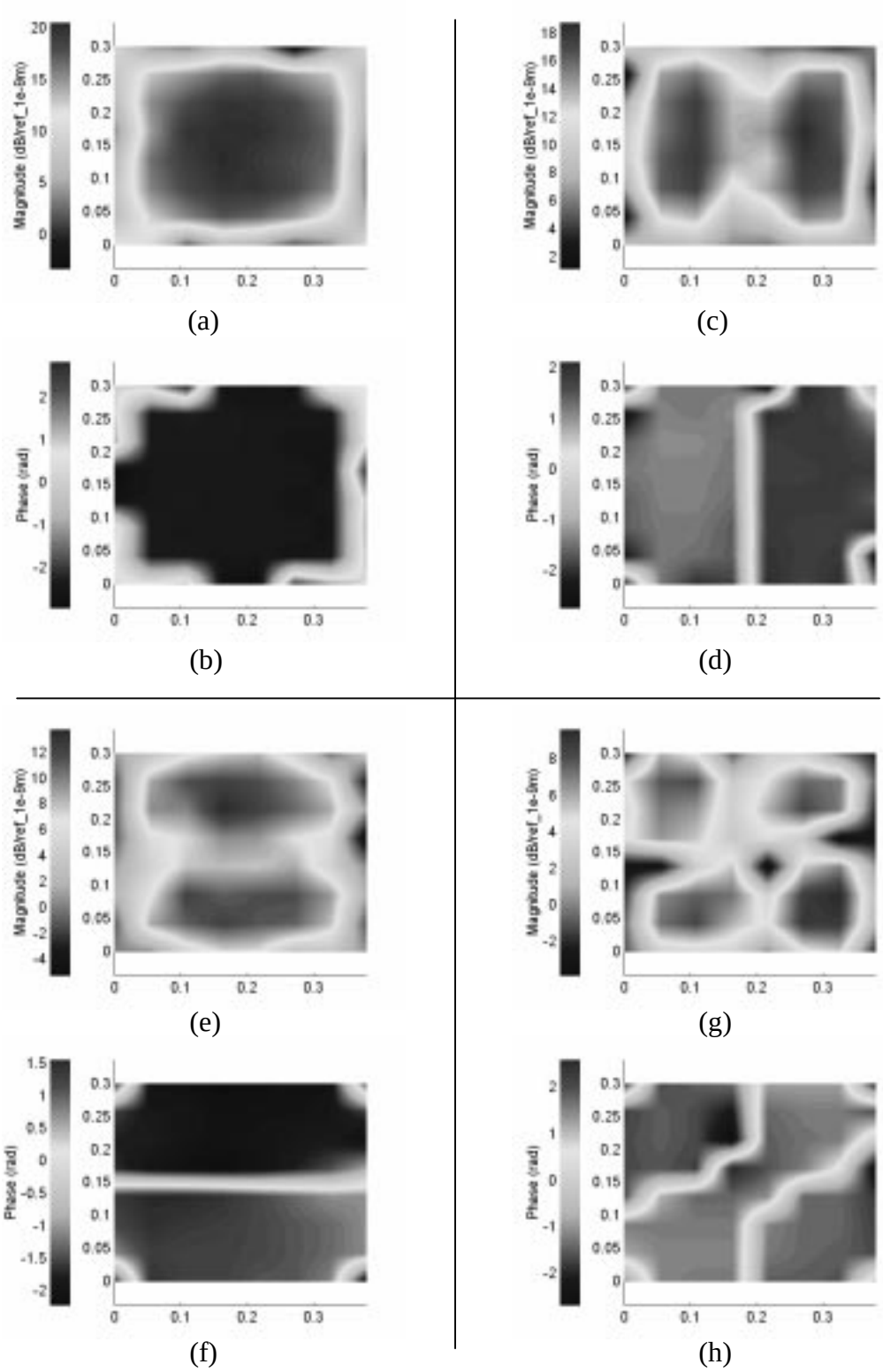

Figure 4.15 Complex surface response of plate at (a-b) 414 Hz, (c-d) 836 Hz, (e-f) 1088, (g-h) 1444 Hz

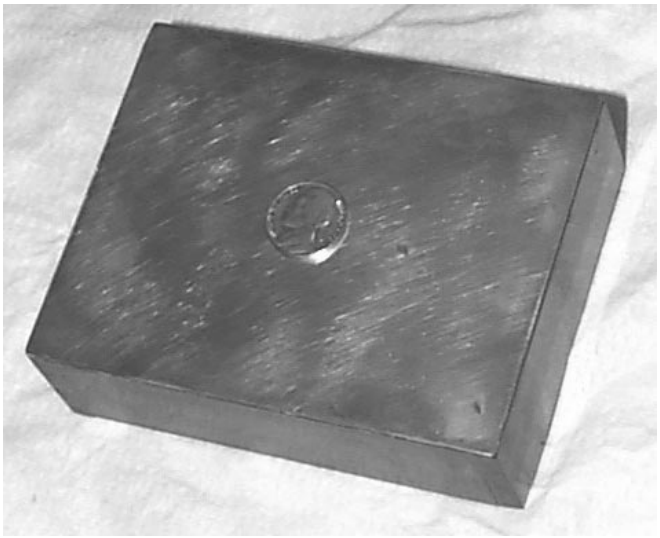

(a)

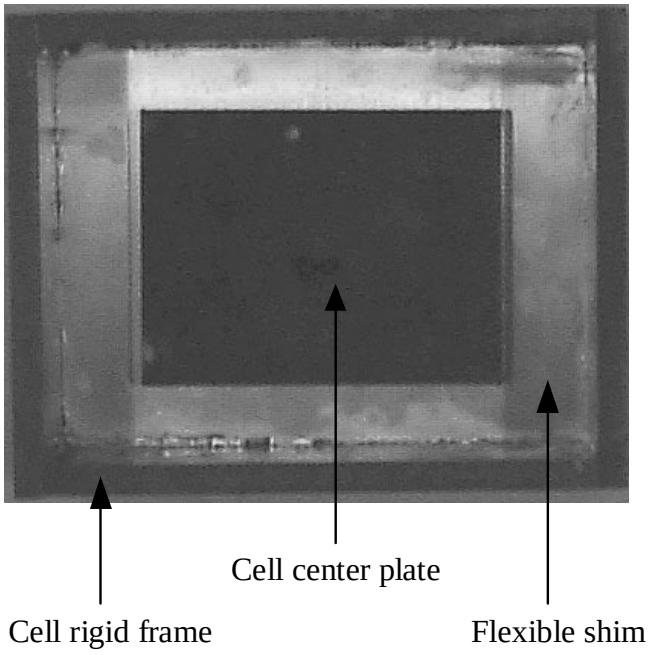

(b)

Figure 4.16 Isometric (a) and bottom (b) view photographs of cell

direction with sufficient compliance in the direction normal to the cell. The shim is made of 0.2 mm thick brass shim stock (Modulus of Elasticity E = 104 GPa, density ρ = 8500 kg/m^3). The rigid frame and plate are made of 6.4 mm thick polyvinyl chloride (PVC) (E = 800 MPa, ρ = 1577 kg/m^3). As mentioned in Chapter 3, an alternate material to be used for the rigid frame is epoxy foam, commercially known as structural foam used in the automotive industry.

Epoxy was used to fix the center mass to the shim and the shim to the frame. The global dimensions of the cell are 125x99x38 mm while the center plate dimensions are 71x52 mm. The total mass of each cell is 199 g. It is important to note that the height of 38 mm defines the cell to be a considerably compact device for passive control of low frequency structurally radiated noise.

The dynamic behavior of the nine cells was tested to investigate the variation between the cells. To this end, each cell is mounted to a rigid plate excited by a shaker driven with white noise from 0-1600 Hz as shown in Figure 4.17. A reference accelerometer was placed on the bottom of the rigid piston structure and a second at the center of the cell. The transfer functions between the acceleration measured by the two sensors for the nine cells are shown in Figure 4.18. This figure shows that the fundamental frequencies are found between 174-210 Hz, which are well below the fundamental frequency of the plate at 414 Hz. It can also be seen that the response between the cells is very consistent over the 0-1000 Hz range. Discrepancies in both magnitude and phase are evident above 1000 Hz where the higher order modes are present. It is important to remark that these higher order modes are associated with rotation of the center plate. The radiation associated to these modes is very small because they are non-volumetric modes, i.e. no net volume displaced. In fact, these higher order modes behave as dipole sources. The nine cells were mounted to the plate using an adhesive compound and were separated by a small gap. Thus, the cells were not mechanically connected. Figure 4.19 shows a picture of the nine cells mounted to the plate.

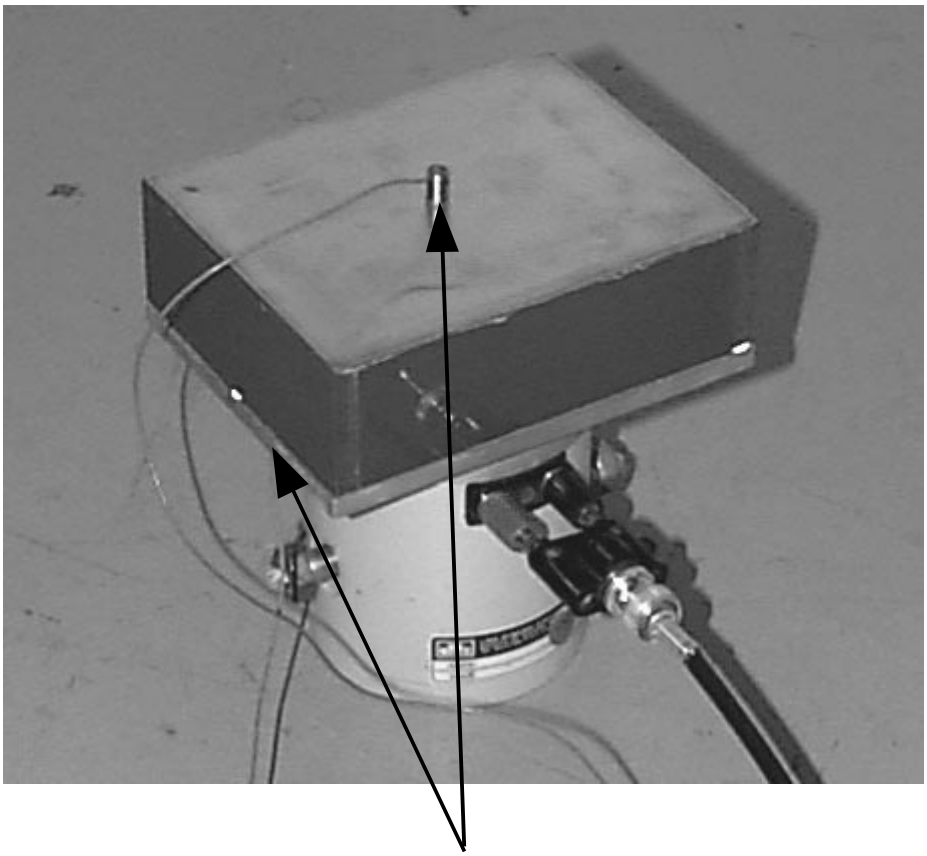

Figure 4.17 Experimental setup to test response at the center of cell

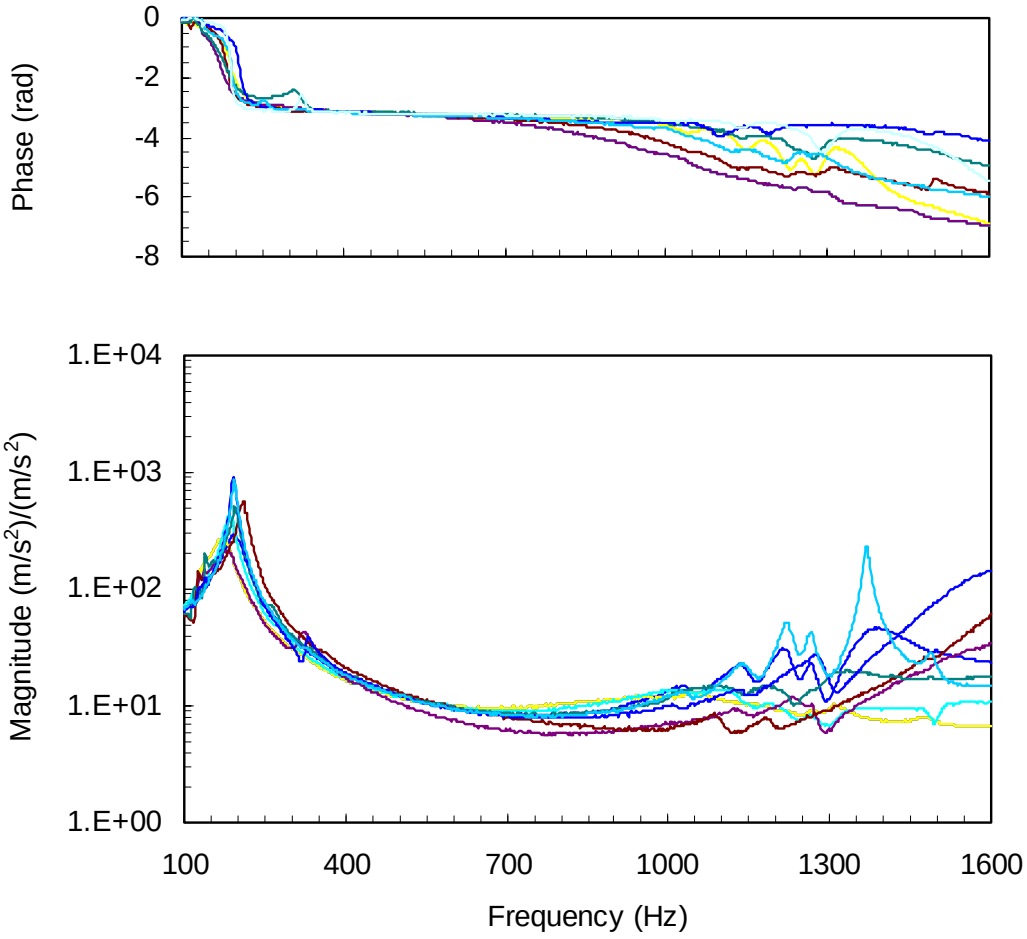

Figure 4.18 Normalized response of center plate for the nine cells used in the experiments

4.4.3 Experimental Results

The mounting of the cells on the plate structure alters both the vibrational and acoustical behavior of the system due to a number of factors. Some of the effects introduced are: (i) mass loading effects due to the added mass of the cells, (ii) additional stiffness from the cell frames, (iii) an increase in damping due to the inherent high damping of the PVC material, (iv) interaction between the dynamics of the cells and the plate; and, (v) the intentionally introduced dipole effects of the cells. With the aim of isolating these effects, three plate configurations were tested. The first configuration is the untreated plate shown in Figure 4.13. As previously mentioned, this is the baseline case and will be used to evaluate each of the effects introduced into the system. The second configuration is the plate with the array of nine weak radiating cells as shown in Figure 4.19. To isolate the mass loading, stiffness, and damping effects introduced by the cell frames, another intermediate plate configuration was tested as shown in Figure 4.20a-b. This configuration consisted of only mounting the rigid cell frames to the plate. Thus, the last two effects listed above, i.e. dynamic interaction and the dipole effects are not listed in this configuration. The ratio of the total mass of the nine cell frames to the mass of the plate is 17% while the mass ratio for the complete cells is 21%.

An ideal design for the rectangular cells would be to allow only the (1,1), or piston, mode to be excited in the frequency range of concern. However, this may be unrealistic and steps should be taken to identify any higher order of modes present. In addition, the plate to which the cells are mounted may introduce compliance to the system that will alter the resonant frequencies of the cells. Thus, a modal analysis was performed on the cells using a modal hammer for two configurations. The first tested the nine cells individually on a rigid modal testing block. In the second configuration, the cells were tested with all nine cells on the plate. A layout used for the tests on the plate is given in Figure 4.21. A similar layout of the apparatus was used when testing the cells individually on the modal testing block. For both cases, the modal hammer impulse excitation was applied in the lower right quarter of each cell. The response was then captured by placing an accelerometer in each of the locations noted in Figure 4.21. Through investigation of the real and imaginary components of the acquired transfer

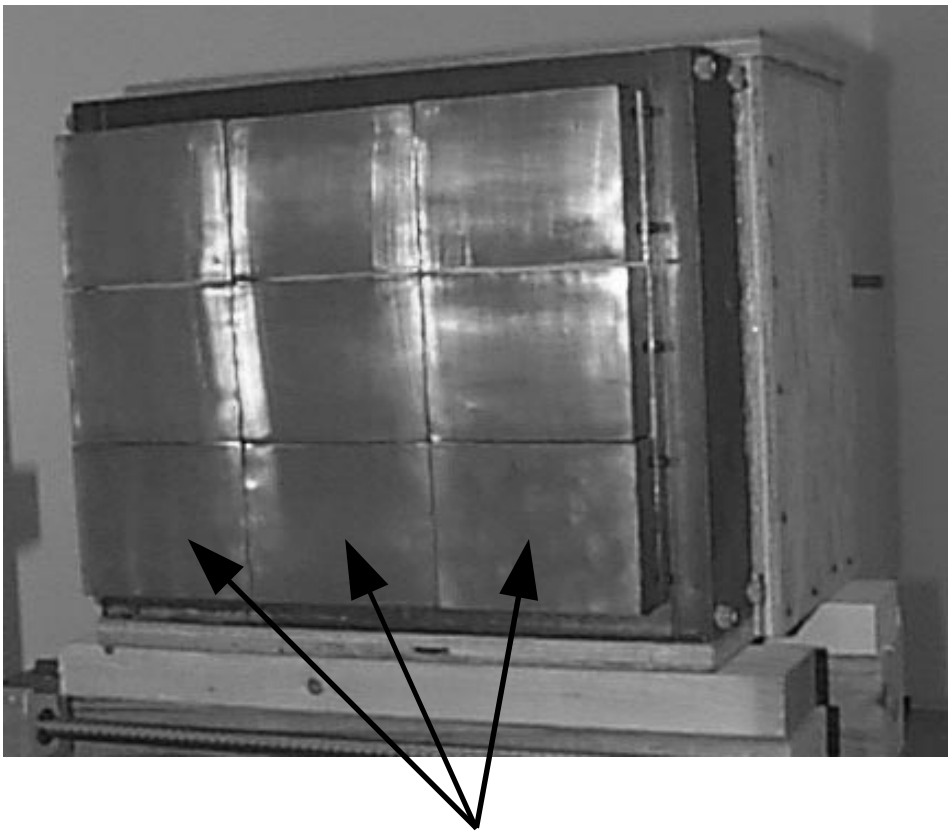

Figure 4.19 Plate with array of weak radiating cells

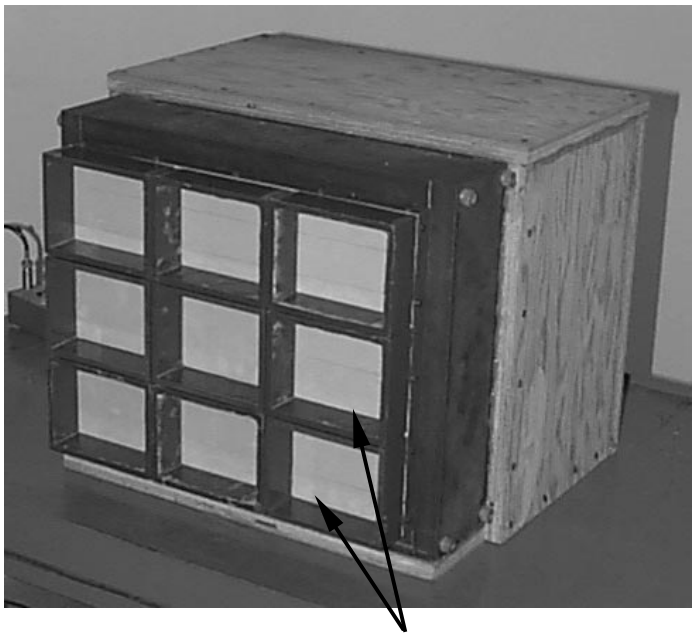

(a)

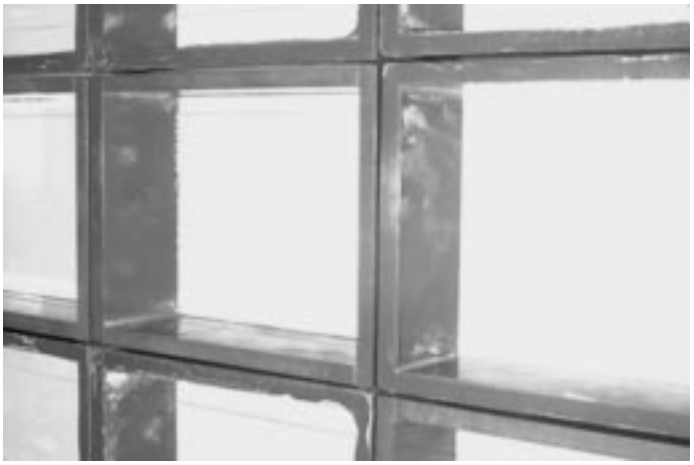

(b)

Figure 4.20 (a) Plate with cell frames and (b) close up of frames

functions, the mode shapes and their resonant frequencies were clearly identified. The tests revealed that the (1,1), (2,1), (1,2) modes are present, with the (2,2) mode lying just outside the frequency range of interest for most of the nine cells. The resonant frequencies of the cells on and off the plate for the four modes are given in Table 4.2. In comparison of the on and off plate configurations, there is little or no deviation in the resonant frequencies due to the potential plate dynamics. Knowing the plate stiffness has virtually no effect on the dynamics of the cells is useful for the design of the cell parameters.

To estimate the impact of the cells on the dynamic properties of the plate, the transfer function between the acceleration and the input force at the driving point of the plate for the three configurations was measured and is given in Figure 4.22. The measured resonance frequencies for these three configurations are presented in Table 4.3. It can be observed that by adding the cell frames to the plate leads to a downward shift in the resonance frequencies due to mass loading and a reduction of the response due to damping. The results in Table 4.3 show that the four resonance frequencies of the plate are reduced by approximately the same factor of 0.94 and the increase in modal damping is very pronounced for the higher modes. Figure 4.22 shows that by adding the cell shims and center masses, the response of the plate is not significantly affected as compared with the case of the plate with frames. In fact, inspection of the natural frequencies in Table 4.3 reveals two effects due to shims and center plates. The first two resonance frequencies are slightly reduced, indicating additional mass loading effects. Note that from Figure 4.18, the cells do not exhibit any dynamics, i.e. modes, within the 300-1000 Hz range that can interact with the first two modes of the plate. On the other hand, above 1000 Hz, there are several modes that can dynamically interact with the third and fourth mode of the plate which is indicated by the slight increase in the natural frequencies of these two modes. Thus, the weak radiating cells are probably behaving as an array of dynamic vibration absorbers at higher frequencies.

One of the main goals of this study is to verify that the array of weak radiating cells mounted on the plate effectively creates an array of distributed dipole

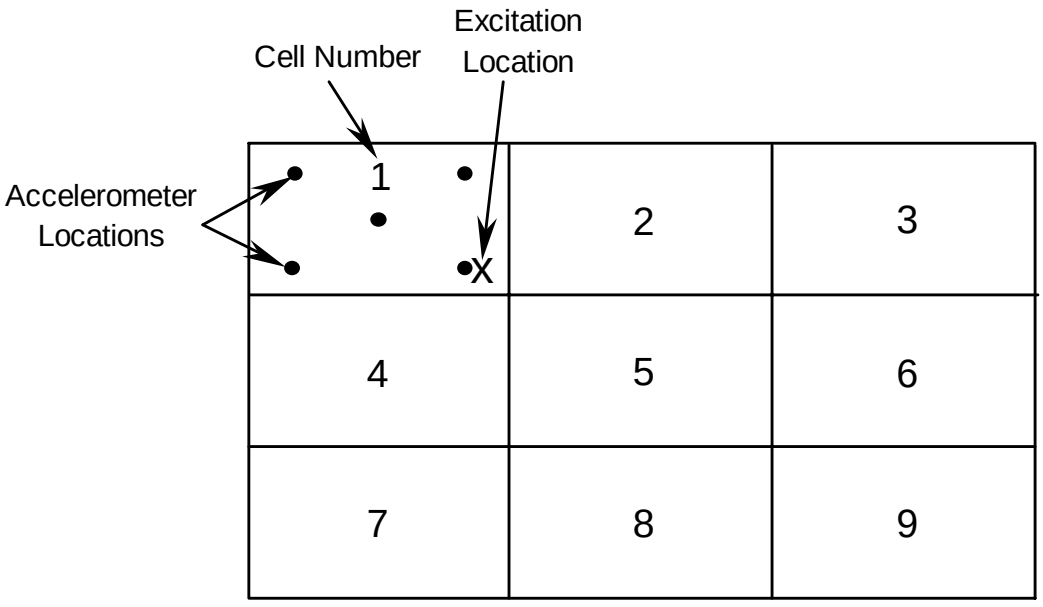

Figure 4.21 Apparatus layout for modal tests

Table 4.2 Cell resonant frequencies on and off plate

Cell #	(1,1) Mode f_n in Hz		(2,1) Mode f_n in Hz		(1,2) Mode f_n in Hz		(2,2) Mode f_n in Hz	
	Individual	On Plate	Individual	On Plate	Individual	On Plate	Individual	On Plate
1	164	166	230	230	----	---	> 1600	---
2	202	202	248	248	320	322	> 1600	---
3	200	198	290	290	320	322	>1600	> 1600
4	200	204	280	280	340	342	> 1600	---
5	222	220	284	282	370	370	> 1600	1520
6	202	204	262	262	340	340	---	---
7	210	210	264	264	350	348	> 1600	> 1600
8	198	190	236	232	298	290	> 1600	1462
9	208	208	270	270	360	356	> 1600	>1600

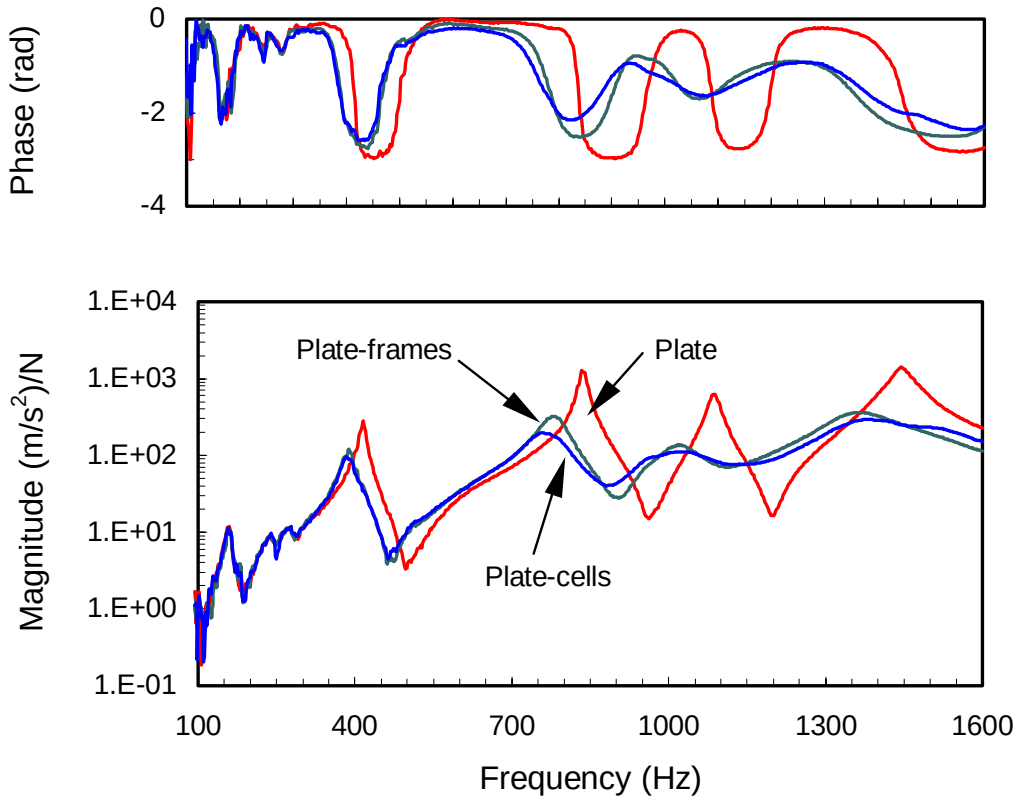

Figure 4.22 Acceleration to force transfer function at driving point

Table 4.3 Plate resonant frequencies for the three test configurations

Configuration	Mode 1	Mode 2	Mode 3	Mode 4
Plate	414 Hz	836 Hz	1088 Hz	1444 Hz
Plate-frames	390 Hz	784 Hz	1036 Hz	1354 Hz
Plate-cells	388 Hz	776 Hz	1046 Hz	1378 Hz

acoustic sources. To investigate this, a 21x21 grid laser scan of the velocity response of the cells on the vibrating plate was performed. Figure 4.23a-h shows the surface response phase and magnitude at the first four modes of the plate-cells structure, i.e 388, 776, 1046, and 1378 Hz, respectively. Figure 4.23a shows that the magnitude of the cell frames response follows the shape of the (1,1) mode of the rectangular plate. More importantly, the phase in Figure 4.23b reveals that the inner surfaces of the cells are out-of-phase with respect to the response of the cell frames, i.e. the frames show a phase of approximately π radians while the phase of the cell inner surfaces is 0. This clearly identifies that an array of acoustic dipoles has been created. The magnitude and phase in Figure 4.23c-d again reveals this fact at the (2,1) mode of the plate. The response of the cells follows the shape of this mode, since a vertical nodal line is evident in Figure 4.23c-d and the response of the left half is out-of-phase with respect to the response of the right half of the plate. In addition, the cells' inner surfaces are respectively out-of-phase with the cell frames on either side of the plate. Through careful inspection, Figure 4.23e-h reveals that dipoles are also created at the (1,2) and (2,2) modes of the plate. In looking at the phase responses, the cell frames are consistently and spatially out-of-phase with the cell inner surfaces, depending on the mode shape being analyzed. Therefore, it should be anticipated that sound reduction will be achieved throughout the entire frequency band.

Using the velocity data obtained from the laser scans, the complex source strength of the plate with and without the cells can be computed using the following discrete equations

$$Q_{plate} = \sum_{i}^{64} v(\omega)_i \cdot S_i \tag{4.3}$$

for the plate and

$$Q_{cells} = \sum_{i}^{441} v(\omega)_i \cdot S_i \tag{4.4}$$

for the plate with the cells, where v is the complex velocity as a function of frequency at the locations of the laser scan, S_i is the corresponding area associated to the velocity, and i is the index for the number of scanning points. The source strength magnitude for the

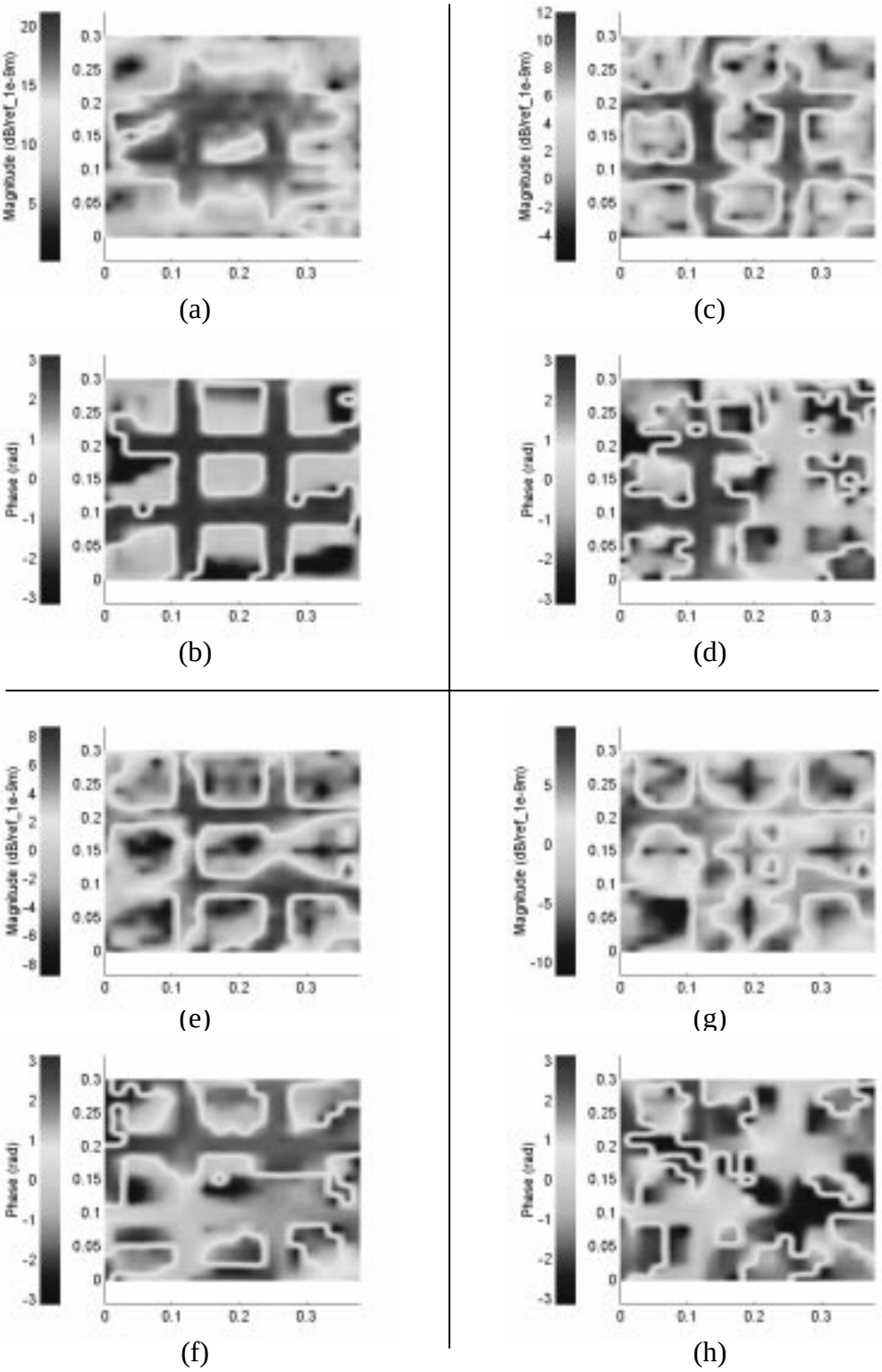

Figure 4.23 Complex surface response of plate with cells at (a-b) 414 Hz, (c-d) 836 Hz, (e-f) 1088, (g-h) 1444 Hz

plate with and without the cells is then plotted in Figure 4.24. The response of the cells lead to a significant reduction in the system source strength throughout a wide frequency range, especially near the first mode of the plate since this is the only volumetric mode. The other three modes of the original plate, i.e. (2,1), (1,2), and (2,2) are non-volumetric and thus not evident in Figure 4.24. The reduction of the source strength at the higher frequencies is in part due to the reduction in the response as a result of the mass loading effect. A key point to note from Figure 4.24 is that the fundamental resonances of the cells do not significantly contribute to the total source strength radiated from the structure, even though each cell has gone through a resonance with a 180° phase shift. This is because the resonances are below the frequency range that the plate is greatly excited, i.e, the shaker is ineffective in exciting the plate in this frequency range. Thus the purpose for designing the cell resonances to be around 200 Hz, which is well below the first resonance of the plate. This gives a general interpretation for achieving optimal reduction, which is to place the cell resonances in a frequency region that the structure has minimal excitation while allowing the cells to radiate as dipoles throughout a wide frequency range.

To assess the performance of the array of weak radiating cells applied to the vibrating plate, the sound pressure data taken in the reverberant chamber for the three test configurations was used to determine the radiated acoustic power. The sound power level in a diffuse or reverberant sound field is estimated as (26)

$$L_w = \overline{L}_p - 10\log(T_{60}) + 10\log(V) + 10\log\left(1 + \frac{S_r\lambda}{8V_r}\right) + 10\log\left(\frac{B}{1000}\right) - 14\text{dB} \qquad (4.5)$$

where $\overline{L}_p$ is the measured space-energy average sound pressure level in the chamber and T_{60} is the reverberation time of the reverberant chamber in seconds. The variables S_r and V_r are the room total surface area and volume, respectively, computed from the dimensions given in Figure 4.14, and λ is the acoustic wavelength in meters. Using Equation (4.5), the sound power level spectra are computed for the three test configurations and plotted in Figure 4.25. As previously mentioned, there are mass loading and damping effects introduced into the system by applying the cell frames to the plate. These effects lead to a reduction of the radiated power at the new resonance

frequencies of the plate-frames system as compared to the radiated power at the resonance frequencies of the untreated plate, e.g. reductions of approximately 6 dB are observed in Figure 4.25. At off resonance frequencies, there is an increase in radiated power due to the corresponding increase in the structural response as shown in Figure 4.22. The resulting changes in the sound power levels due to the mounting of the cell frames to the plate is also illustrated in Figure 4.26, which shows sound power level reduction with respect to the baseline case. An overall sound power level reduction of 3.5 dB was obtained in the 100-1600 Hz frequency range. As shown in Figure 4.25, the sound power spectrum after the complete weak radiating cells were mounted on the plate shows a power level reduction over the full frequency range of interest, i.e. both on and off resonance frequencies. This is very clear in the plot of sound power reduction in Figure 4.26 which shows that there is no sound increase at any of the frequencies in the 100-1600 Hz. An overall sound power level reduction of 10.2 dB was achieved in the frequency range of 100-1600 Hz as compared to the untreated plate. This is an additional 6.7 dB gained from the weak radiating properties, i.e. dipole effects, of the cells. Figure 4.27 more clearly illustrates the advantage of the dipole effect by plotting the difference in sound power level reduction between the plate-cells and plate-frames configurations. The reduction in this figure is the gained sound power level reduction attributed solely to the created dipole effect, beyond the gains achieved from mass loading and damping effects. It is important to remark that, as shown in Figure 4.22, the acceleration of the driving point has little variation between the plate-frames configuration and that of the plate-cells configuration. However, the response of the cells led to a significant reduction in the sound radiation because the cells behave as acoustic dipole sources.

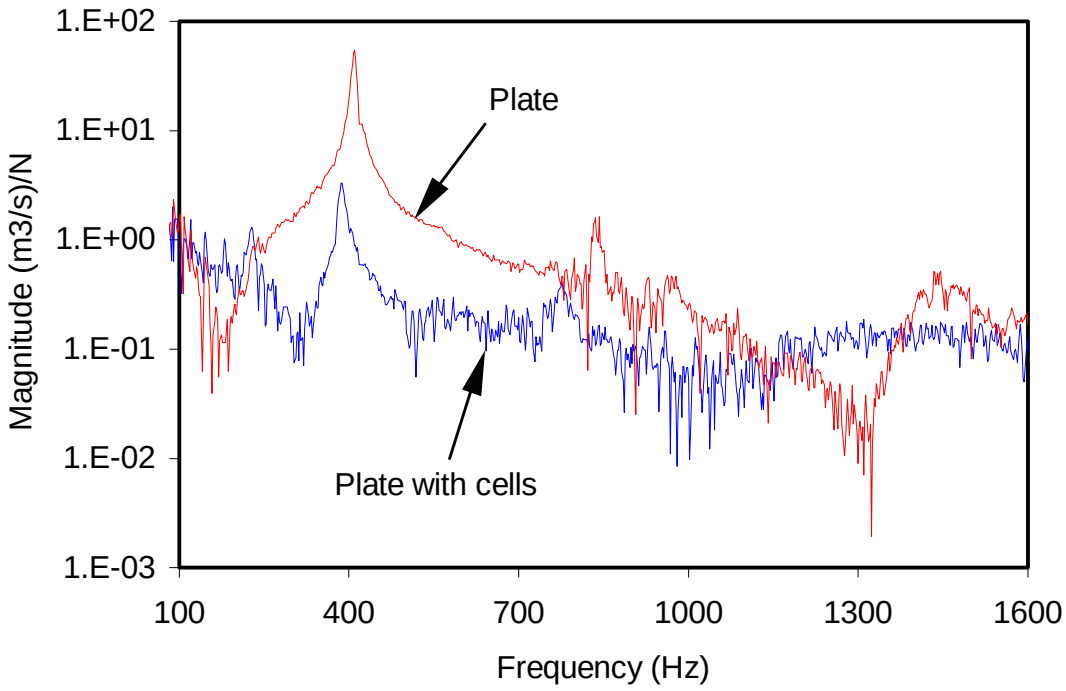

Figure 4.24 Source strength magnitude of plate with and without cells

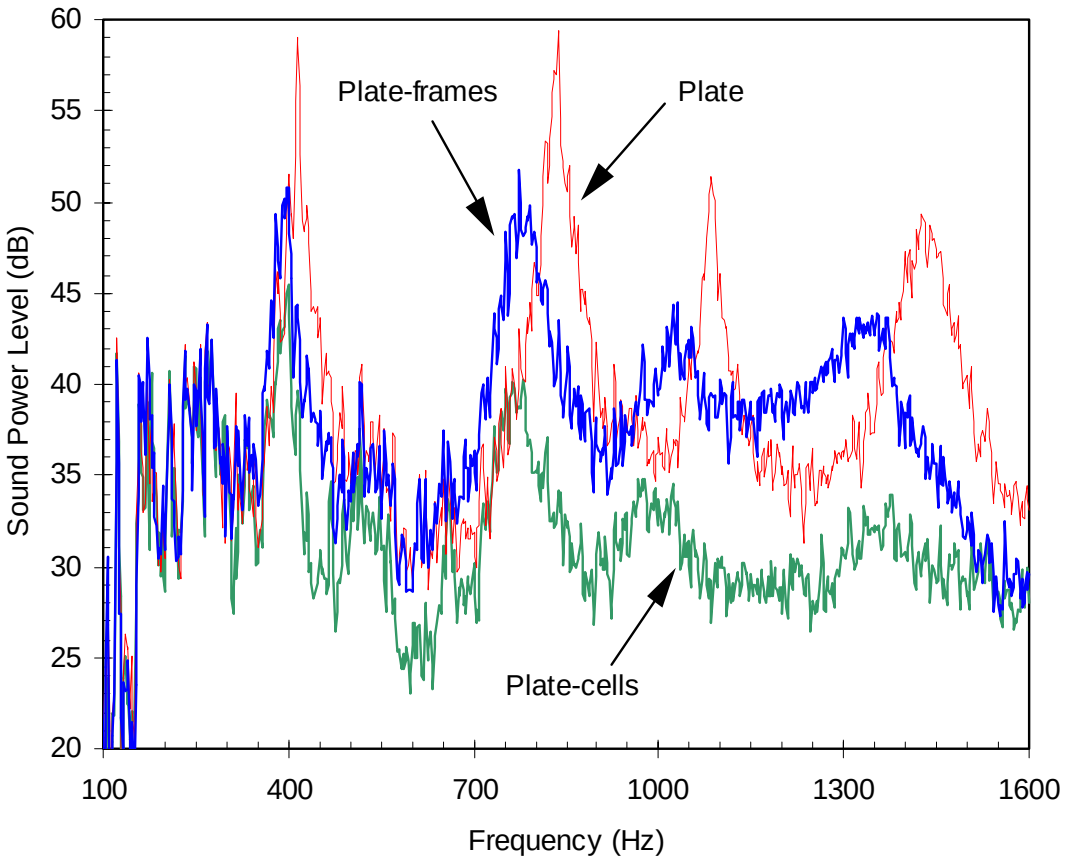

Figure 4.25 Sound power level spectra for the three test configurations

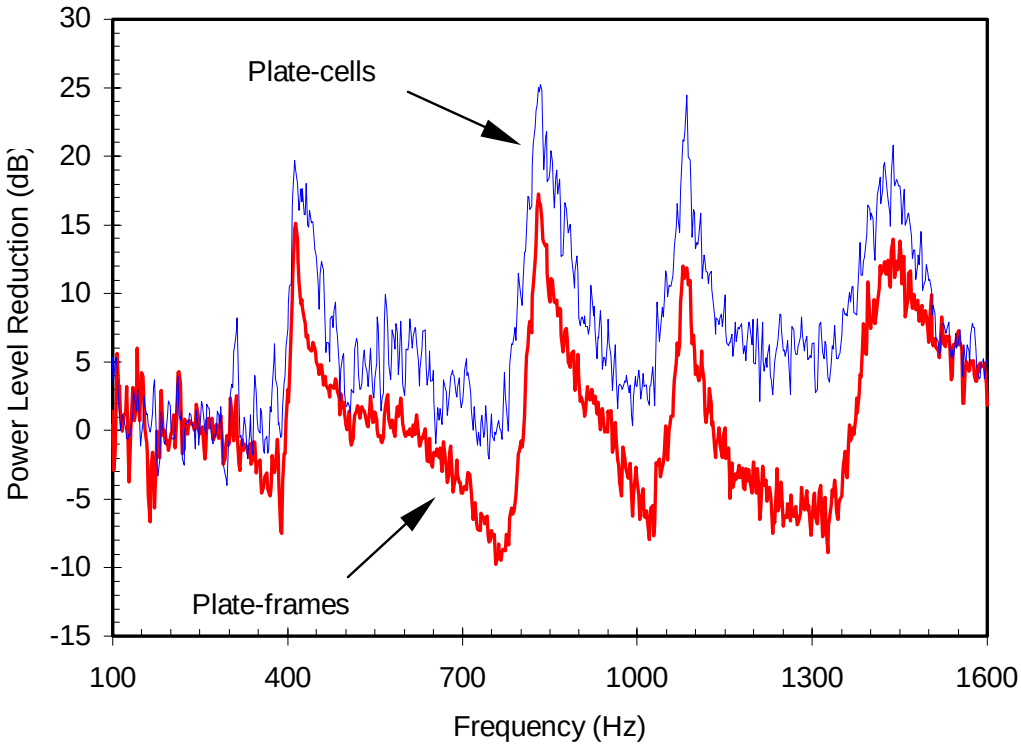

Figure 4.26 Sound power level reduction

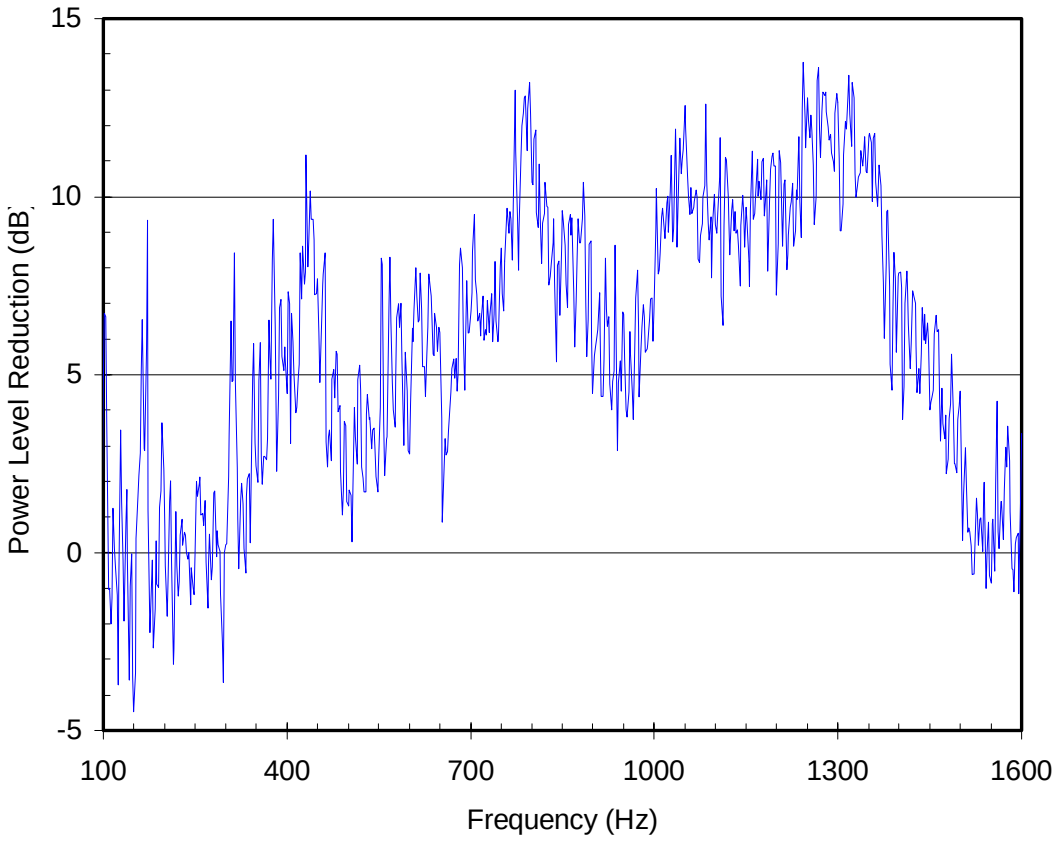

Figure 4.27 Sound power level reduction attributed solely to the dipole effect

Chapter 5

Conclusions

The new concept of the weak radiating cell was introduced as a low frequency passive noise control device for radiating structures. The concept takes advantage of the inefficient radiating properties of an acoustic dipole to achieve broadband reduction for frequencies below 1000 Hz. Two implementations of the weak radiating cell concept were developed during the pioneering of this work. Theoretical models were derived for each implementation and their performance characterized through source strength and sound power reduction. Experiments were performed on a single weak radiating cell on a piston-like structure and on an array of cells applied to a rectangular plate.

Through the simple models developed, the performance of the two cell implementations can be compared. The mechanically coupled cell is most likely simpler to implement than the mechanically and acoustically coupled. On the other hand, the performance of the second cell implementation is better than the first, achieving higher power reduction over a wider frequency range. A parametric study revealed the significant effects of contributing parameters to the achieved sound power level reduction. This information can be used to guide in the design of the weak radiating cell characteristics for a specific application in order to achieve optimal reduction. An essential for optimal reduction is to design the cell resonance(s) out of the frequency range of interest or in a region where the offending structure does not have significant response.

The developed cell models indicated theoretical potential for significant low frequency reduction, so the concept was applied to a piston-like structure and its dynamics were analyzed. Only the results of the mechanically coupled cell were presented because of difficulties encountered with the implementation of the mechanically and acoustically coupled cell. The problem originated from the fact that the

elastic medium used in the experiments, acoustic foam, lacked the required stiffness in the direction perpendicular to the piston face. The potential exists for future work to implement a more effective elastic material. The experiments on the mechanically coupled cell achieved encouraging results with an overall sound power level reduction of 5.2 dB from 400-1000 Hz with values exceeding 30 dB at discrete frequencies. This yields close agreement with theoretical predictions, which suggests a 6.7 dB overall reduction over the 400-1000 Hz range.

The successful results of the experiments with a weak radiating cell on simple piston-like structure led to the application of an array of cells to a more complex rectangular plate structure. The cells were designed to possess identical dynamics with resonant frequencies below that of the fundamental plate resonance. This ensured that the adverse effects of the cell resonances would not be present in the power spectra. In addition to characterizing the performance of the cell's dipole effects, mass loading and damping effects of the cell frames were isolated. By simply applying the cell frames to the plate, mass loading and damping proved to obtain a 3.5 dB reduction in power between 100-1600 Hz. However, a 10.2 dB reduction was achieved after applying the cell shims, i.e. after creating an array of acoustic dipoles.

The theoretical and experimental results presented in this thesis clearly identify the potential for the weak radiating cell concept to be applied to realistic systems as a passive low frequency noise control device for acoustically offensive radiating structures. Prior to integrating the weak radiating cell concept into realistic systems, there are a few areas of this research that may require some future work. These areas include investigation of the cell frames acting as vibration absorbers at high frequencies, development of a model coupling the array of cells to the plate dynamics, and the possibility of creating a finite element model to account for any umodeled cell dynamics such as acoustic cavity modes. In addition, if it is desired to pursue a hybrid weak radiating cell further modeling will be required to characterize the effects of the control system.

References

[1] Murray, B. S. and J. F. Wilby, 1978, "Helicopter Cabin Noise – Methods of Source and Path Identification and Characterization", Proceedings of an International Specialist Symposium held at NASA Langley Research Center, Hampton, Va., May 22-24, 1978, NASA Conference Publication 2052.

[2] Wilby, J. F., 1996, "Aircraft Interior Noise", Journal of Sound and Vibration, 90(3), pp. 545-564.

[3] Brungardt, K., J. Vierengel, and K. Wiessman, 1997, "Active Structural Acoustic Control of Noise from Power Transformers", Noise-Con '97, Pennsylvania State University, June 15-17, pp. 173-182.

[4] Prydz, R. A. et al., 1990, "Transmission Loss of a Multilayer Panel with Internal Tuned Helmholtz Resonators", Journal of the Acoustical Society of America, 87(4), pp.1597-1602.

[5] Lee, J. and G. W. Swenson, Jr., May-June 1992, "Compact Sound Absorbers for Low Frequencies", Noise Control Engineering Journal, pp. 109-117.

[6] St. Pierre, R. L., Jr., and G. H. Koopman, June 1995, "A Design Method for Minimizing the Sound Power Radiated from Plates by Adding Optimally Sized, Discrete Masses", Transactions of the ASME Special 50th Anniversary Design Issue, vol. 117, pp. 243-251.

[7] Abe, M. and T. Igusa, 1995, "Tuned Mass Dampers for Structures with Closely Spaced Natural Frequencies", Earthquake Engineering and Structural Dynamics, vol. 24, pp. 247-261.

[8] Jolly, M. R. and J. Q. Sun, "Passive Tuned Vibration Absorbers for Sound Radiation Reduction from Vibrating Panels", Journal of Sound and Vibration, 191(4), pp.577-583, 1996.

[9] Nelson, P. A. and S. J. Elliott, 1992, *Active Control of Sound*, Academic Press, San Diego.

[10] Fuller, C. R., S. J. Elliott, and P. A. Nelson, 1996, *Active Control of Vibration*, Academic Press, San Diego.

[11] Johnson, B. D., 1997, "Broadband Control of Plate Radiation using a Piezoelectric, Double-Amplifier Active-Skin", Master's Thesis, Virginia Polytechnic Institute and State University.

[12] Gentry, S. A., C. Guigou, and C. R. Fuller, April 1997, "Smart Foam for Applications in Passive-Active Noise Radiation Control", Journal of the Acoustical Society of America, 101(4), pp. 1771-1778.

[13] Franchek, M. A., M. W. Ryan, and R. J. Bernhard, 1995, "Adaptive Passive Vibration Control", Journal of Sound and Vibration, 189(5), pp. 565-585.

[14] Aldrin, J., D. C. Conrad, and W. Soedel, 1996, "Investigation of Passive and Adaptive Dynamic Absorbers Applied to an Automatic Washer Suspension Design", Proceedings of the SPIE – The International Society for Optical Engineering, vol. 2720, pp. 50-61.

[15] Sun, J. Q., M. R. Jolly, and M. A. Norris, June 1995, "Passive, Adaptive and Active Tuned Vibration Absorbers – A Survey", Transactions of the ASME Special 50th Anniversary Design Issue, vol. 117, pp. 234-242.

[16] St. Pierre, R. L., Jr., W. Chen and G.H. Koopman, 1995, "Design of Adaptive Panels with High Transmission Loss Characteristics", American Society of Mechanical Engineering, NewYork. Presented at the 1995 ASME International Mechanical Engineering Congress and Exposition, San Francisco, Ca., November 12-17.

[17] Naghshineh, K. and V. B. Mason, 1996, "Reduction of Sound Radiated from Vibrating Sources via Active Control of Local Volume Velocity", Applied Acoustics, vol. 47, pp. 27-46.

[18] Johnson, M. E. and S. J. Elliott, October 1995, "Active Control of Sound Radiation using Volume Velocity Cancellation", Journal of Acoustical Society of America, 98(4), pp. 2174-2186.

[19] Sharp, S. J., G. H. Koopman, and W. Chen, 1997, "Transmission Loss Characteristics of an Active Trim Panel", Proceedings from Noise-Con 97 held at The Pennsylvania State University, pp. 149-160, June 15-17, 1997.

[20] Kinsler, L. E., A. R. Frey, A. B. Coppens, and J. V. Sanders, 1982, *Fundamentals of Acoustics*, Third Edition, Canada, John Wiley & Sons.

[21] Temkin, S., Elements of Acoustics, New York, John Wiley & Sons, 1981.

[22] Novacore Structural Foam Brochure, Novamax Technologies, 13650 E. 10 Mile Road, Warren, Michigan.

[23] Thomson, W. T. *Theory of Vibration with Applications*, Fourth Edition, New Jersey, Prentice Hall, 1993.

[24] A. Liessa, *Vibration of Plates*, New York, Acoustical Society of America, 1993, pp. 32-33

[25] Pierce, A. D., *Acoustics: An Introduction to its Physical Principles and Applications*, New York, Acoustical Society of America, 1989.

[26] Beranek, L. L. and I. L. Ver, 1992, *Noise and Vibration Control Engineering: Principles and Applications*, New York, John Wiley and Sons.

APPENDIX A

Single DOF Model of Mechanically Coupled Cell

This Appendix develops the equation of motion for the single degree-of-freedom model of the mechanically coupled cell. A derivation is given for internal acoustic pressure that is required for the model.

A.1 Internal Acoustic Pressure

Internal acoustic pressure is defined as the difference between the instantaneous and static pressures for a fluid filled volume, and is given as [20]

$$p = P - P_o \tag{A.1.1}$$

Assuming the acoustic processes are nearly adiabatic, the equation of state for a perfect gas is defined as

$$P_o V_o^{\gamma} = P V^{\gamma} = K \tag{A.1.2}$$

where P_o, P, V_o and V are the static and instantaneous pressures and volumes, respectively, γ is the ratio of specific heats, and K is a constant.

Partial differentiating Eq. (A.2) yields

$$\frac{\partial P_o}{\partial V_o} = -\frac{\gamma K V_o^{-\gamma}}{V_o} = -\frac{\gamma P_o}{V_o} \tag{A.1.3}$$

which can be simplified to

$$p = -\frac{\gamma P_o \Delta V}{V_o} \tag{A.1.4}$$

where ΔV is the change in volume.

The speed of sound in fluids is defined as

$$c = \sqrt{\frac{\gamma P_o}{\rho_o}} \tag{A.1.5}$$

where ρ_o is the constant equilibrium density of the fluid. Combining Eqs. (A.4) and (A.5) gives the form of internal acoustic pressure that is used for the development of the cell models

$$p = \frac{c^2 \rho_o}{V_o} \Delta V \tag{A.1.6}$$

A.2 Equation of Motion

The mechanical behavior of the cell can be depicted as a single degree-of-freedom lumped parameter system with a base input. The simplified model is shown in Figure 2.3b, and the free body diagram of the plate is given below.

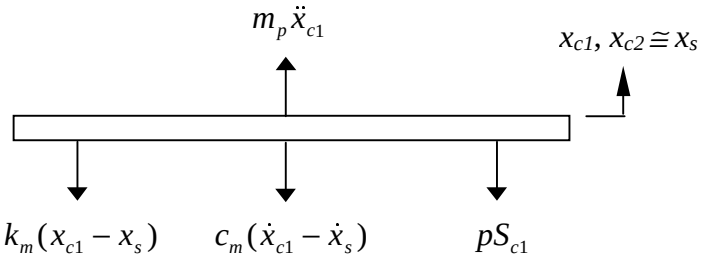

Figure A.1 Free body diagram of mechanically coupled cell

As seen in Eq. (A.6), the internal acoustic pressure is a function of the change in cavity volume due to the plate dynamics. By substituting the change in volume $\Delta V = (x_{c1}\text{-}x_s)$ into Eq. (A.6), the acoustic pressure is given as

$$p = -\frac{c^2 \rho_o}{V_o} \cdot (x_{c1} - x_s) \cdot S_{c1} \tag{A.2.1}$$

Performing a force balance from the free body diagram yields the equation of motion for the mechanically coupled cell, and is given as

$$m_p \ddot{x}_{c1} + c_m \dot{x}_{c1} + k_t x_{c1} = c_m \dot{x}_s + k_t x_s \tag{A.2.2}$$

where the stiffness of the system is

$$k_t = k_m + \frac{c^2 \rho_o S_{c1}}{V_o} = k_m + k_f \tag{A.2.3}$$

and k_m is the mechanical stiffness and k_f is the stiffness due to the fluid in the cavity.

APPENDIX B

Two DOF Model of Mechanically and Acoustically Coupled Cell

In this Appendix, the equations of motion for the two degree-of-freedom model of the mechanically and acoustically coupled cell are developed. Though the equations are coupled, one primarily represents the mechanical behavior of the plate while the other represents the behavior of the fluid in the orifice. The simplified model of the system is illustrated in Figure 2.7b. The free body diagrams for the plate and the fluid element are given in Figures B.1 and B.2.

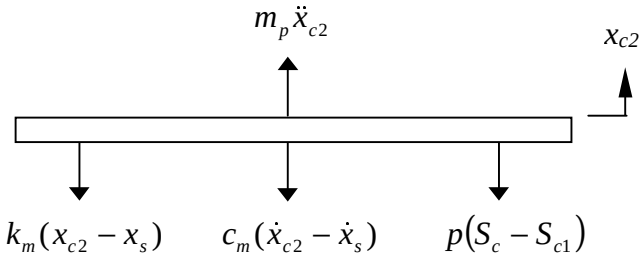

Figure B.1 Free body diagram of plate

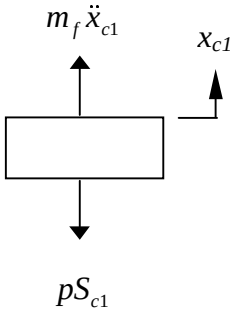

Figure B.2 Free body diagram of fluid element

Performing a force balance on the free body diagram of the plate obtains the following

$$\Sigma F_{plate} = m_p\ddot{x}_{c2} = -c_m(\dot{x}_{c2}-\dot{x}_s) - k_m(x_{c2}-x_s) - p(S_c-S_{c1}) \qquad \text{(B.1)}$$

where S_c is the surface area of the cavity. By substituting in the acoustic pressure from Eq. (A.6), which is a function of the change in volume given in Eq. (2.18), the first equation of motion for the system reduces to

$$m_p \ddot{x}_{c2} + c_m \dot{x}_{c2} + \left(k_m + \frac{c^2 \rho (S_c - S_{c1})^2}{V_o} \right) x_{c2} + \left(\frac{c^2 \rho S_{c1} (S_c - S_{c1})^2}{V_o} \right) x_{c1}$$
$$= c_m \dot{x}_s + \left(k_m + \frac{c^2 \rho S_c (S_c - S_{c1})^2}{V_o} \right) x_s \qquad \text{(B.2)}$$

Using the free body diagram for the fluid element in the orifice, the following force balance is obtained

$$\Sigma F_{fluid} = m_f \ddot{x}_{c1} = p S_{c1} \qquad \text{(B.3)}$$

By again substituting in the change in volume and acoustic pressure into Eq. (B.3), the second equation of motion for the system reduces to

$$m_f \ddot{x}_{c1} + k_f x_{c1} + \left(\frac{c^2 \rho_o S_{c1} (S_c - S_{c1})}{V_o} \right) x_{c2} = \left(\frac{c^2 \rho_o S_{c1} S_c}{V_o} \right) x_s \qquad \text{(B.4)}$$

APPENDIX C

Continuous Model of the Elastic Medium for the Mechanically and Acoustically Coupled Cell

This Appendix develops a continuous model for the elastic medium in the mechanically and acoustically coupled cell through a wave analysis. The obtained plate response is a function of the structure response and takes place of the single degree-of-freedom assumption used in the derivation of Chapter 2.

Though an elastic medium possesses an infinite number of internal resonances, a single degree-of-freedom approximation is typically valid for frequencies beyond the first mode, but lower than the second mode. Figure B.1 illustrates the elastic medium to be modeled as a continuous system through a wave analysis.

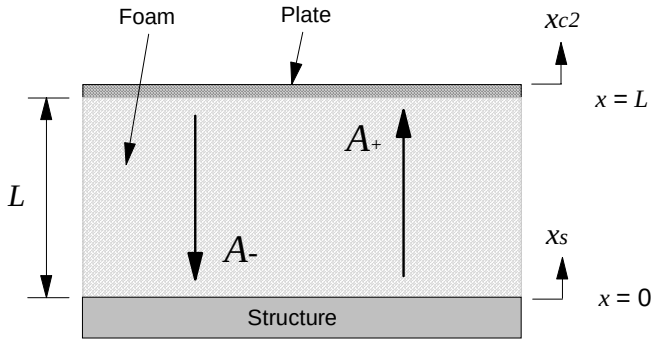

Figure C.1 Continuous model for elastic medium

To account for the damping of the elastic medium, a complex form of the Modulus of Elasticity is used as follows

$$\tilde{E} = E(1 + i\eta) \tag{C.1}$$

where E is the Modulus of Elasticity and η is the loss factor.

The equation of motion for the axial vibration of the elastic medium is given by

$$\frac{\partial^2 u(x,t)}{\partial x^2} = \frac{1}{c^2}\frac{\partial^2 u(x,t)}{\partial t^2} \tag{C.2}$$

where $u(x,t)$ is the axial displacement and c is the speed of sound in the elastic medium, which is defined as

$$c = \sqrt{\frac{\tilde{E}}{\rho}} \tag{C.3}$$

where ρ is the density of the medium.

Equation (C.2) has a solution of the form

$$u(x,t) = A_+ e^{i(\omega t - kx)} + A_- e^{i(\omega t + kx)} \tag{C.4}$$

where A_+ and A_- are the amplitudes of the waves traveling in the positive and negative x direction, respectively, and k is the wave number.

As seen in Figure C.1, there are two system boundaries with a continuity displacement at $x = L$ and a continuity of force at $x = 0$. At x = 0,

$$u(0,t) = x_s \tag{C.5}$$

and at $x = L$,

$$F = m_p \ddot{x}_{c2} = -\tilde{E}S \cdot \left.\frac{\partial u}{\partial x}\right|_{x=L} \tag{C.6}$$

where S is the surface area of the elastic medium. Substituting Eq. (C.4) into Eq. (C.5) and Eq. (C.6) gives

$$A_+ + A_- = x_s \tag{C.7}$$

$$A_+ e^{-ikL}\left(m_p\omega^2 + ikS\tilde{E}\right) + A_- e^{ikL}\left(m_p\omega^2 - ikS\tilde{E}\right) = 0 \tag{C.8}$$

Writing Eqs. (C.7) and (C.8) in matrix form leads to

$$\begin{bmatrix} e^{-ikL}\left(m_p\omega^2 + ikS\tilde{E}\right) & e^{ikL}\left(m_p\omega^2 - ikS\tilde{E}\right) \\ 1 & 1 \end{bmatrix} \begin{Bmatrix} A_+ \\ A_- \end{Bmatrix} = \begin{bmatrix} 0 \\ x_s \end{bmatrix} \tag{C.9}$$

Solution of Eq. (C.8) yields the amplitude of the waves as

$$A_+ = \frac{-e^{ikL}\left(m_p\omega^2 - ikS\tilde{E}\right)}{2i\left[kS\tilde{E}\,\mathbf{cos}(kL) - m_p\varpi^2\,\mathbf{sin}(kL)\right]} \cdot x_s \tag{C.10}$$

$$A_{-} = \frac{e^{-ikL}\left(m_p\omega^2 + ikS\tilde{E}\right)}{2i\left[kS\tilde{E}\,\mathbf{cos}(kL) - m_p\varpi^2\,\mathbf{sin}(kL)\right]} \cdot x_s \tag{C.11}$$

The displacement of the plate is obtained by substituting Eqs. (C.10) and (C.11) into Eq. (C.4) for $x = L$. The plate displacement is then given as

$$x_{c2} = A_{+}e^{-ikL} + A_{-}e^{ikL} = \frac{kS\tilde{E}}{kS\tilde{E}\,\mathbf{cos}(kL) - m_p\omega^2\,\mathbf{sin}(kL)} \tag{C.12}$$

Vita

Bradley W. Ross

Bradley William Ross was born on December 30, 1972 in Aston, Pennsylvania where he spent the first ten years of his life. At the age of ten, his family moved to Oakton, Virginia where he lived until entering the College of Engineering at Virginia Tech in 1991. During his undergraduate studies in the Department of Mechanical Engineering, he developed an interest in the field of acoustics. This interest later developed into a motive to pursue a graduate degree. Upon obtaining a B.S. degree in Mechanical Engineering in 1996, he immediately began graduate studies at Virginia Tech, and was employed as a research assistant in the Vibration and Acoustics Laboratory in the Department of Mechanical Engineering. While employed at Newport News Shipbuilding in the submarine acoustics division, he completed his M.S. degree in 1998.